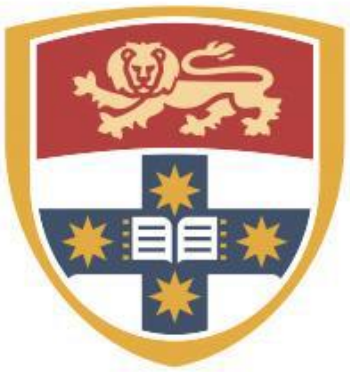

THE UNIVERSITY OF SYDNEY

Cobalt Oxide nanomaterial on MoS_2 quantum dots as a heterojunction photocatalyst for water splitting.

Supervisor: Dr. David Wang

Co-Supervisor: Dr. Jia Ding

A thesis submitted in fulfillment of the requirements for
the degree of Master of Philosophy

by

Upalee Chandramani Labhane

School of Chemical and Biomolecular Engineering
Faculty of Engineering, The University of Sydney.

2024

Declaration

This is to certify that this thesis's content is my own work. This thesis has not been submitted for any purpose.

I certify that the academic content of this thesis is the product of my own work and that all the assistance received in preparing this thesis and sources have been acknowledged.

Acknowledgment

Firstly, my highest gratitude to Dr. Babasaheb Ambedkar for laying down the grounds of the educational scholarship that I hold to join this MPhil. I would like to express my gratitude to my lead supervisor David Wang, who gave me this opportunity to work and provided me not just with academic support but guidance to excel in my personal hardship and fear. Also, I extend my thanks to Dr. Jia Ding for the suggestions in my experimentation setup.

I am grateful to my colleagues, Joyann Li, Haoyue Sun, Rasmeet Singh, Fangxin She, Simran Sethi, Yi-Chen Lin, and Hashim Khan, for being supportive throughout my candidature and not limited to only colleagues' relationships but beyond.

Moral and emotional support from my parents and loved Kobton Mossang was much needed.

Finally, I thank my collaborators, Zelio Fusco, David Alam, Sergio and Asso. Prof. Alejandro Montoya for their technical, lab, and design support.

Authorship attribution and statement

List of Publications.

1. Boosting Hydrogen Generation with Microwaved MoS2-Cobalt Oxide: Effect of sacrificial agents.

2. Microwave-assisted MoS_2 QD and cobalt oxide: heterojunction for hydrogen evolution reaction.

Chapters 3, 4, and parts of Chapter 5 are submitted/in the process of submission as journal articles and will be communicated in the relevant chapters below.

This is a statement to acknowledge that in the above articles, in cases where I am not the corresponding author of a published item, permission to include the published material has been granted by the corresponding author.

Signature:

Abstract

The primary objective of this MPhil research is to investigate the hydrogen evolution reaction (HER) via water splitting using new Molybdenum disulfide (MoS_2) incorporated cobalt oxide photocatalysts. Cobalt oxide has been extensively investigated and proven to be an efficient, and well-established photocatalyst for catalytic applications including organic degradation, CO_2 reduction, and water splitting. This research has explored a rapid and reliable synthesis technique using microwave (MW) irradiation for fabricating cobalt oxide photocatalysts by varying the polyvinyl alcohol as a reaction template precursor. Leveraging the well-known microwave technology for its high kinetic and energy efficiency over conventional hydrothermal and solvothermal technology to synthesize nanomaterials, the advantage of this microwave technique to synthesize cobalt oxide and co-catalyst was explored and established for the first time.

The first study of this thesis investigated the MW synthesis of MoS_2 quantum dots (QD) with photoluminescence and quantum confinement effect to enhance the HER performance of MoS_2 QD modified cobalt oxide-based photocatalyst to achieve a Z-scheme heterojunction construct.

To evaluate the enhanced hydrogen production capabilities of the as-prepared Z-scheme photocatalyst. Initially, the conducted experiment utilizes microwave synthesized MoS_2 QD. The prepared MoS_2 QD were incorporated over the microwave-synthesized cobalt oxide through a simple stirring method. The HER results showed an increment of 16.2 and 22.5 times in absence of sacrificial agent. The unmodified MW cobalt oxide was selected as the control sample for all modifications and the commercial cobalt tetraoxide (Co_3O_4) was used as a comparison.

For the second work, the thesis reports the synthesis of MoS_2 bulk as a co-catalyst with cobalt oxide photocatalyst using the same MW synthesis approach. The effect of HER performance with

and without the use of sacrificial agents: Triethanolamine (TEOA) and a mixture of sodium sulfide (Na_2S), and sodium sulfite (Na_2SO_3) was also investigated in this work.

The results demonstrated competitive hydrogen production with 1l.21 $mmolg^{-1}h^{-1}$ (TEOA) and 16.64 $mmolg^{-1}h^{-1}$ (sodium sulfide (Na_2S) and sodium sulfite (Na_2SO_3)) for MoS_2 bulk heterojunction and 16.4 $mmolg^{-1}h^{-1}$ (TEOA) and 17.5 $mmolg^{-1}h^{-1}$ (sodium sulfide (Na_2S) and sodium sulfite (Na_2SO_3)) for MoS_2 QD.

In both works, the synthesized MoS_2 QD and MoS_2 bulk cobalt oxide photocatalysts were considerably analysed using several characterization techniques including X-Ray diffraction analysis (XRD), X-ray photoelectron spectroscopy (XPS), and Fourier-transform infrared spectroscopy (FTIR) for chemical analysis, transmission electron microscopes (TEM) and scanning electron microscope (SEM) with elemental mapping for morphological analysis, and UV-Vis-NIR and Photoluminescence for optical study. Results from these characterization techniques supported the rationale of enhance photocatalytic performance.

The novelty of this research can be summarized as following. Firstly, the reduction in cobalt oxide synthesis time to 0.15% compared to the average required for hydrothermal process from a 20 hours range to 2 minutes. Secondly, exploring MoS_2 QD synthesis using microwave irradiation is unprecedented to my knowledge. Lastly, the synthesis of Z-scheme heterojunction of the two semiconductor materials (MoS_2 QD and cobalt oxide) for hydrogen evolution reaction is reported for the first time.

Keywords: Photocatalyst, Water splitting, Cobalt oxide, Molybdenum disulfide, Quantum dots, Microwave, Z-scheme heterojunction.

Table of Contents

List of Figures.

List of tables.

List of Abbreviations.

MW	Microwave
QD	Quantum dots
SPR	Surface plasmon resonance effect
LSPR	Localized Surface plasmon resonance effect
SEM	Scanning electron microscopy
TEM	Transmission electron microscopy
XRD	X-ray diffraction
XPS	X-ray photoelectron microscopy
GC	Gas chromatograph
H_2	Hydrogen
O_2	Oxygen
Ar	Argon
UV	Ultraviolet
NIR	Near-infrared
Vis	Visible
PEM	Proton exchange membrane
PL	Photoluminescence
Co_3O_4	Cobalt tetraoxide
MoS_2	Molybdenum disulfide

Chapter 1. Introduction

1.1 Applications and importance of hydrogen

Hydrogen currently has a vast array of applications in chemical industries, ammonia synthesis as a fertilizers [1]. It is also used in petroleum refineries for hydrocracking, hydrotreating to produce petrol and diesel derivatives and used in food industries to transform unsaturated fats into saturated fats to extend the shelf life of the food [1, 2]. Recent a development to be used a as a fuel, not only for passenger cars, and busses but also in space industries where hydrogen along with liquid oxygen is used to achieve high-energy propulsion [3, 4].

Hydrogen is considered a potential alternative source of energy, a fuel for the future [5]. The hydrogen economy is a term used for the overall cycle that involves the synthesis, storage, and application of hydrogen in various sectors of the economy [6]. This can offer an alternative to the fossil fuel-based economy only if newer technological development can provide a viable and green alternative to the current economy [7]. The transition toward the hydrogen economy necessarily has to be developed in an environmentally friendly and using economically competitive technologies [8].

1.2. Current hydrogen production status

The mature and traditional technology that is currently used for hydrogen production is Steam Methane reforming (SMR). Half of the worldwide hydrogen supply comes from SMR [9]. In a typical SMR process, a catalyst usually Nikel is used under high temperature (700 to 1400^{o}C) and pressure to produce hydrogen in the presence of hydrocarbon feedstock, such as natural gas or methane and steam [10]. However, this technology has high environmental impact as amounts of carbon monoxide and carbon dioxide gases are generated along with heavy energy demands [11, 12].

Modern and sustainable technology for hydrogen production is the electrolysis of water. In an electrolysis process, an external energy source is used to drive the uphill chemical process [13]. In an electrolyser device, chemical bonds are dissociated using electricity. Hydrogen reaction happens at the cathode and oxygen evolution at the anode [13]. There are several challenges faced by this process, firstly, the porous diaphragm makes it hazardous, and explosive to operate under pressure between anode and cathode [14]. It also faces high capital cost that includes external circuits and battery assembly which is a prominent challenge along with the cathode material to be noble metal like Pt [15, 16].

These are two key processes currently used for hydrogen production that come with their own sets of challenges and limitations. As a comparative technology for water splitting, photocatalysis is emerging as a promising choice. The overall or half-reaction to produce hydrogen or oxygen over a semiconductor photocatalyst material using solar energy is researched to produce large-scale hydrogen production in a sustainable manner [17]. Recently numerous attempts have been made to develop photocatalysts that can utilise the complete solar spectrum [17]. This can be accomplished by developing a reliable and effective base catalyst or incorporating with a co-catalyst that works synergistically and overcomes the limitation of the base photocatalyst [17]. Being a relatively new technology, achieving commercially suitable conversion efficiency is still a challenge.

1.3. Gaps within the technologies

In the case of SMR, a prominent challenge is the reliance on high temperature that not only leads to energy intensive process but also results in substantial greenhouse gas emissions that is counter to the objective of sustainable future [18]. Furthermore for electrolysers, the challenge lies in the substantial capital cost along with the need to use noble metals in its application [19]. The large

utilization of potassium hydroxide (KOH) as an electrolyte also presents a drawback so an alternative more environmental sustainable electrolyte have be exploited [19]. To address these gaps a development and establishment of materials and technology that can align with sustainable objectives is the need of future.

1.4 Photocatalysis Materials in use

Cobalt oxide has been extensively studied for the photocatalytic operation as it offers advantages like stable chemical states, abundance, cost effectiveness and availability [20]. However, cobalt oxide faces challenges relating to the light absorption, and charge recombination due to its semiconductor characteristic. Overcoming these challenges is the ongoing state of art and future strategies. This can be achieved by synthesising materials with modern technologies that results in unique bond formation, altering shape and size, band gap tuning and the addition of co-catalyst. The addition of co-catalyst can be advantageous for example in enhancing the light absorption, minimising charge recombination, and providing support as physical or chemical to the base catalyst. One such co-catalyst is the Molybdenum disulfide (MoS_2). It is a transition metal dichalcogenide that has gained scientific focus owing to its exceptional properties like chemical, optical, electronical, and excellent surface area [21, 22]. Being able to showcase direct band gap of 1.8 eV for instance, it can be used as a co-catalyst for enhanced light absorption [23]. MoS_2 in this work is used in two physical states in photocatalytic application, first as MoS_2quantum dots and second as MoS_2Bulk and both exhibit significant potential for photocatalytic reaction.

1.5 Sacrificial agents

Sacrificial agents (SA) play a critical role in scaling up water splitting reaction towards commercialisation standards by facilitation of the efficient charge transfer within the photocatalyst [24]. The water only systems face challenges in overcoming the high energy conditions, slow

reaction kinetics, thermodynamic barriers (ΔG = 285.5 kJ mol−1) and the need for higher redox potential. These challenges can be addressed using SA. Primarily, they provide necessary electrons along with the simultaneous quenching of the generated holes and facilitate the thermodynamic requirement [25]. In this study two SA systems have been studied, Triethanolamine (TEOA) and a mixture of sodium sulfide (Na_2S), and sodium sulfite (Na_2SO_3).

1.6 Thesis structure

The Figure 1 shows the thesis flow starting with introduction of the thesis. Followed by identifying the gaps and then deriving the strategies to overcome the gaps regarding the choice of photocatalyst and synthesis methods. Then experimental sections incapsulated by two research articles followed by comparing both the experimental sections and finally proposing the results.

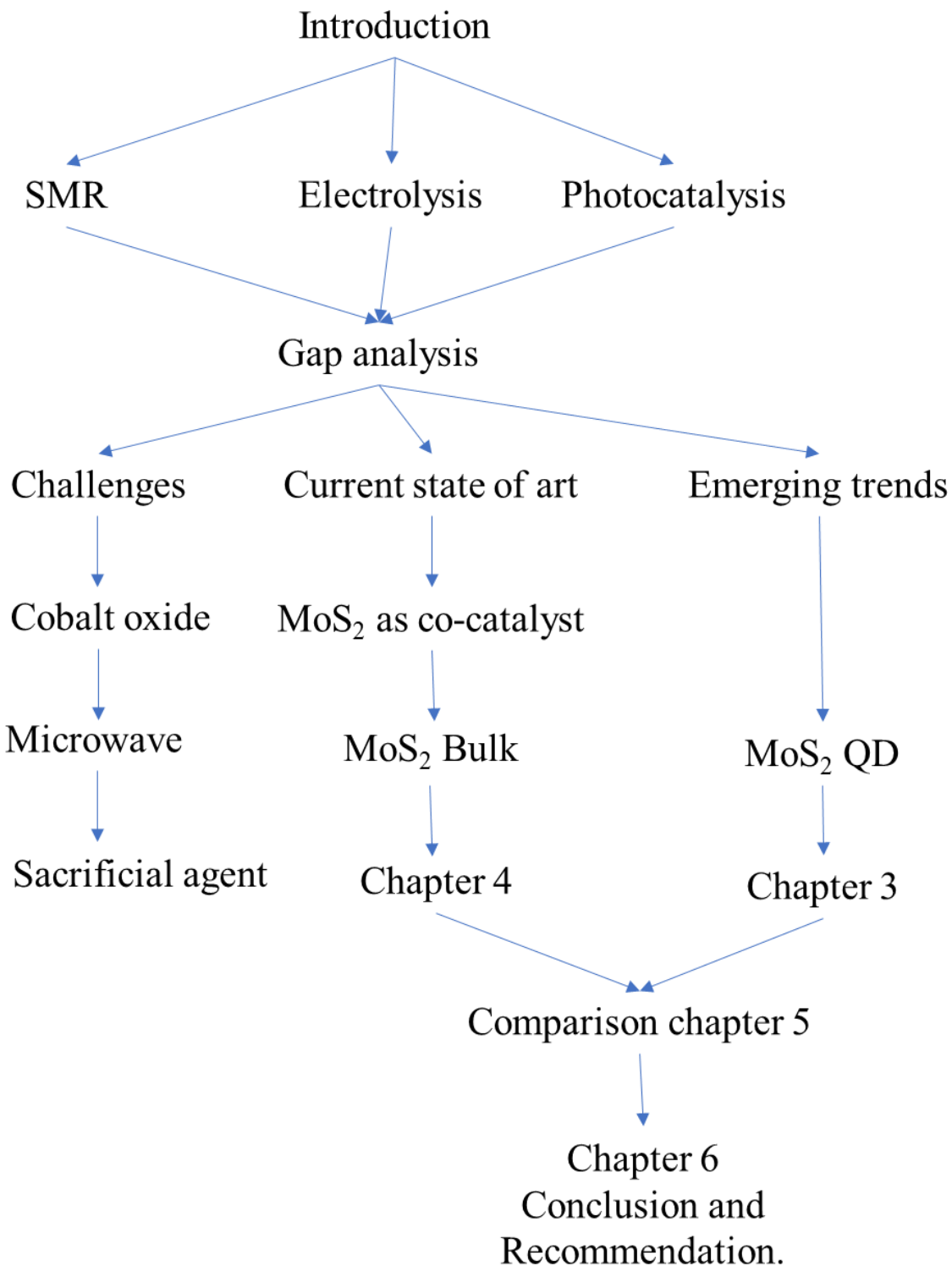

Figure 1: Thesis Mindmap.

1.5 Objective:

1. To investigate the feasibility of microwave for rapid synthesis of cobalt oxide as a photocatalyst.

2. To investigate the successful synthesis of MoS_2 Quantum dots using microwave.

3. A Z-Scheme heterojunction is established with cobalt oxide MoS_2 bulk and MoS_2 QD to investigate the hydrogen evolution reaction.

4. To evaluate the influence of sacrificial agent on the heterojunction formed above.

Chapter 2. Literature review

2.1 Water splitting

The quest for alternative source of energy has led the scientific focus towards hydrogen evolution via water splitting [26]. The traditional methods for hydrogen generation relies on fossil fuels, that contributes highly towards environmental pollution, carbon emission, thus causing challenges that necessitate a transition towards the sustainable renewable energy solutions [27]. This transition is driven by the increasing scarcity, cost fluctuation owing to the source availability, geopolitical reasons, and importantly detrimental environmental impact [28]. So, the quest of green hydrogen has gained high pace due to alarming environmental concerns and the limited conventional fossil fuel. Green Hydrogen has significant potential to emerge as a promising energy solution to the growing environmentally friendly energy needs [29]. It also stands out by proving to offer advantages including clean combustion profile and usable flexibility for several modern applications making it as a rational choice [30]. Thus, to generate green hydrogen, one of the promising technologies is the dissociation of water that offers a potential solution to address the challenges related with sustainable hydrogen supply.

Water splitting is a process that involves dissociation of a water molecule into its component elements, hydrogen and oxygen and that can be driven by external forces like electricity, thermal, and light [29, 31]. In the subsequent session the detailed analysis of each step will be provided. Water splitting has grasped attention as its energy effective and environmentally benign approach of hydrogen production [32]. In this process the primary input is light and water that presents advantage over fossil fuel based hydrogen generation techniques that involves hydrocarbon as raw materials [33]. From a thermodynamic perspective water splitting is a uphill reaction, it implies that, additional energy input is required to overcome the thermodynamic barrier

which contributes to 1.23 eV [34]. This thermodynamic barrier associated to the hydrogen and oxygen bond breakage in a water molecule rendering that the process is thermodynamically non spontaneous [34].

Equation for water splitting: $H_2O \longrightarrow H_2+1/2O_2$

2.1.1 Steam methane reforming (SMR)

Steam reforming of methane stands as a primary and prominent source of hydrogen production that currently surpasses other new technologies [35]. This is a recognised and mature technology for effectively converting methane-rich feedstock such as a natural gas into hydrogen [35]. The SMR usually involves the use of hydrocarbon feedstock typically natural gas or methane in combination with steam that is passed over a Nikel based catalyst to yield hydrogen gas [35]. This reaction occurs over high temperature generally around 700 – 1400^{o}C and under high pressures. A undesired outcome of this technology is the significant amount of carbon monoxide and carbon dioxide [36]. When carbon monoxide is generated, it is passed through a water gas shift process to convert into carbon dioxide and the hydrogen purification is achieved by employing an amine unit [36]. On case per case basis, mostly SMRs are fitted with carbon capture and sequestration (CCS) units to capture generated carbon denoted in the Figure 2 while in other instances the carbonous gasses are released into the environment that contributes to adverse repercussions [36]. However, the incorporation of and additional CCS step contributes to the overall capital cost. Not only that but this process is burdened with drawbacks like the release of greenhouse gasses which is a significant challenge that hampered the pursuit of sustainable future. Additional to these challenges, the reliance on non-renewable resources (fossil fuels) for hydrogen production is also a major drawback [37].

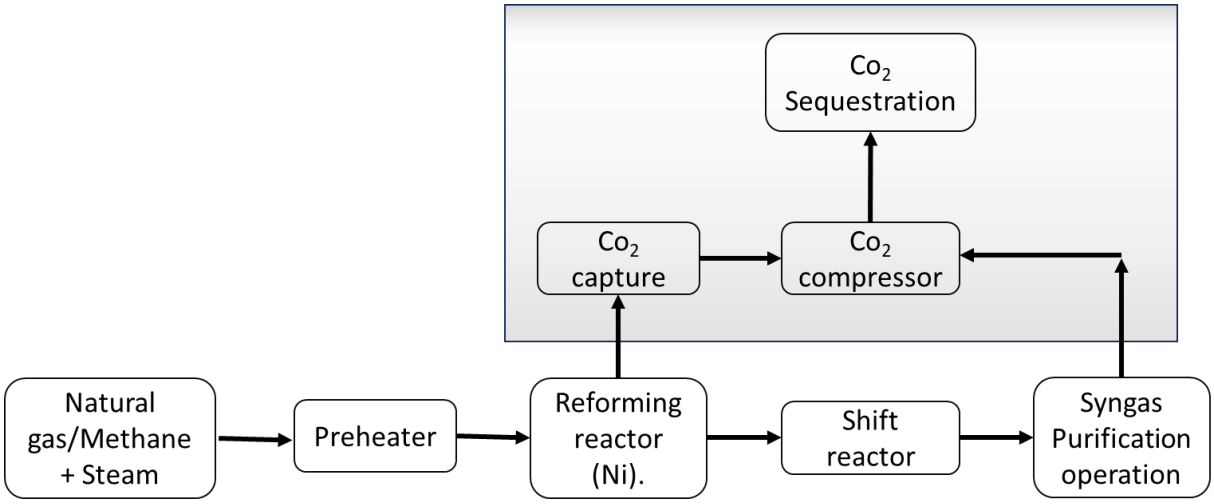

Figure 2: Schematic of SMR of a typical SMR process with highlighted CCS unit to capture carbon monoxides and carbon dioxides.

2.1.2 Water splitting – electrolysis

Electrolysis serves as an effective method for splitting water into its fundamental components – hydrogen and oxygen by applying external electrical current [38]. In a typical electrolysis cell, the two critical components are anode as an oxygen electrode and a counter electrode as cathode functioning as a negative electrode and both have a thickness of 200µm – 300µm [39, 40]. At the positively charged electrode (anode) water molecule release electron while at the negatively charged electrode (cathode) the molecules accept the electrons. These two electrodes are separated by an ionic conducting electrolyte which is potassium hydroxide (KOH) [39, 40].

The reaction can be represented as

$2H_2O \rightarrow 4e^- + 4H^+ + O_2$ (Anode) Eq (1)

$4e^- + 4H^+ \rightarrow 2H_2$ (Cathode) Eq (2)

Overall reaction

$2H_2O \rightarrow 2H_2 + O_2$ Eq(3)

Alkaline water electrolysis (AWE) is a well-established technology that employs low-cost metals catalyst. However, it does pertain associated disadvantages relating to the low current density, low operational pressures, and gas crossover issue [41]. Another studied technology is a solid polymer electrolyte water electrolysis. Though overcoming the limitations of the AWE, it introduces drawbacks such as high cost of components including proton membrane exchange (PEM), and the necessity for noble metal catalyst and lower range output power [41]. Figure 3 shows the simple representation of a PEM electrolyser with Pt and Ir noble metal catalyst. The oxygen evolution reaction represents the determining step in water electrolysis process that demands a high over potential due to its irreversibility that hinders the over forward reaction [42]. Achieving the overpotential requires a substantial electrical current contributing to the energy consumption resulting in higher cost and energy [42]. To mitigate the high energy needs newer modifications as integration of renewable energy sources like solar panels, or wind power is ideal. But this addition comes with capital cost and heavy maintenance. However, this is a considerably sustainable process compared to SMR but the need to address the challenges is crucial for the advancement and success of the electrolytic water splitting process.

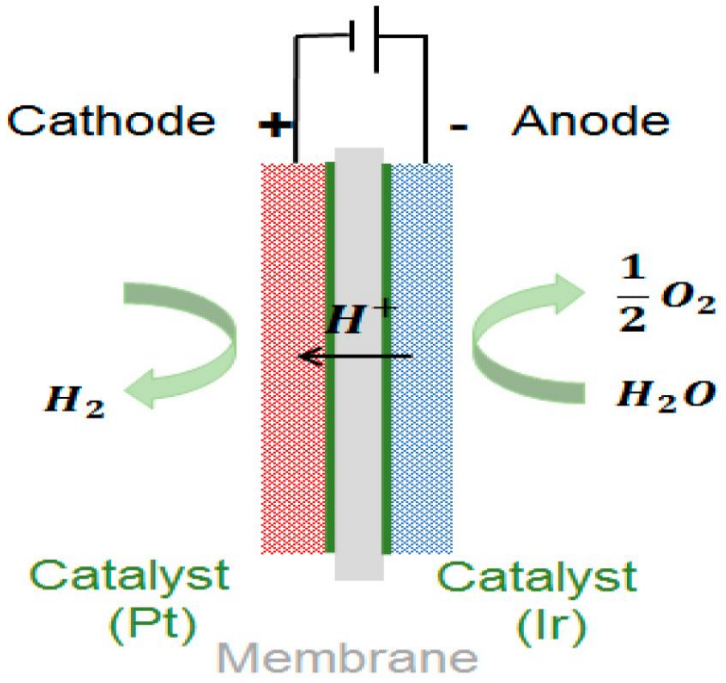

Figure 3: PEM electrolysis with platinum and Iridium catalyst separated by a membrane [48].

2.1.3 Water splitting – photocatalysis

The utilization of the solar energy for green hydrogen production via using a semiconductor material (photocatalyst) is a highly effective and environmentally friendly modern technique. It benefits from the abundance and renewability of both water and solar while operating in ambient temperature and pressure [43]. The semiconductor material has an electronic band arrangement that consists of a packed valence band and an empty conduction band separated by a band gap [44, 45]. When the light source of energy greater than the band gap is incident on the photocatalyst the electrons in the valence band are excited to the conduction band [45]. From a thermodynamic perspective, photocatalytic reaction can be categorised into two types depending on the Gibbs free energy change; 1. Uphill reaction where the Gibbs free energy is positive ($\Delta G = 285.5$ KJ mol−1) and 2. Downhill reaction with a negative Gibbs free energy (Δ-G^o). In case of the photocatalytic

water splitting reaction, the process is a uphill as the dissociation of the water molecules is accompanied by a positive change in the Gibbs free energy, shown in Figure 4 [46]. To achieve this, photon energy is therefore converted into chemical energy during the water splitting reaction [47, 48].

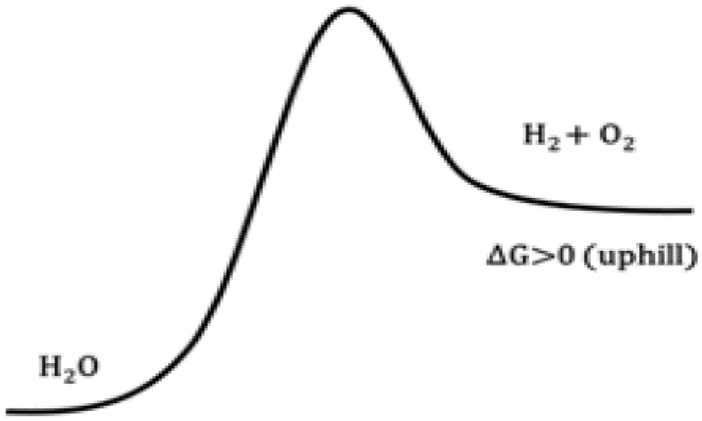

Figure 4: A thermodynamic plot of photocatalysis as an uphill reaction with (ΔGo) > zero [51].

The photocatalytic hydrogen evolution reaction (HER) process comprises of several steps. First, the generation of the exciton consisting of electrons and holes upon the light absorption. Second, exciton charge migration to the photocatalyst's surface. Thirdly, the migrated excitons to react with water molecule to produce hydrogen at the conduction band while the oxygen at the valance band [49]. The overall photocatalytic process involves the participation of four electrons that are shown in the equation below [50].

$$\text{Photocatalyst} + 4h\gamma \text{ photons (irradiated light)} \rightarrow \text{Photocatalyst} + 4h^{+} + 4e \qquad \text{Eq (1)}$$

$$4e^{-} + 4H^{+} \rightarrow 2H^{\bullet} + 2H^{\bullet} \rightarrow 2H_2 \qquad \text{Eq (2)}$$

$$4h^{+} + 4H_2O \rightarrow 4OH^{\bullet} + 4H^{+} \qquad \text{Eq (3)}$$

$2OH^{\bullet} + 2OH^{\bullet} \rightarrow 2H_2O + O_2$ Eq (4)

A typical photocatalytic schematic is shown in Figure 5 where the photocatalyst is dispersed in water and with light irradiation, and hydrogen and oxygen gasses are evolved.

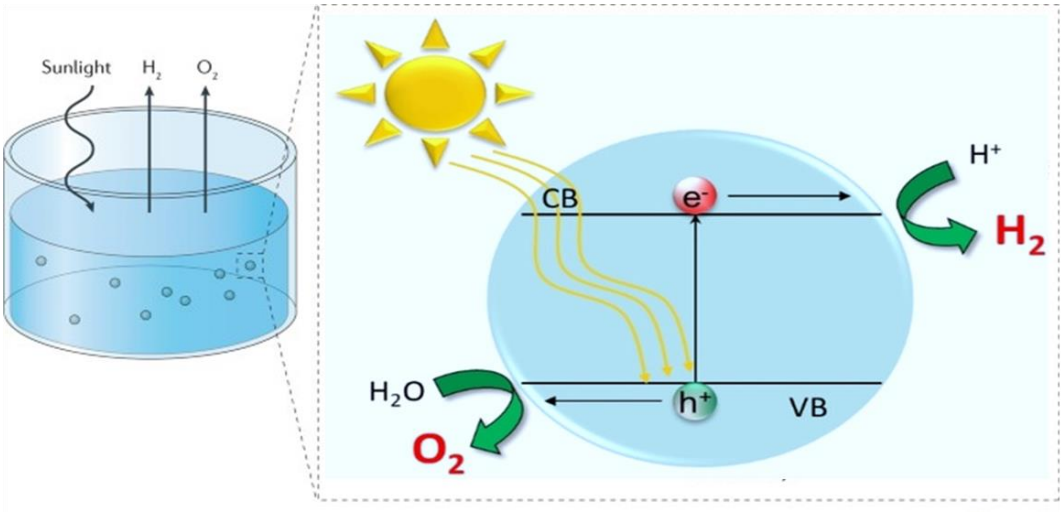

Figure 5 Shows the photocatalytic system with charge excitation in the semiconductor photocatalyst [51, 52].

2.2 Challenges, current state of art, and Emerging trends – photocatalyst for water splitting

2.2.1 Challenges in photocatalyst

Semiconductor photocatalyst material play a pivotal role in the process of water splitting because of their capacity of harnessing solar energy to initiate the redox reaction that decomposes water. Metal oxides are among the commonly used materials for this purpose. Owing to their semiconductor's nature, the limitations for overall water splitting are, 1. The development of suitable photocatalyst that has appropriate band gap which promotes the reaction with minimal

amount of energy to achieve the uphill reaction. 2. The adjustable band structure of valance and conduction band. 3. Higher stability so the photocatalyst can be used of longer reaction time with minimal loss of efficiency. 4. The ability to harness the complete solar light spectra. 5. Inefficient charge migration are some major challenges associated with the semiconductor photocatalyst [17].

2.2.2 Current state of art in photocatalyst

Recent efforts have been focused on the enhancing the optical properties, charge separation capabilities and stability of the photocatalyst. One such prominent strategy is the loading of co-catalyst onto the semiconductor surface. Table 1 discusses the different co-catalyst incorporated with cobalt based photocatalyst. For example, the use of Pd, Au, Ag, Ni, MoS_2, Cd and sulfide, metal oxides, biomimic hydrogenase as a cocatalyst have resulted in promising improvements in the area of light harvesting as a co-catalyst [53, 54]. These co-catalyst strategies contribute to lowering the activation energy and catalysing the surface reactions and supressing the exciton recombination [54].

Furthermore, the reaction conditions are also studied like temperature and pH dependence has been investigated where the hydrogen evolution shows variation with varying pH conditions. Silva et al., [55] observed a HER of 1 mmol $g^{-1}h^{-1}$ at pH 14 which dropped to 0.15 mmol $g^{-1}h^{-1}$ at neutral pH. 'Development in the materials field is the use of bismuth-based halide perovskites' Liang et at., (2022) studied the use of hierarchal mesoporous $SrWO_4$ doped with the metallic Bismuth that resulted in an significant 2.4 fold increase in the photocatalytic activity [56]. A variety of Bi based materials ($NiCoP/Cs_2AgBiBr_6$) [57] have been studies for their improved interfacial charge transfer kinetics and surface reaction dynamics [58, 59]. While these recent materials show promising performance their challenges still remain like the materials exhibit instability in aqueous media that limits their application in various solvent environment dynamics [58, 59]. Metal organic

framework (MOFs) have gained attention due to their surface area, porosity, turnability but they face limitations in terms of stability under harsh conditions, for example while using with a oxidising sacrificial agents [60].

2.2.3 Emerging trends in Photocatalyst

A noteworthy and highly potential emerging trend in the realm of semiconductor is the application of quantum dots (QD). They have gained significant attention and extensive scientific investigation due to their excellent light absorbance capacity multi excitation effect adjustable energy bands, optoelectronic properties and so forth [61]. QD are classified as quasi-zero-dimensional materials consisting of a small number of atoms with the size typically less than 10nm that is closer to the exciton Bohr radius [62]. This supports QDs to display unique characteristics of singular photophysical and photochemical properties [63]. QDs have a tuneable band gap and that is proportional to their size showcasing unique properties like quantum confinement effect, surface plasmon resonance, visible light absorption capacities and high volume to surface area ratio that provides high concentration of active sites. [64, 65]. Quantum confinement property enables the QDs to extend their light absorbing capabilities to near infrared region (NIR) along with visible light and that is altered by their band gap and size [63]. The size also plays pivotal role in effectively migrating the charges from the core material to its surface. Furthermore, multi exciton generation within the QDs allows them to achieve high efficiency in HER. Another optical property, the up-conversion fluorescence effect gives QDs the ability to harvest light of NIR and convert it to a shorted wavelengths which is in visible light region. This results in enhancing the light exposure to the base photocatalyst [63]. For instance, the integration of MoS_2QD onto the Bi_2S_3 nanorods served as a light harvesting co-catalyst that resulted in up-conversion fluorescence

that aided Bi_2S_3 to retain its HER in the NIR. however standalone Bi_2S_3 does not exhibit the HER property [63].

As a co-catalyst in a photocatalytic reaction, quantum dots assumed a multifunctional role. Firstly, QDs serve as a proficient host or photosensitiser that generates charge carriers to initiate the water splitting process. Secondly, they can act as a charge carrier that mediates half oxidation or reduction reaction. This role is critical in limiting the charge recombination phenomenon. Thirdly, QDs can work as a light trapping, augmenting the light harvesting capacity of the base catalyst [66-68]. QDs in ideal circumstances should exhibit more negative potential conduction band, while the valence band should be more positive compared to the base semiconductor material [69]. QDs possess a direct bandgap in a range of 1.8 to 2.8 eV rendering them capable of effectively absorbing the various light spectra [70]. When exposed to external light source, in return QDs emits varying light frequency different than the light source which is called the fluorescence effect. This variation in the light emittance is proportional to the QDs size, composition and structure [63]. For example, CdTe QDs having a size between 2.5 to 4 nm, showed an emittance from 510 to 600 nm, this property can be utilised to assist the base photocatalyst to absorb a specific wavelength of light that can enhance the HER [63]. Several characterisation techniques can be used to confirm the formation of desired QDs, some of the techniques are diffuse reflectance spectroscopy (UV-Vis DRS) and photoluminescence [63]. To leverage these properties, numerous strategies have been explored to integrate QDs onto a base semiconductor that opens up new avenues of improving photocatalytic performance.

Metal based QDs can be classified into two categories 1. Noble metal QD and 2. Non noble metal QDs. The noble metal QD like Au, Ag, Pd, Pt, Rh and Ir are known for their unique phenomenon surface plasmon resonance (SPR) and hot carrier participation [71, 72]. Reddy et al

[73], investigated a TiO_2 based photocatalyst and modified with Cu/Ag QDs under UV light the performance was enhanced from 0.1mmol $h^{-1}g^{-1}$ (TiO_2) to 16.3 mmol $h^{-1}g^{-1}$ (Cu/Ag QDs/TiO_2) for UV-Visible light. This confirms the co-catalyst modification of SPR induced QDs can successfully improve the hydrogen yield. The limiting factor for using noble metal quantum dots is their higher cost and limited supply and however, considering the scarcity and high demand, the cost of production for the noble metal quantum dots will be rising.

An alternative, the higher availability and lower cost for the non-noble QD makes them a logical consideration for the use in hydrogen evolution reaction. Non noble metal QD also shows quantum confinement, photoluminescence, up-conversion fluorescence effects. Along with that, they also show improved charge separation and migration thus reducing the recombination of the electron and holes [74]. The non noble metal QDs that are currently investigated are Bi [75], Ni [76], Cu [77], Al [78], Zn [79], Na [80], Mg [81], Mo [82]. Weizhao et al., [83] showed a systematic comparison of TiO_2 modified with non-noble NiQD and with noble metal Pt where optimal dosing of Ni QD/TiO_2 yielded a hydrogen rate of 1.35 mmol h^{-1} g^{-1} which is equivalent to the Pt/TiO_2 modified photocatalyst with 1.39 mmol h^{-1} g^{-1}. This observation concludes that non-noble QDs can be a reasonable replacement to the noble metal without compromising on the HER performance.

2.3 Cobalt oxide-based photocatalyst

Cobalt oxide has been a subject of comprehensive investigation for various catalytic applications, like CO_2 reduction, N_2 fixation and degradation of organic pollutants, and water splitting [84]. These are multiple cobalt based materials used for water splitting purposes like cobalt oxides (Co_3O_4, CoO, CoO_2, Co_2O_3), cobalt hydroxide [$Co(OH)_2$] and cobalt oxyhydroxide [CoO(OH)] [85]. The material parameters to be considered while synthesising the cobalt based photocatalyst

are crystallinity, amorphous, morphology, size, exposed faced and lastly **surface vs. bulk oxidation states, band gap and charge recombination** [85]. It offers several advantages such as high surface to volume ratio, stable chemical states, and cost effectiveness. In photocatalytic applications, the presence of Co^{2+} and Co^{3+} redox couple is advantageous in order to transfer electrons for water splitting, where $Co2^{+}$ and $Co3^{+}$ occupies tetrahedral and octahedral voids respectively [20]. Also, Co^{2+} species are responsible to for the formation of key intermediates such as CoOOH during water spitting mechanism [85]. The Co^{3+} species present at octahedral coordinate are not directly participating in the reaction but are responsible for the charge transfer due to their highly reactive nature [85]. Thus, understanding their roles and quantity present is critical to design an effective cobalt based photocatalyst. Despite several advantages, cobalt oxide owing to its semiconductor nature has some limitations and area for improvements owing to its semiconduction nature. Some limitations are the relatively low catalytic activity, lower active sites density**, limited light absorption, electron recombination (surface and bulk recombination pathways)** (bold are the limitations endeavoured to address in this research work) shown in Figure 6.

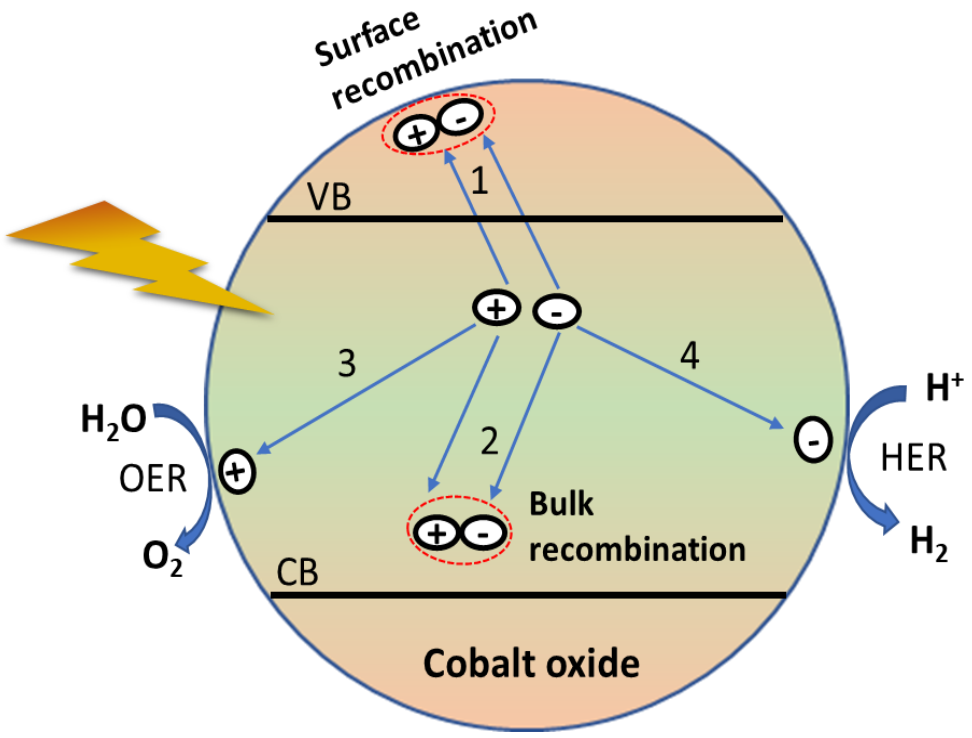

Figure 6: Single semiconductor photocatalyst (cobalt oxide) and pathways of charge recombination

The current challenges in improving the catalytic efficiency of cobalt oxide revolves around the synthesis of distinctive nanostructures, morphological design, tuning size, and shape that can impact the band gap. Importantly, incorporating co-catalyst to enhance the charge migration, separation and improvement in the light absorption [84]. From material synthesis point of view, cobalt oxide nanomaterial is a synthesised using longer time thus energy intensive processes like solvothermal and hydrothermal discussed in the Table 1 [86, 87]. Thus, modern rapid synthesis methods are investigated for the synthesis of cobalt oxide one such prominent method is the microwave irradiation which is discussed in detail in the below relevant sections.

Table 1 also compares various sacrificial agents including Methanol, Latic acid, Triethanolamine, and Sulfide and Sulfite based, Also NA NA SA is abbreviated for not available and no sacrificial agent . Also, various co-catalyst (noble and non-noble) are discussed forming a range of Z-scheme heterojunctions.

Investigation of co-catalyst mixed metal oxide as a photocatalyst is conducted by Menezes et al., 2015, where cobalt and manganese were studied for oxidation and reduction reaction [88]. Recently, Tien et al., 2023 investigated another photocatalyst with cobalt oxide as base and MoS_2 as co-catalyst observed increased HER from 66.8 µmol $h^{-1}g^{-1}$ for Co_3O_4 to 765 µmol $h^{-1}g^{-1}$ after modification by Z-scheme with MoS_2. This performance enhancement is due to better charge separation and light absorbance [89].

Table 1. Comparison of cobalt-based catalysts' hydrogen production rate with co-catalyst and modifier under different sacrificial agent systems.

Photocatalyst	**Sacrificial agent**	**Hydrogen production rate (mmol h^{-1} g^{-1})**	**Synthesis Method**	**Synthesis Time (hrs)**	**Ref.**
Co/TiO_2	Methanol	0.8	Hydrothermal and Ion exchange	5	[90]
$Co(OH)_2/TiO_2$	Methanol	0.7	In-situ synthetic method	-	[91]
$NiCo_2O_4/g\text{-}C_3N_4$	Methanol	0.5	Thermal polymerization.	2	[92]
Au-Co / TiO_2	Methanol	171	IWI and DPU	-	[93]
$Pt/AgTa_{0.7}Nb_{0.3}O_3$/ Co–Pi	Methanol	0.012	hydrothermal method	48	[94]
Plasmonic AuNP@CoTPy	Methanol	3.21	Heating and stirring.	6.5	[95]
NiCo-LDH/40 wt% P-CdS	Lactic acid	8.7	Solvothermal and hydrothermal.	25	[96]

CoP quantum dots (QDs)/ CdS/rGO	Lactic acid	1.1	Two-step heating reaction.	10	[97]
MoS_2/Co_3O_4 nano-heterojunction	Lactic acid	3.8	Hydrothermal	20	[89]
Co-2TPABTz Co-2TPABTz / Ag NP	Lactic acid	20.65	Stirring and evaporation,	36	[98]
Co_3O_4	TEOA	0.66	Hydrothermal method.	29	[99]
g-C_3N_4/CoP QD-4%	TEOA	0.93	Heating	5	[100]
0.45 wt% CoP modified g-C_3N_4	TEOA	1.0	Thermal condensation	12	[101]
$CuCo_2O_4$/g-C_3N_4	TEOA	4.1	Reflux-calcination.	1.5	[102]
$Cu_{0.9}Co_{2.1}S_4@MoS_2$	TEOA	4.0	Hydrothermal method.	24	[103]
CoS2/g-C3N4	TEOA	1.2	hydrothermal method.	12	[104]
plasmonic $Ag@CoFe_2O_4$/g-C_3N_4.	TEOA	0.33	Hydrothermal	18	[105]
2% Co_2P/RP	Na_2S/Na_2SO_3	5.9	Hydrothermal method	12	[106]
CdS/CoO_x core-shell NRs	Na_2S/Na_2SO_3	3.5	Impregnation and calcination	50	[107]
CdS/CoO		6.45	Hydrothermal method	24	[108]
CZS/M-CoO-1.5%	Na_2S/Na_2SO_3	1.78	Hydrothermal method.	24	[109]
$Mn_{0.2}Cd_{0.8}S/MoS_2$/ Co_3O	Na_2S/Na_2SO_3	16.4	Solvothermal.	30	[110]
3% $NiCo_2O_4$ /$Mn_{0.05}Cd_{0.95}S$	Na_2S/Na_2SO_3	17	Hydrothermal.	8	[111]
CoO/NiCo-LDH	Na_2S/Na_2SO_3	1.5	Hydrothermal method	24	[112]
CdS (QD)/Co_9S_8	Na_2S/Na_2SO_3	1.06	Hydrothermal.	-	[113]

MoS_2/Co_3O_4	Na_2S/Na_2SO_3	3.8	hydrothermal method.	20	[114]
Pt_3Co/CdS	$(NH_4)_2SO_3$	45.09	Solvothermal & hydrothermal	18	[115]
$Co(dcbpy)_2(NCS)_2$/ CQDs/CN	Not specify	0.3	Hydrothermal and heating	36	[116]
Co_2P/CdS	NA	262.1	Ultrasonication and stirring.	24	[117]
NiCoP/g-C_3N_4-3	NA	0.07	Thermal pyritization	4	[118]
$Co_{0.85}Se$ (1.5 wt %)/$Cd_{0.5}Zn_{0.5}S$	NA	0.7	Solvothermal	-	[119]
AuNP@CoTPyP	No SA	3.21	Colloid mixing	-	[95]
(CoOx)- (AgTaO3)	No SA	0.075	Hydrothermal and Photo deposition	-	[120]
Co3O4/CdS/SrTiO3	No SA	0.9	Hydrothermal-chemical-photo deposition method.	-	[121]
Pd/Ir/ CoO_x	No SA	0.008	Cross-coupling reaction	-	[122]
Plasmonic ZrN-CoO_x	No SA	32.44	Calcination	-	[123]
Plasmonic CuCo	NA SA	0.07	Hydrothermal	2	[124]
Plasmonic CuCo	No SA	0.078	Hydrothermal	4	[125]

2.4 MoS_2Bulk and MoS_2QD

MoS_2 is a transition metal dichalcogenide (TMD), that has been investigated as a promising material in recent years due to its inherent chemical, electronic, optical properties, high mobility and effective surface area [21, 22]. MoS_2 TMD is formed as a sandwich like structure with a layer of Molybdenum (+4) lies between 2 layers of sulfur (-2) as S-Mo-S and these layers are bonded together by Van der Waal forces [126]. Two main phases of MoS_2 are observed, first is the 1T phase characterised by an octahedral coordination structure of molybdenum (Mo) and sulfur (S) atoms and while the second is 2H that has a trigonal prismatic structure as shown in the Figure 7

[127, 128]. In its monolayer form, MoS_2 demonstrate a direct band gap of 1.8 eV, although this can be tuned by varying the interlayer spacing [23]. The metastable 1T phase is particularly noteworthy for its catalytic properties for HER because of its reactive basal planes and strong binding affinity of S atom and surface covalent functionalization [129]. Particularly, the binding potential towards hydrogen atom of the MoS_2 1T nano sheet along with the improved charge transfer kinetics and surface activity overall contributes towards the HER reaction [129]. This is in contrast to 2H MoS_2 sheets, where the catalytic activity is associated to the edges, not the basal plane, thus 1T phase has a sight advantage for the HER reaction [130].

A promising future trend discussed in the previous sections is the used of MoS_2QD for HER application which processes a unique strong quantum confinement limited to QDs, and MoS_2 properties are carried along like edge effect and a direct bandgap. MoS_2QD showcases all the advantageous properties of QDs discussed above like surface area to volume ratio, excellent electrical conductivity adds large active edge sites, owing to these properties MoS_2 QD promising material to enhance HER [130, 131]. Its quantum confinement effect enhances the photon response that results in improving the photoluminescence (PL) properties of the base photocatalyst [132].

In MoS_2 QD, quantum confinement arise due to the conjugated π-domains that alongside acts as a centre of the PL and also small dielectric constant and week spin orbit coupling [133]. This size alteration of MoS_2QD results in the increment of photoluminescence properties [134]. Wen Qiao et al., 2015 demonstrated that, the MoS_2 QD when compared to MoS_2 nano sheets exhibited higher HER activity [135]. Thus, MoS_2 is a promising material for HER reactions as both bulk and monolayer QD configuration.

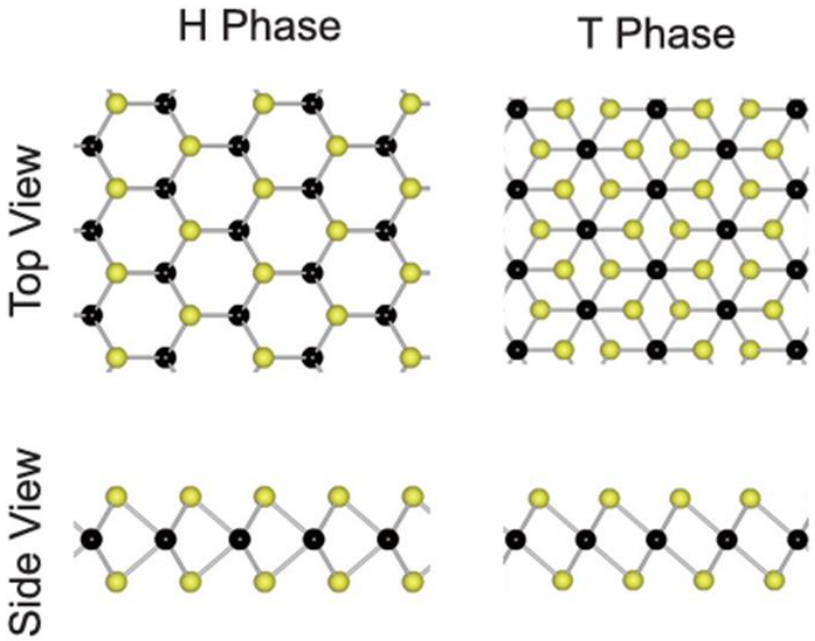

Figure 7: The crystal structure of MoS_2. Two phase of MoS2 (H phase and T phase) side and top view [128].

2.5 Z-scheme heterojunction for Cobalt oxide and Molybdenum disulfide

The enhancement in the performance of photocatalysts is governed by the synthesis of an efficient heterojunction, which are the interfaces developed between multiple photocatalyst materials resulting in different band structures [136]. As a result of this interface, the heterojunction promotes electron and hole and inter-catalyst migration, and charge separation thus enhancing the photocatalytic performance [137]. Heterojunction were proposed to mitigate the limitations of single semiconductor photocatalyst used for water splitting that simultaneously produced hydrogen and oxygen by having two active sites within the one semiconductor material. However their performance was greatly limited due to electron and hole recombination within the single semiconductor material that can either be by pathway 1 (surface recombination) or pathway 2 (bulk recombination) showed previously in the Figure 6 [137]. The proposed Z-scheme heterojunction

consist of two semiconductor materials (I and II) consisting of different band gaps where the first act as an electron donor and the second as an electron acceptor semiconductor shown in Figure 8 [138]. The mechanism of Z-scheme heterojunction comprises of active boundary sites that involve electron transfer between the semiconductors with and without the presence of electron mediator [139]. Particularly, after the generation of electrons and holes in each semiconductor, the electrons migrate from conduction band of the first photocatalyst (cobalt oxide, I) to the valence band of the second photocatalyst (MoS_2, II) forming a stable electron-hole recombination. This leaves pairs of electrons in conduction band of the semiconductor II, and these are the reducing sites for hydrogen evolution. Also for semiconductor I at the valence band, the holes act as oxidation sites for oxygen evolution [140]. Due to this mechanism, Z-scheme heterojunction shows prominent advantages like the enhancement of redox potential, increased light harvesting because of their so formed newer band structure [141], and finally, the charge transfer is more favourable owing to its electrostatic attraction between electrons and holes at the migration sites [137].

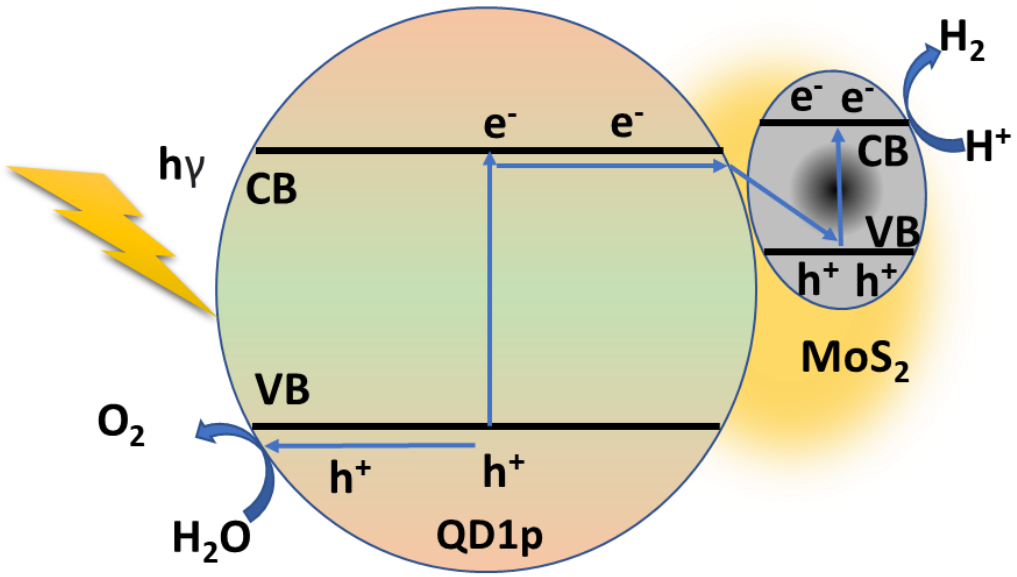

Figure 8: Z-scheme heterojunction of cobalt oxide and MoS_2 and charge transfer between two semiconductor photocatalyst

2.6 Microwave irradiation for synthesis

Metal oxides and metal chalcogenide semiconductor materials are synthesised conventionally by solvothermal and hydrothermal method. These methods involve high temperature and pressure conditions (temperature range from 600^{o}C to 1200^{o}C and pressure conditions are around 50 bars)for extended periods (12-24 hours) as a result, large amount of energy is consumed in the synthesis process and adding up to the operational cost. This limitation can be overcome by employing modern microwave synthesise technology. In principle, microwave are electromagnetic fields it has a frequency between 300 MHz and 300 GHz and the wavelength of 1 mm to 1m, respectively [142]. A schematic of microwave reactor and the sample generating heat from the core is shown in Figure 9. These electromagnetic fields can be divided into two sections 1. electric and 2. magnetic. Electric component of the electromagnetic waves is responsible for heating of the material. The heating operates by two mechanisms 1. dipole polarization and 2. ion conduction [143]. Unlike the conventional heating, which relies on conduction for heat transfer, microwave involves a direct energy conversion to thermal energy from electromagnetic waves. The microwave energy is supplied to the material and heat can be created uniformly throughout the volume of the reaction mixture resulting as volumetric heating [143, 144]. Only the reaction mixture is heated while the microwave reactor chamber remains at ambient temperature. Not only volumetric heating but, microwave offers advantages such as selective heating, quick initiation and termination of the synthesis process, non-contact heating of the material, reduced synthesis times thus reducing the operation cost [143, 145]. Additionally, microwave irradiation technique can provide precise control over heating rate.

For example, Wilson et al., [146] compare the formulation of TiO_2 using a traditional hydrothermal and microwave method and finding that microwave showed higher crystallinity with reduced energy and time. Similarly, Yap et al., [147] observed change in the morphology of CuO crystals by using microwave over hydrothermal. Recently Huang et al., [148] synthesised cobalt based MOF catalyst by using microwave for just 60 seconds of irradiation, MOF showed strong electrocatalytic performance for HER and OERs. The advantage of using microwave strategy as it consumed only 0.37% of energy as compared to conventional pyrolysis method [148].

The above studies demonstrate that the use of microwave provides flexibility and controlled over synthesis parameters that influence the properties of nanomaterials. This is especially advantageous in photocatalysis because the nano material properties significantly impact the catalytic performance of the material. Therefore, the hypothesis for choosing microwave irradiation for synthesis of the cobalt oxide and molybdenum disulfide is that microwave will initiate different reaction kinetics and pathways that can lead to unique physical properties like shape, size, morphology, and chemical structure like bonding and electronic states that can strongly result to a better photocatalytic performance for HER.

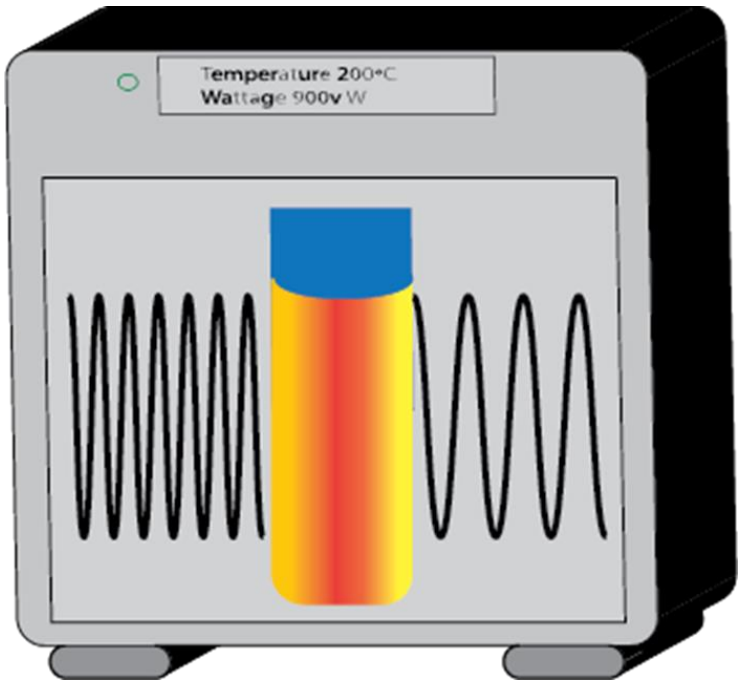

Figure 9: Microwave reactor with heated sample vial (red colour is the most heated part) after absorbing microwaves.

2.7 Sacrificial agents – Significance and advantage

Sacrificial agent (SA) play a crucial role in overall water splitting process as they serve as an electron acceptor and/or donor that allows efficient quenching and charge transfer within the semiconductor photocatalyst [24]. Photocatalytic water splitting faces thermodynamic barriers like the high energy conditions to drive the reaction that has sufficiently larger thermodynamic potential [149]. This can be overcome by using sacrificial agent which is one of the primary advantages. For instance, when water is the sole reactant along with the photocatalyst, ideally the electrons and holes participate in water splitting. This scheme is partially advantageous due to a simplicity and the environmentally friendly process as no subordinate chemicals are involved. However, this system has significant challenges that includes slower kinetics as water splitting is

an uphill process (ΔG = 285.5 KJ mol−1) than a spontaneous one as discussed in the Chapter 2, section 2.1.3. Thus, resulting in lower efficiency that is a major concern, so it requires a reduction in the redox potential to be governed effectively. When the electron and holes are generated, due to the random migration, the rate of recombination is high. These challenges limit the hydrogen production rate for pure water however the use of SA can guide the charge migration to the surface, quench the electrons or holes and hinder the recombination rate. Therefore, the use of sacrificial agent is highly critical for a feasible and commercial approach towards water splitting.

Addition of SA as an electron donor facilitates the electrons to produce hydrogen that is the half reaction. On the contrary, it can simultaneously quenches the generated holes and reduce oxidation reaction that is the other half of the water splitting reaction to limit the recombination [25]. SA can be categorised as inorganic and organic. For the organic, ethylene diamine tetra acetic acid (EDTA), lactic acid, and a few alcohols such as ethanol and methanol are commonly used. However, the alcohols are valuable industrial products as an industrial fuel thus using them can outweigh the gain [150]. Along with that, Triethanolamine (TEOA) can be used as an effective sacrificial agent. On the other hand, inorganic sacrificial agent containing inorganic ions that can effectively be used, for example SO_3^{2-}/S^{2-}. Sulfides based SA are a common pollutant as a byproduct in hydrogenation and flue gas desulfurization industry this can be economical to be employed. The advantage here is the holes in the valence band will oxidise both S^{2-} and SO_3^{2-} to form S_2^{2-} and SO_4^{2-}. Further, the S_2^{2-} will react with SO_4^{2-} to form S^{2-} and $S_2O_3^{2-}$ this whole oxidisation reaction will continue until the complete consumption of sacrificial agent. The comprehensive multi step mechanism for both SA system is show in Figure 10. However, for this research, the use of sulfur ion-based SA will inhibit the defect formation at the sulfur site for the

MoS_2 co-catalyst. Thus, protecting the overall structural integrity of the photocatalyst and meanwhile $S_2O_3^{2-}$ does have limited adverse effect on the photocatalysis performance [150, 151].

In summary, SA plays serve a crucial role in water splitting. Firstly, they act as hole scavenger preventing charge recombination. Secondly, they serve lower redox potential than pure water which facilitates the dissociation process. Thirdly, the presence of complimentary ion contributing sacrificial agent can improve photocatalyst dispersion stabilise and improve stability thus preventing the deactivation in case of S ions. Therefore, an effective selection of sacrificial agent which compliments the chemical properties of the photocatalyst is the performance determining step in the overall photocatalysis. Hence, another hypothesis regarding the comparative approach and the choice of sacrificial agent between organic or inorganic sacrificial agent will impact the effectiveness of the photocatalyst. So, in our study we used two sacrificial agents 1. 9:1 (v/v) water/TEOA and 2. Mixture of 1.25 M Na_2S + 1.75 M Na_2SO_3 to test our photocatalyst and found that the later produced higher hydrogen yield over TEOA. The hydrogen yield is discussed in the respective chapters to refer.

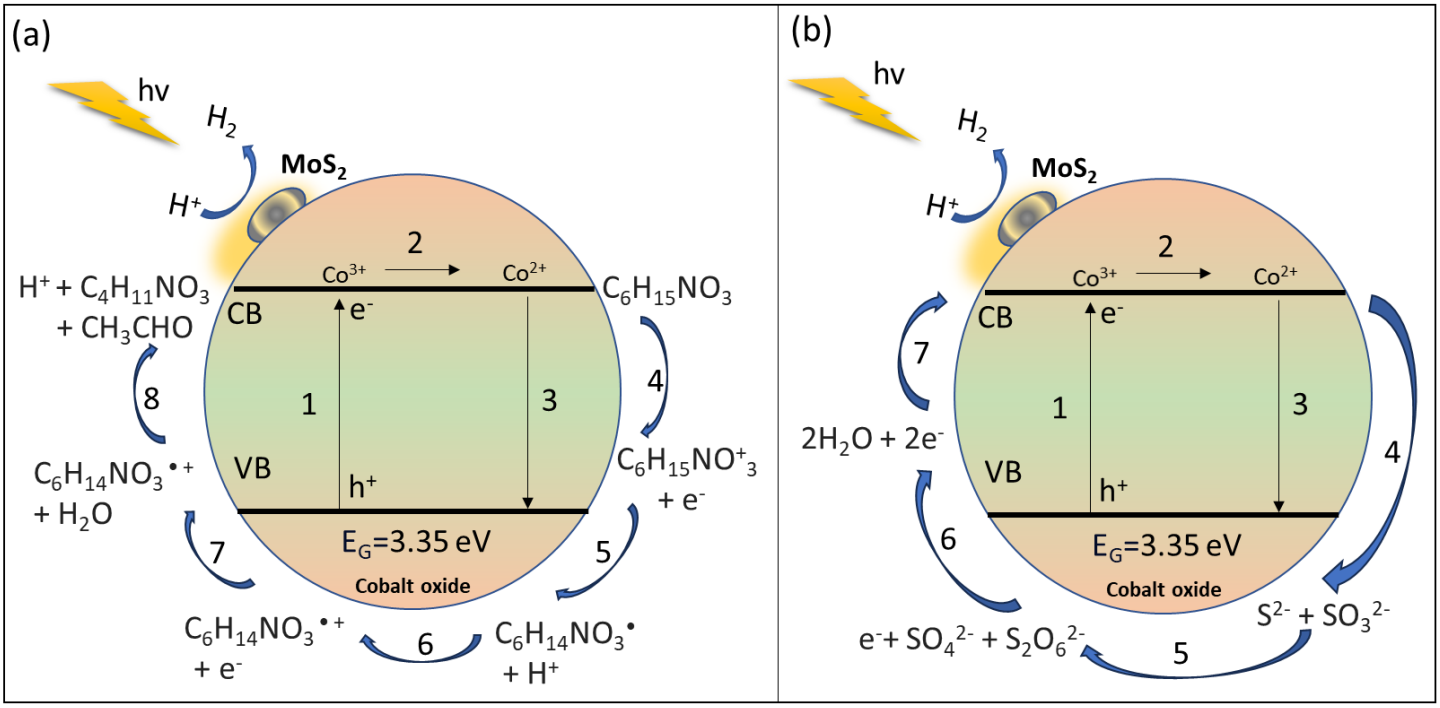

Figure 10: Mechanism on HER for two SA. TEOA (a) and Na_2S + Na_2SO_3 (b)

Therefore, in summary, the above literature review on cobalt based photocatalyst materials present several gaps which will be addressed in this thesis presented in Chapters 3 to Chapters 5.

Gap 1: Reduction in the synthesis time for cobalt oxide that involves, and average for 21 hours based on the data in Table 1, thus proposing microwave irradiation method (Chapter 3)

Gap 2: Enhancing the HER performance by investigating two sets of sacrificial agents (Chapter 4)

Gap 3: Mitigating electron – hole recombination phenomena in cobalt oxide that results in lower HER production, thus proposing Z-Scheme heterojunction with MoS2bulk and MoS2QD (Chapter 3, 4 and 5)

Chapter 3. Microwave synthesised cobalt oxide and molybdenum disulfide quantum dots without sacrificial agents.

These sections have been drafted to be submitted to Applied surface science. The corresponding data is attached in the appendix section contributing to the methodology, experimentation results and discussion on microwave synthesised cobalt oxide and molybdenum disulfide quantum dots in absence of sacrificial agent. The importance of QDs as a future trend has been covered in this manuscript.

Paper 1.

Microwave-assisted MoS_2 QD and cobalt oxide: heterojunction for hydrogen evolution reaction.

Upalee Labhane [a], Zelio Fusco [b], Jia Ding [a], Hashim Jalil Khan [a], Yi-Chen Lin [a], Sarina Sarina [a], David Alam [a], Sergio Londono [a], Alejandro Montoya [a], David K. Wang [a1]

[a] School of Chemical and Biomolecular Engineering. The University of Sydney, New South Wales, 2006, Australia
[b] College of Engineering, Computing and Cybernetics, Australian National University, Canberra, ACT, 2601, Australia.

[1] Corresponding author: David.wang1@sydney.edu.au

Abstract:

This study investigated the hydrogen evolution rate (HER) of water splitting reaction by employing rapid thermal microwave synthesized cobalt oxide and Molybdenum disulfide quantum dots (MoS_2 QD) photocatalysts under simulated sunlight. Cobalt oxide was modified with MoS_2 QD to form a Z-scheme heterojunction leading to quantum confinement and photoluminescence effect. The MoS_2QD-modified cobalt oxide heterojunction achieved a hydrogen evolution reaction (HER) of 1.3 µmol $h^{-1}g^{-1}$ and 1.8 µmol $h^{-1}g^{-1}$ unassisted by a sacrificial agent for modified photocatalyst 0.5QD1p and 1QD1p respectively, which is a performance enhancement of 16.2 and 22.5 times compared to the unmodified photocatalysts 0.07 µmol $h^{-1}g^{-1}$ (cobalt oxide) and 0.08 µmol $h^{-1}g^{-1}$ (MoS_2QD). The combined quantum confinement and photoluminescence effects increased the effective charge separation, reduced band gap energy, improved light absorption, and changed electronic and chemical properties. This study provides insight towards modern rapid thermal routes compared to conventional hydrothermal and solvothermal techniques to synthesize photocatalyst semiconductors for hydrogen generation.

1. Introduction.

Due to its high combustion value, hydrogen has been recognized as a green and zero pollution-causing future fuel utilized in numerous applications, from powering automobiles to heavy industry applications [152]. The industrial scale production of hydrogen currently relies on fossil fuel based feedstocks using mature technologies like hydrocarbon steam reforming [153]. However, due to global environmental concerns and energy security, alternative hydrogen production methods from sustainable sources are actively pursued in research and development worldwide. Water splitting reaction is one of the promising avenues that can be technically achieved with a scale by 1. Electrochemical or 2. Photocatalysis method. [153]. However, both technologies still suffer from several technical challenges including low HER efficiency, material instability, and energy supply, storage and management strategies are areas where research is actively seeking to improve. Nevertheless, photocatalytic water splitting is becoming increasingly popular because of its high feasibility and ease of operation as it relies only on water and solar energy as the input and a semiconductor photocatalyst.

Amongst the semiconductors, cobalt oxides possess a narrowed band gap and excellent capability of absorbing light in the ultraviolet, visible, and near-infrared region light spectrum [154]. Moreover, water oxidation reaction efficiency is enhanced by its optical and electrochemical properties that are mainly attributed to its Co^{2+} and Co^{3+} oxidation species in tetrahedral and octahedral positions and its diverse morphological phases such as Co_3O_4, CoO, CoO_2, Co_2O_3 and cobalt oxalates [99, 155]. The current state-of-the-art focuses on enhancing the light absorption capture efficiency and reducing the charge recombination effects in the cobalt oxide photocatalysts by incorporating modifiers or a co-catalyst to address these fundamental challenges [156].

The use of quantum dots (QD) as a co-catalyst for HER has spiked research interests. QDs are semiconductor materials whose size lies under 10 nm and they exhibit unique characteristics including size tunable bandgap, large surface area, quantum confinement, and excitation photoluminescence [157]. For instance, plasmonic Silver (Ag) nanomaterials were used as combination as $Ag@CoFe_2O_4/g\text{-}C_3N_4$ [105] with Triethanolamine and $Pt/AgTa_{0.7}Nb_{0.3}O_3/Co–Pi$ [94] complex photocatalyst with 20% v/v methanol was used that yielded 33.5 $\mu molg^1\ h^{-1}$ and 12.5 $\mu molg^1\ h^{-1}$ respectively. Due to this, they can absorb a broader range of wavelengths from UV, Vis to NIR region, promote increased light absorption of the base catalyst, and sustained charge migration by reducing the possibilities of electron-hole recombination [158].

The use of noble metal QDs utilizing Ru, Pt, Pd, Ag, and Au have been a prevalent choice in HER as a co-catalyst. Nonetheless, their applicability is limited by both scarce availability and high cost. Thus, on the research endeavor the necessity for exploring alternative commonly available and economically viable non noble QDs for this purpose is the growing need [159].

Recently, molybdenum disulfide (MoS_2) has been studied for HER as a standalone or a co-catalyst [160]. Its multilayer configuration has a sandwich-like structure (S-Mo-S) that features a direct band gap of 1.9 eV, allowing its efficient utilization in visible light spectrum [161]. Notably, the sulfur atom at the edge sites has a strong affinity towards hydrogen and besides this, MoS2 possesses a negative redox potential compared to H+/H2, thus favoring HER [161, 162]. There are several advantages of using QDs over bulk MoS_2 such as a larger surface area contributing to the increase active sites, edge effect, quantum confinement effect and excellent optical properties like photoluminescence (Figure 11 (b) shows the photoluminescence effect under 320 nm light source). As a result, these properties leads to quantized energy levels, enhancements in the electron-holes

charge transfer, carrier mobility and charge separation efficiency rendering MoS_2QD an effective co-catalyst for HER [131].

Figure 11 L-R, Microwave synthesized QD (a), and QD showing photoluminescence effect under 320nm light (b).

The application of microwave heating technology is becoming a reliable modern technology in material synthesis. Unlike conventional heating techniques, microwave offers an efficient and uniform heat profile within the sample that contrasts with the heat transfer from container walls to the sample as observed in conventional heating [163]. Another distinctive benefit of microwave is its immediate quenching effect upon stopping the magnetron power that contributes to forming metastable reaction products enhancing the overall material properties [164]. As shown in Figure 12, microwave and conventional techniques' heating dynamics demonstrate notable contrast. Initially, from the starting point t1 to t3, a rapid temperature rise is demonstrated in the microwave profile however, at t3 the comparative heating for conventional technique is significantly lower.

These heating profiles underscore the microwave technique's potential in reaching higher temperatures in shorter reaction time.

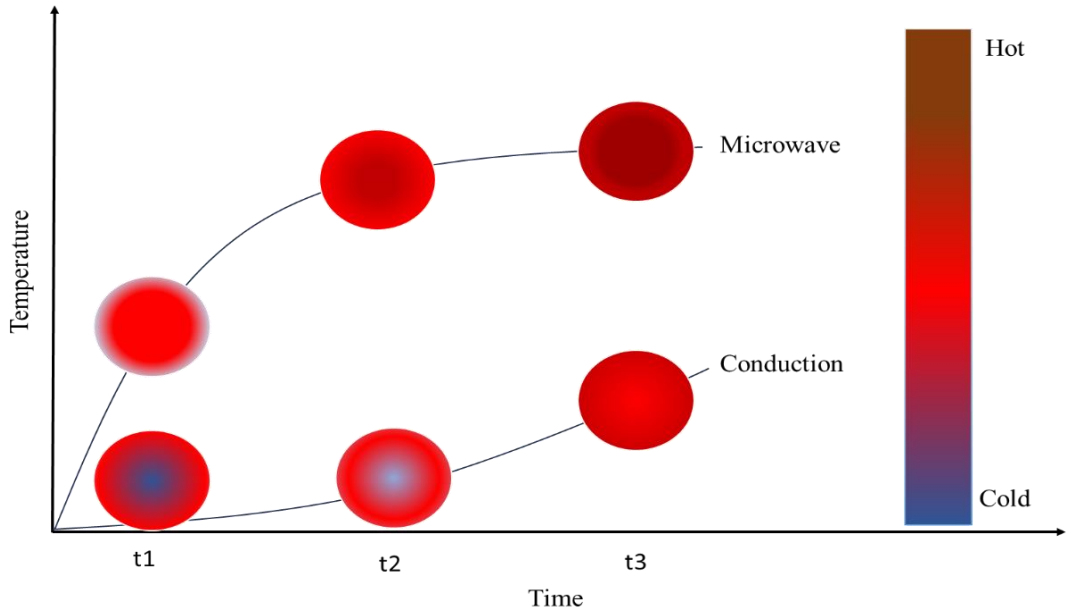

Figure 12 The temperature profile vs. time of microwave and conduction heating at different points in time.

Recent research finding support efficacy of the reduction in reaction time and temperature by using microwave for metal oxides like, $La_{1-x}Sr_xCoO_3$, $Li_{0.35}La_{0.55}TiO_3$, and cobalt oxide [165, 166]. An illustrative example that highlights the enhanced photocatalytic properties of α-Fe_2O_3 when synthesized using microwave as compared to conventional heating is studied by Saremi et al., (2013) [167]. According to this research, the reason for improved performance includes the accelerated reaction kinetic that resulted in unique bond formation leading to enhanced structural stability. The purity of the final product is influenced by magnetron power that is proportional to the heating rate thus faster reaction kinetic produces purer products [168]. Another component to expedite the synthesis process is the use of polyvinyl alcohol (PVA) as a precursor that played a

critical role in altering the cobalt oxide's chemical and morphological properties. PVA being characterized by it semi-crystalline nature initially it acts as a template for guiding the shape and size during the nucleation process [169, 170]. In our case it resulted information of both rode and sphere like structures. Then influencing the crystal formation through impacting the crystallization kinetics that accelerates the synthesis of the photocatalyst [171] And lastly, it served as a linking agent that bridges the base and co-catalyst thus enhancing the overall stability of the heterojunction [170].

In this study the use of microwave technique is explored for the synthesis of cobalt oxide and MoS_2QD that represents a significant novelty. The unmodified consisting of varying PVA concentration (0.5 – 2wt%.) and modified Z-scheme heterojunction photocatalyst with different QD concentrations was evaluated for HER without sacrificial agents.

2. Experimental section.

2.1 Materials.

Unless specified otherwise, all chemicals were purchased and used as received from Sigma Aldrich. Cobalt oxide (99.5% trace metal basis) <50 nm particle size, Cobalt nitrate hexahydrate (ACS reagent, ≥ 98%), potassium oxalate monohydrate (ACS reagent, 99%), Polyvinyl alcohol (99+% hydrolyzed), sodium hydroxide (reagent grade, ≥98%), Ammonium tetra-thiomolybdate (99.97% trace metals basis), Hydrazine hydrate (reagent grade, N_2H_4 50-60 %), and Ethanol (ACS reagent, ≥99.5%) was diluted with DI water to make a 50% v/v ratio, Triethanolamine (purity≥99.0%) were used.

2.2 Material Characterization.

Powder X-ray diffraction (XRD) patterns were recorded by PANalytical X'Pert3 powder diffraction. For which the *d* -spacing was calculated using the Bragg's Law formula, $\lambda = 2d \sin\theta$, where λ is the wavelength (1.54 Å for Cu Kα) [172]. UV-Vis-NIR Spectrophotometer UV-3600 with triple detectors from Shimadzu was used for light absorbance spectroscopy. CHI electrochemical workstation (532 nm laser) apparatus with 3 electrode system and a 0.5 M Na_2SO_4 electrolyte and a Ag/AgCl electrolyte was used for photoluminescence. Nicolet 6700 FTIR Spectrometer from Thermo Fisher and the spectra was collected at a resolution of 4 cm^{-1} between 500 – 4000 cm^{-1} for functional group identification. Thermo Fisher K-Alpha+ XPS/UPS were used for the chemical composition of the photocatalyst.

2.3 Microwave-assisted Cobalt Oxide Synthesis

The stoichiometric equivalent of 30 mL of 2 M $Co(NO_3)_2H_2O$ and to that of 30 mL of 2 M $K_2C_2O_4$ solution was added dropwise and stirred for 15 minutes at 500 rpm for uniform mixing. Then, 90 mL of PVA suspension (0.5, 1, 1.5, 2 wt% i.e., 0.075, 0.15, 0.225 and 0.3 M PVA,) was added with stirring for 10 minutes, followed by the addition of 1.2 mL of 1M NaOH solution and stirred for 5 minutes. The final suspension was reacted for 2 minutes under microwave irradiation using 900 Watts (W) and 200°C. The rationale behind using these modified specific ratios is the occurrence in of the early papers in MW technology mentioned in the work by Ai, Lun Homng et. al (2009) [173] where they worked on the early MW technology and synthesised cutting egde research that reduced the cobalt oxide's synthesis time to 2 minutes and further by Kandu et. al (2013) [174] where they investigated the effect of PVA on the shape and size of the cobalt oxide nanomaterials. By combining both the studies, we were able to synthesis and select the most desired and best performing cobalt oxide nanomaterial.

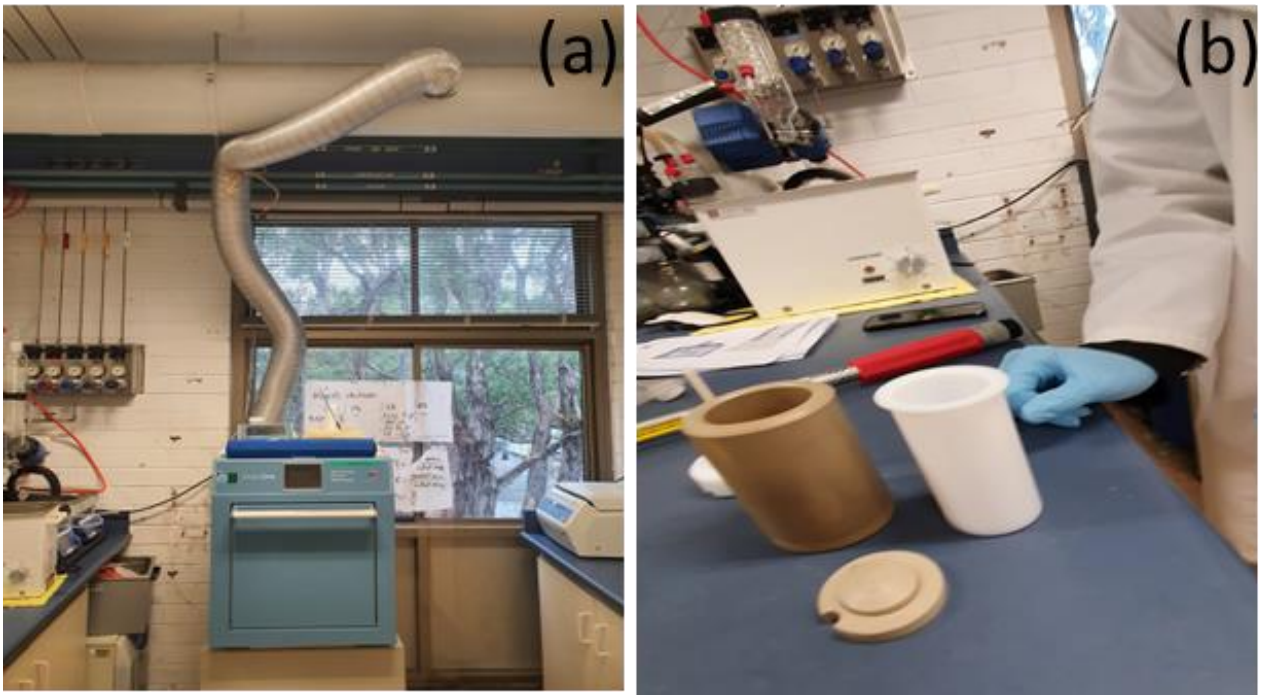

Figure 13 (a) shows the microwave setup that includes the manufacturer as Milstone and model name as EthosOne with a produced gas exhaust at the top and the whole system is powered by 2500 W magnetron. The

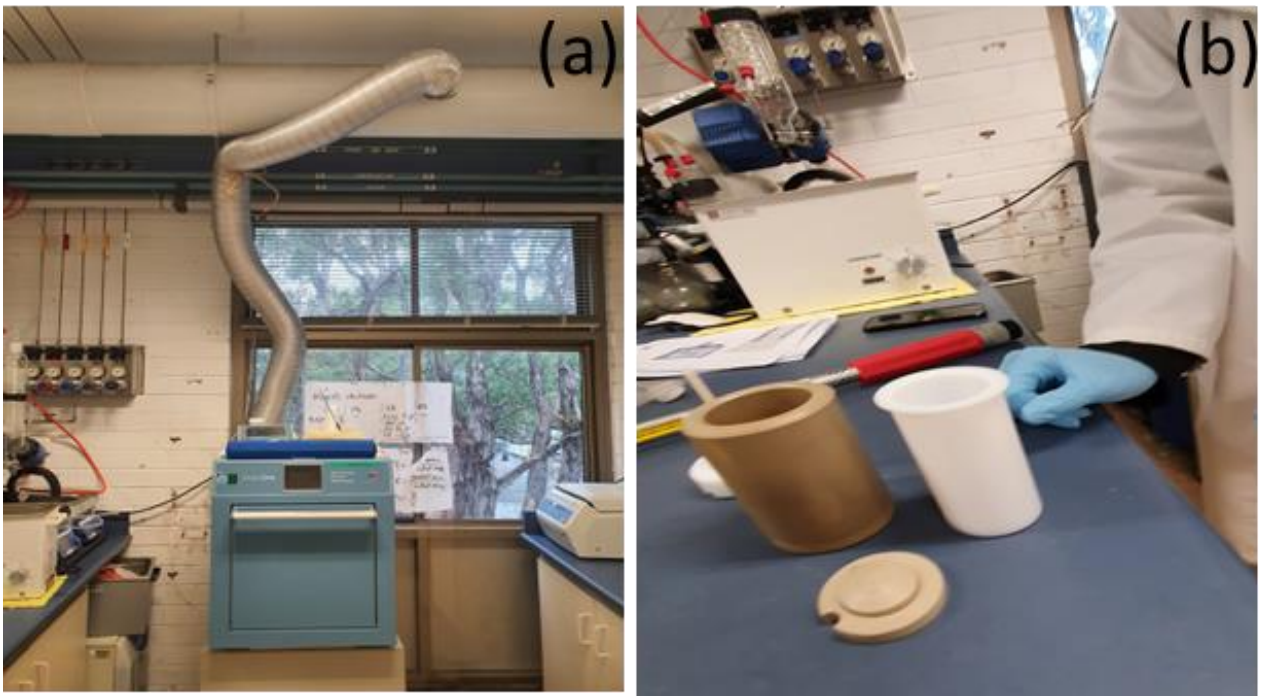

Figure 13 (b) represents the vials that hold the chemicals. The main components are the out covering that houses the inner polyethylene 100 ml tube. This vial is also equipped with a temperature and pressure probe. The experiments were carried out in a lead closed state, however, air was not vacuumed nor it was replaced with other gas.

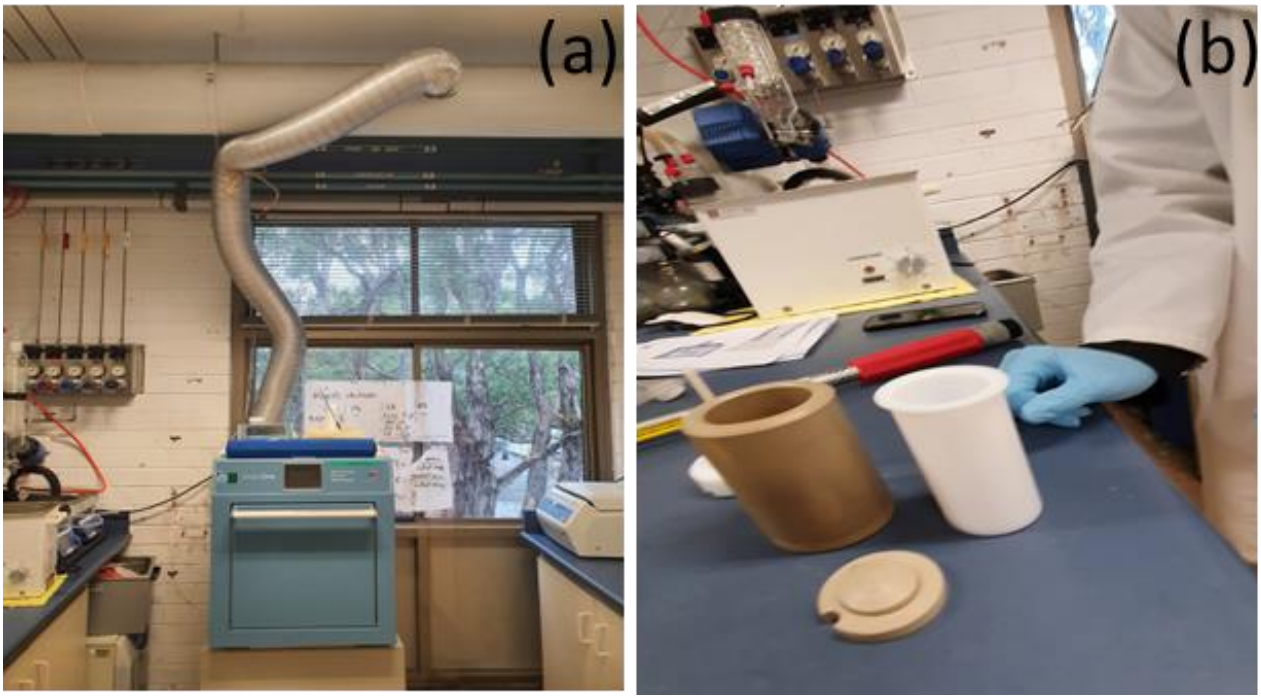

Figure 13 Microwave setup.

The final solution with cobalt oxide nanomaterials was centrifuged at 5000 rpm for 5 minutes and the product was washed 3 times with drying at 60 °C overnight.

2.4 Microwave-assisted MoS_2 Quantum Dot Synthesis

The synthesis process was adopted from a previously reported article [175], where 0.05 g of ammonium tetrathiomolybdate ($(NH_4)_2MoS_4$) powder was added to 20 mL, 50% v/v ethanol solution and stirred for 1 hour. Then 1 mL hydrazine hydrate (H_6N_2O) was added and stirred for 5 mins and this solution was reacted under microwave at 1000W, 200°C, for 10 minutes. The

obtained solution was centrifuged at 5000 rpm for 5 minutes and then the obtained quantum dots were washed with 50% ethanol solution 3 times and dried at 60°C overnight.

2.5 Preparation of Z-scheme heterojunction of Cobalt oxide and MoS_2 Quantum dots.

To prepare heterojunction with MoS_2QD, cobalt oxide containing varying PVA concentration were weighed and added in 100 mL ethanol respectively and to that, a corresponding amount of MoS_2QD was added to make the respective heterojunctions, 0.5, 1.0, 1.5 wt% MoS_2. This suspension was stirred for 24 hours at 500 rpm and later centrifuged and dried at 60 °C overnight. Table 2 below represents the photocatalyst matrix with varying PVA and QD concentrations. In Table 2, 'p' corresponds to PVA concentration and 'QD' corresponds to MoS_2QD concentration. Catalyst matrix with varying PVA concentration and varying QD concentration.

Table 2 The photocatalytic matrix with varying PVA concentration and QD to denote definite the heterojunctions.

Sample Code	MoS2 QD (wt%)	PVA (wt%)
Commercial Co3O4	-	-
QD	1	0
0.5p	0	0.5
1p		1
1.5p		1.5
2p		2
0.5QD1p	0.5	1
1QD1p	1	
1.5QD1p	1.5	
1QD0.5p	1	0.5
1QD1p		1
1QD1.5p		1.5
1QD2p		2

2.6 Photocatalytic measurement.

The customized online gas analysis setup used is shown in Figure 14. In a typical water splitting experiment, 50 mg of the photocatalyst was dispersed in a borosilicate glass reactor with a quartz window on the top filled with 100 mL deionized water at 25°C and atmospheric pressure. The light irradiation time was fixed at 12 hours and the produced gas was measured after the experiment. The produced gas was passed through a cooling chamber to capture the moisture and then analyzed by an Agilent micro-GC (Varian 490) with a thermal conductivity detector (TCD, 5 Å molecular sieve column). A mass flow controller (Alicat USA) was used to flow 30 SCCM of Argon as a sweep gas was passed through the glass reactor to carry the generated gasses to the GC for analysis. A 300 W Xenon light bulb (xh400) sourced from Aulight China, fitted with a filter (λ <420) was used for photocatalytic reaction.

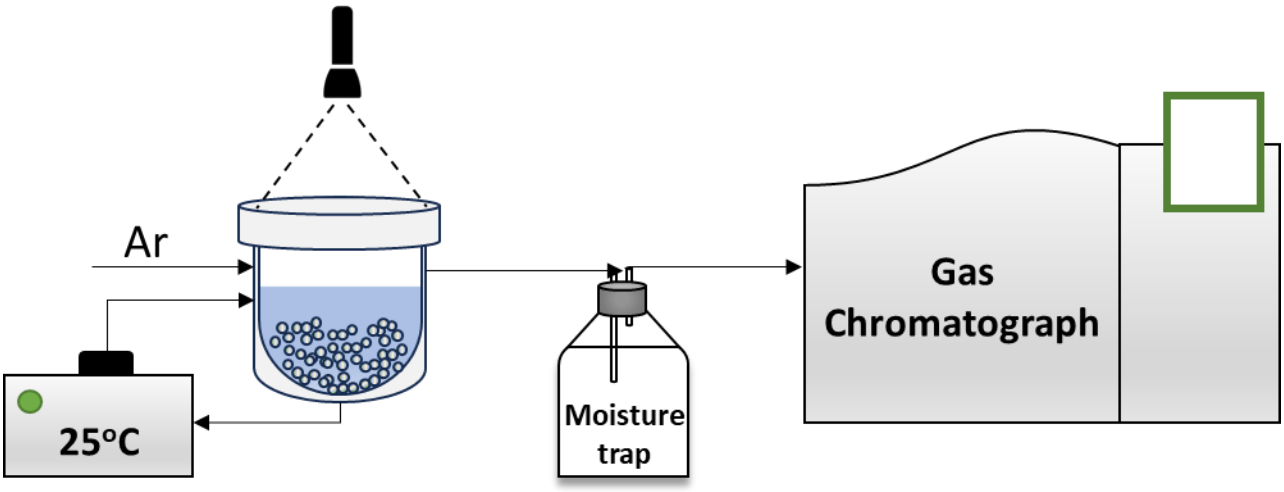

Figure 14 Customized online hydrogen gas reactor (quartz on the top) with a moisture trap to absorb water before entering the GC.

3. Results and discussions.

3.1 HER performance of the synthesised cobalt oxide and MoS_2 heterojuntion:

Sigma Aldrich source commercial cobalt oxide, Co_3O_4 was used as the comparison catalyst. The hydrogen production of 0.04 µmol $h^{-1}g^{-1}$ was recorded for the Co_3O_4 photocatalyst. In the unmodified cobalt oxide PVA series, 0.5p and 1p outperformed the commercial sigma photocatalyst with hydrogen production of 0.06 µmol $h^{-1}g^{-1}$ & 0.08 µmol $h^{-1}g^{-1}$ while the 1.5p and 2p photocatalyst lower yield as shown in Figure 15 (a). In the first PVA series 1p outperformed the rest of the unmodified photocatalyst samples, which was then used as a base photocatalyst for further modifications with different concentrations of QD. An overall increment in the hydrogen production rate is recorded for all modified heterojunction samples as compared to unmodified. The following experiment tested the series depicted in Figure 15 (b), which involved varying the concentration of QDs., initially 0.5QD1p showed increased performance with 1.3 µmol $h^{-1}g^{-1}$ which is 16.2 times high over unmodified 1p and the highest recorded value for 1QD1p was 1.8 µmol $h^{-1}g^{-1}$ which is 22.5 times increase in hydrogen production rate. However, for 1.5QD1p the higher concentration of QD showed a negative effect where the QDs acted as the recombination sites thus reducing the HER yield. Here, the pure QD performed lowest with the value of 0.07 µmol $h^{-1}g^{-1}$. In the second series of experiments the highest yielding exemplified by 1QD1p was tested against varying concentrations of PVA as shown in Figure 15 (c). Interestingly, the trend mirrored the observations from the unmodified PVA series where 1p sample constantly outperformed the other PVA samples.

The lower hydrogen production of all unmodified photocatalysts is attributed to the cobalt oxide's affinity towards electron hole recombination, potential oxidation photocatalyst and limited light spectrum absorbance. However, the pure QD also presumably suffered from rapid electron hole recombination, so it was concluded that the standalone cobalt oxide and QD do not show

comparable results as modified photocatalyst. This indicates that synthesized Z-Scheme heterojunction can overcome the limitations of standalone photocatalyst by possessing better electron hole recombination properties. The migration of the electrons from the conduction band of the cobalt oxide to the valance band of the QD is driven by the difference in their redox potential. Also, improved optical properties for both light absorption and narrowing of the band gap by 0.05 eV for the modified samples. Along with that the change in the electronic properties by increases Co^{3+} species, and lattice compression shown in XPS and XRD analysis respectively. These listed observations will be discussed below in the relevant analysis sections.

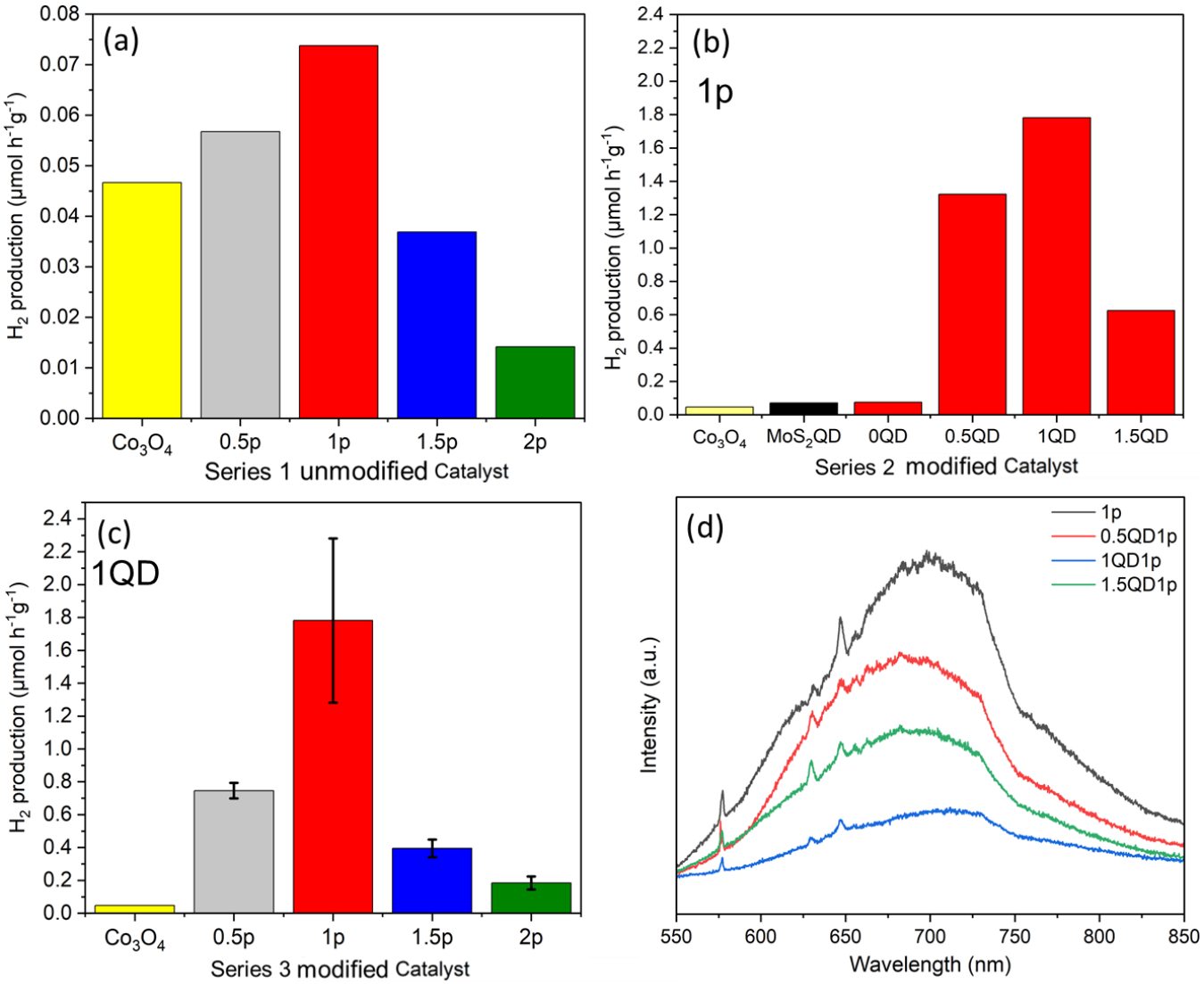

Figure 15. Hydrogen evolution performance for unmodified and modified photocatalyst along with PL spectra. (Left to right) unmodified cobalt oxide with comparison commercial cobalt oxide (Co_3O_4) (a) where the use of commercial photocatalyst lays a ground for comparison to the synthesised photocatalyst, Figure (b, 1p is chosen to be the best photocatalyst in the unmodified series and further modified with varying QD Concentration along with pure QD where 1QD1p outperformed. Figure (c) depicts the 1QD modifications with the unmodified series to investigate the effect of 1QD on other concentrations of PVA in series 1. The error bars in (c) is reported as a function of mean and standard deviation based on 3 sets of experiments.

3.1 Photoluminescence (PL)

The PL technique is employed to investigate the photocatalyst's charge separation and electronic-hole combination characteristics. In Figure 15 (d), the QD modification has increased the charge separation efficiency in the heterojunction that is due to the quantum confinement effect, photoluminescence and the formation of Z-scheme heterojunction compared to unmodified 1p [176]. A blue shift of ≈15nm and an overall peak broadening is observed from 650 nm to 725 nm in the modified samples. The PL intensity increment is in the order of 1QD1p < 1.5QD1p < 0.5QD1p <1p. So, we can conclude that 1QD1p has the lowest charge recombination rate and this analysis is well translated to its highest performance for HER. Another conclusion is that increasing the concentration from 1QD to 1.5QD decreases the charge separation because the addition QD acts as a site for exciton recombination rather than adding more electrons-holes, which is also evident in HER performance [30]. Thus, 1QD is the optimum doping amount that is beneficial for the catalyst performance reviewed hereinafter.

3.2 UV Vis NIR

The optical study covers the light spectrum from 200 nm to 1600 nm. Figure 16 shows the photo-response of unmodified 1p and modified heterojunction. The unmodified and modified samples show a wide light absorption spectrum from 200 to 1600 nm with varying intensity as a general observation. A sharp slope at 340 nm is due to the band gap transition of cobalt oxide with another minor slope at 560 nm that can be attributed to varying structural morphology (rod and spear), confirmed by the SEM image (Figure 23). A decrease in intensity is seen within the range of 800 to 1000 nm, followed by a successive increase as the spectra extended to the near-infrared region between 1000 – 1600 nm. Modification with QDs has enhanced the light absorbance, and a pronounced a blue shift is prominently evident within 400-750 nm range. This shift can be

attributed to the quantum confinement and edge effect inherent of QD size thus reducing the interlayer coupling [177, 178]. This observation underlines that the QD's size has impacted the optical properties of 1p photocatalyst. The light spectrum of 1QD1p initially showed lower light absorption in the lower UV region than 1p. However, beyond the 320 nm range, there was an evident increase in light absorbance, into the visible range and extending to the near-infrared (NIR) region. Certainly, the lower absorbance in the UV range is not likely to impact the HER because the employed light source is equipped with a filter limiting the wavelength below 420 nm. The extended spectra in the NIR region can be attributed to thermal effects arising from the photoluminescence and quantum confinement phenomenon [179]. This then results in producing more electrons in proportion to the light absorbed that are beneficial for HER [180]. The light absorbance spectra of 1.5QD1p showed the highest light absorbance, but its performance is limited by electron-hole recombination property that is inferred from the PL analysis.

The band gap of the samples were calculated using Tauc formula where the linear relation (ahν)^2 against hν was plotted. The band gap of 1p was calculated to be 3.41 eV, which narrows to 3.36 eV upon QD modification. This reduced band gap may be attributed to the facilitated charge exchange from O^{2+} to Co^{3+} facilitated by the induced quantum confinement effect [181]. This narrowing of the band gap is extremely advantageous as it implies that the heterojunction can effectively harness a broad range of the light spectrum, thus enhancing the generation of photo-excitons [182]. When combined with the PL analysis, these derived observations, particularly for 1QD1p, provide valuable insights on comprehending that the heterojunction not only absorbs a superior amount of light but also facilitates an enhanced charge separation and critically contributes to higher overall performance.

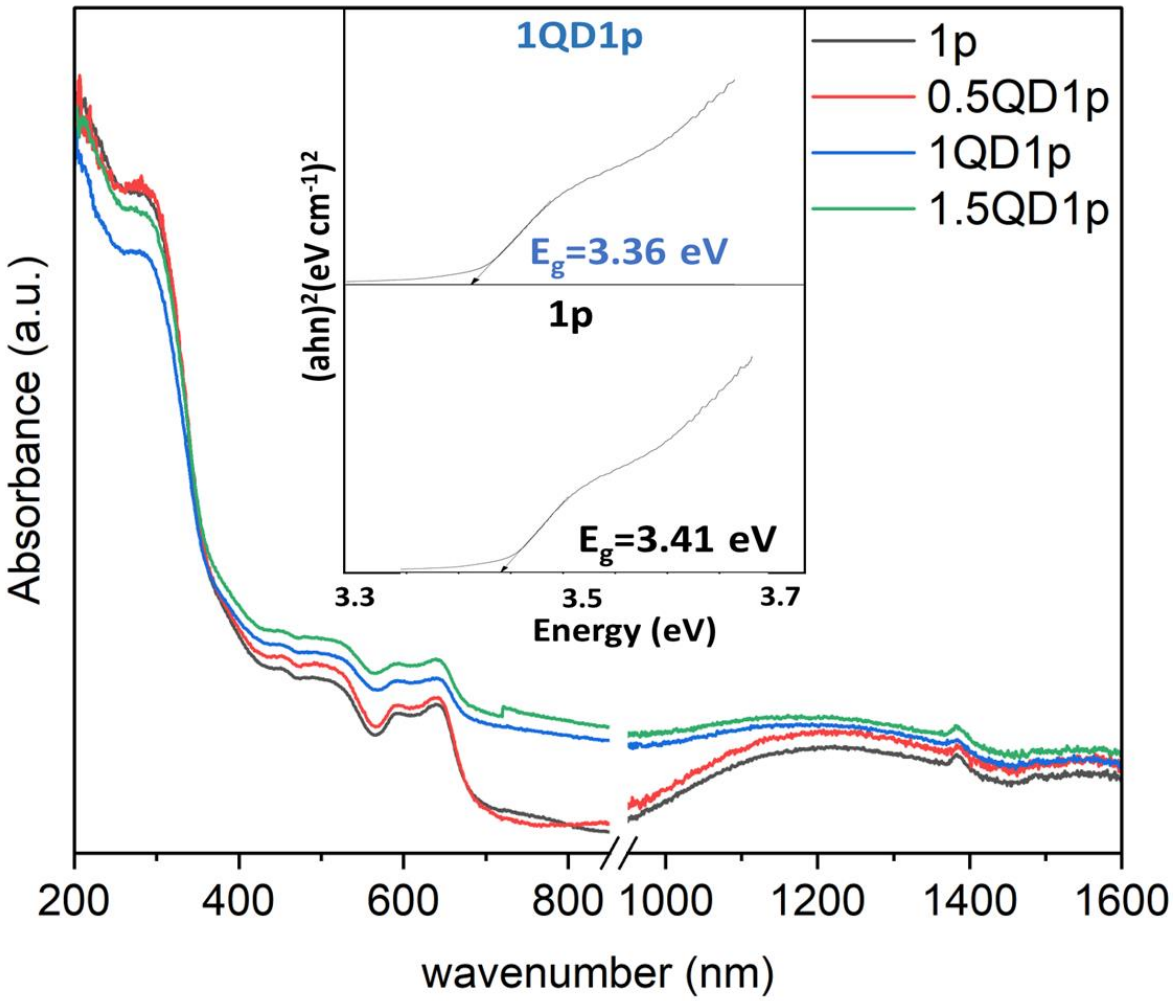

Figure 16 UV Vis NIR absorbance spectra {insets change in band gap of 1p (black colour) and 1QD1p (blue colour) showing the reduced band gap energy.

The XRD spectra of unmodified 1p sample is shown in Figure 17 (a) that has two major cobalt peaks observed at 18.7° 2θ and 19.1° 2θ. Specifically, the peak at 19.1° 2θ associated to (111) plane is complimented by a minor peak at 33.9° 2θ (440) indicating the monoclinic structure for cobalt oxide (Co_3O_4) [183, 184]. Furthermore, the remaining major peaks at 18.7° 2θ, complimented by 30.3° 2θ and 35.0° 2θ corresponds to the orthorhombic crystalline structure of

cobalt oxalate. [185, 186]. In addition to the above cobalt peaks we also observed PVA characteristic peaks at 22.8° 2θ and 40.4° 2θ [187]. The semicrystalline PVA peak range is 20° 2θ to 30° 2θ but because of the overlapping by the obvious cobalt peaks, the PVA peaks are superimposed, however the presence of shoulder peak at 22.8° 2θ confirms the presence of PVA [188, 189]. After the modifications, it is noted that the peak position remains unchanged. Also, the MoS_2 characteristics peaks remain undetected upon introducing QD which is reasonable because of the absence of constructive interference within the formed crystals [190]. Notably, the lattice peak at 19.1° 2θ (111) has been compressed from 6.33 Å to 6.05 Å after modification. This lattice shrinkage is due to the addition of smaller sized QD (Figure 24) [191]. The XRD spectra of commercial Co_3O_4 and MoS_2QD is shown in Figure 25.

3.4 X-ray photoelectron spectroscopy (XPS)

The XPS was used to investigate the surface chemical composition of the photocatalyst sample. The survey spectrum confirms the existence of cobalt, oxygen, molybdenum, and sulfur shown in supplementary data S6. After modification, the Co2p spectra exhibited a 2 eV red shift depicted in Figure 17 (b). This observation is evidence of the change in chemical environment and also in electronic configuration in the cobalt species arising due to the modification by QD [192].

The Co2p spectrum identifies two distinct characteristic regions (Co2p $_{3/2}$ and Co2p $_{1/2}$) that are separated by 15.5 eV. Between this range, the Co $2p_{3/2}$ peak at 783.1 eV corresponds to Co^{3+} and 785.5 eV corresponds to Co^{2+} [193]. These observed cobalt species can be attributed to either cobalt oxide or cobalt oxalate where the cobalt bonding with the oxygen is in form of a carbonyl species [193]. The later region of Co $2p_{1/2}$ was deconvoluted at 797.4 eV corresponding to Co^{3+} and 799.1 is corresponding to Co^{2+} [194]. We observed two satellite peaks at 787 eV and 804 eV shaded in yellow and cross lined well after the Co^{2+} [195]. In this case, the presence of Co2p is

associated with d electron that can be linked with the presence of oxygen in the vicinity, implying the presence of either cobalt oxide or oxalate and both can contribute to the Co2p spectrum [196, 197]. The ratio of Co^{2+} : Co^{3+} species of the unmodified 1p sample were calculated as 1:4 and after modification the Co^{3+} species have been increased in its concentration to 1:3.5. In general, the Co^{3+} species exhibit higher reactivity and readiness to transfer charges as compared to the Co^{2+}. Furthermore, Co^{3+} species can alter the photocatalyst's electronic structure, resulting in enhanced performance [198]. The distinctive oxygen peak at 533.5 eV can be assigned to the hybridization of oxygen O1s and this peak can be attributed to eighter cobalt oxide or oxalate but prominently the Co-O bond likely be originating from the oxalate component [199, 200]. This observation supports the results from XRD analysis that indicated the occurrence of mixed cobalt composite of Co_3O_4 and cobalt oxalate. The peaks at 228.1 eV and 232.4 eV deconvolutes to represent Mo^{4+} in its $3d_{5/2}$ and $3d_{3/2}$ oxidation states respectively [201]. Also the large observed peak at 235.2 eV corresponds to Mo^{6+} and the peak at 237 eV is a Mo-O satellite peak [202, 203]. This satellite bonding peaks confirm the interaction between cobalt and MoS_2. Whereas the S1p weak peaks detected at 161.88 eV ($S2p_{3/2}$) and 162.9 eV ($S2p_{1/2}$) is showing the divalent sulfide ions [204] and the larger peak at 169.9 attributes that the S_2p bond structure that is formed as S-O bond [205].

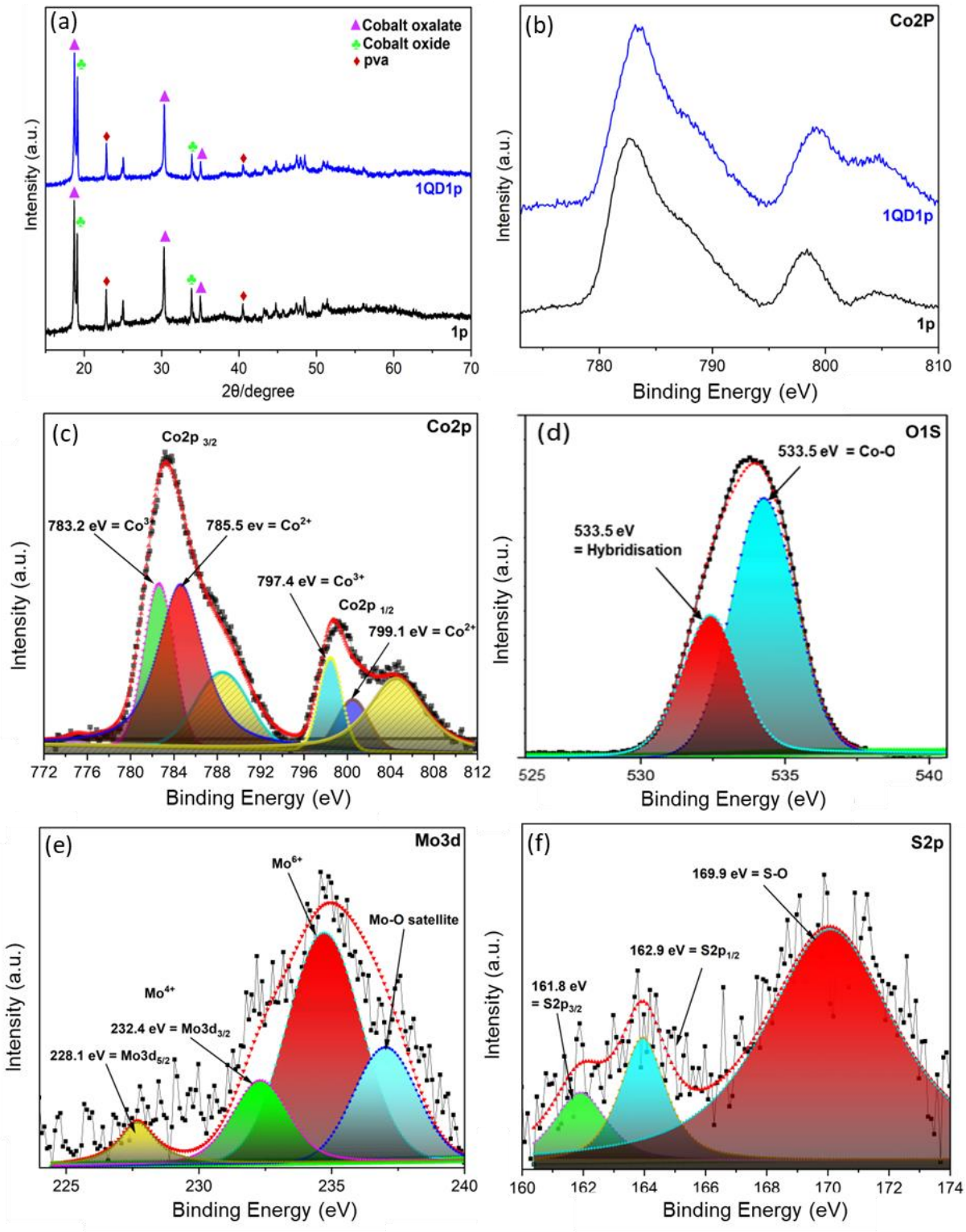
(a)
Cobalt oxalate
Cobalt oxide
pva
1QD1p
1p
Intensity (a.u.)
2θ/degree
(b)
Co2P
1QD1p
1p
Intensity (a.u.)
Binding Energy (eV)
(c)
Co2p
Co2p 3/2
783.2 eV = Co3+
785.5 ev = Co2+
797.4 eV = Co3+
Co2p 1/2
799.1 eV = Co2+
Intensity (a.u.)
Binding Energy (eV)
(d)
O1S
533.5 eV = Co-O
533.5 eV
= Hybridisation
Intensity (a.u.)
Binding Energy (eV)
(e)
Mo3d
Mo6+
Mo-O satellite
Mo4+
232.4 eV = Mo3d3/2
228.1 eV = Mo3d5/2
Intensity (a.u.)
Binding Energy (eV)
(f)
S2p
169.9 eV = S-O
162.9 eV = S2p1/2
161.8 eV
= S2p3/2
Intensity (a.u.)
Binding Energy (eV)

Figure 17 Chemical properties of photocatalyst. (a-f), XRD spectra for varying 1QD1p and 1p sample (a), Co2p redshift for 1QD1p sample (b), deconvoluted Co2p 1QD1p (c), deconvoluted O1s 1QD1p Molybdenum (d), deconvoluted Mo3d 1QD1p (e), deconvoluted S2p 1QD1p (f)

3.5 Fourier transform infrared spectra (FTIR):

The FT-IR spectra was used to study the functional groups in unmodified 1p and 1QD1p that is shown in Figure 18. Also, the commercial Co_3O_4 and MoS_2QD are shown in Figure 22. For 1p samples the bond group observed between 3230 cm^{-1} - 3550 cm^{-1} can associated to eighter an amine functional or OH group, but noting the nature of the peak maxima at 3346 cm^{-1} which is not sharp as typical amine groups but is broad enough [206]. Thus, we confirm this peak as OH bond along with a carbon shielded hydrogen atom from cobalt nitrate hexahydrate, one of the precursors [206]. The two peaks at 1314 cm^{-1} and 1358 cm^{-1} are the alcohol group (-OH) from PVA [206]. A strong peak at 1613 cm^{-1} is a carbonyl function group present in potassium oxalate [206]. The two distinctive cobalt oxide peaks at 587 cm^{-1} , ~ 737 cm^{-1} are indicative of cobalt oxide (Co-O) as these peaks are linked to the stretching vibrational mode of Co^{+3} and coordinates as octahedrally metal ions [207, 208]. In addition a complimenting peak at 823 cm^{-1} is associated with (O-C-O) that indicates abridging oxalate group (orthorhombic) [209]. After modification, all the peaks show heightened intensity and sharper profiles accompanied by minor shifts in the peaks due to the change in the environment owing to the presence of QD. It is noteworthy to identify these changes, but they are not significant enough to be claimed as a new bond however we observe two noticeable changes. Firstly, a blueshift for the OH bonding at 3347 cm^{-1} and an increased peak height. This change is certainly due to the stirring process in the modification step involving ethanol. The same effect was observed by Yimlamai et al., (2011) [210] where they observed the bond stretching and peak enhancement around 1614 cm^{-1} associated to the carbonyl group (H-O-

H). for the 1QD1p sample, this peak corresponds to potassium oxalate along with the increment in the peak at 3347 cm-1 associated with OH. The other main difference is observed in the dissociation of 1380 cm^{-1} peak, corresponding to the Co-O-H which experienced bond breakage, creating a different Co bonding [211].

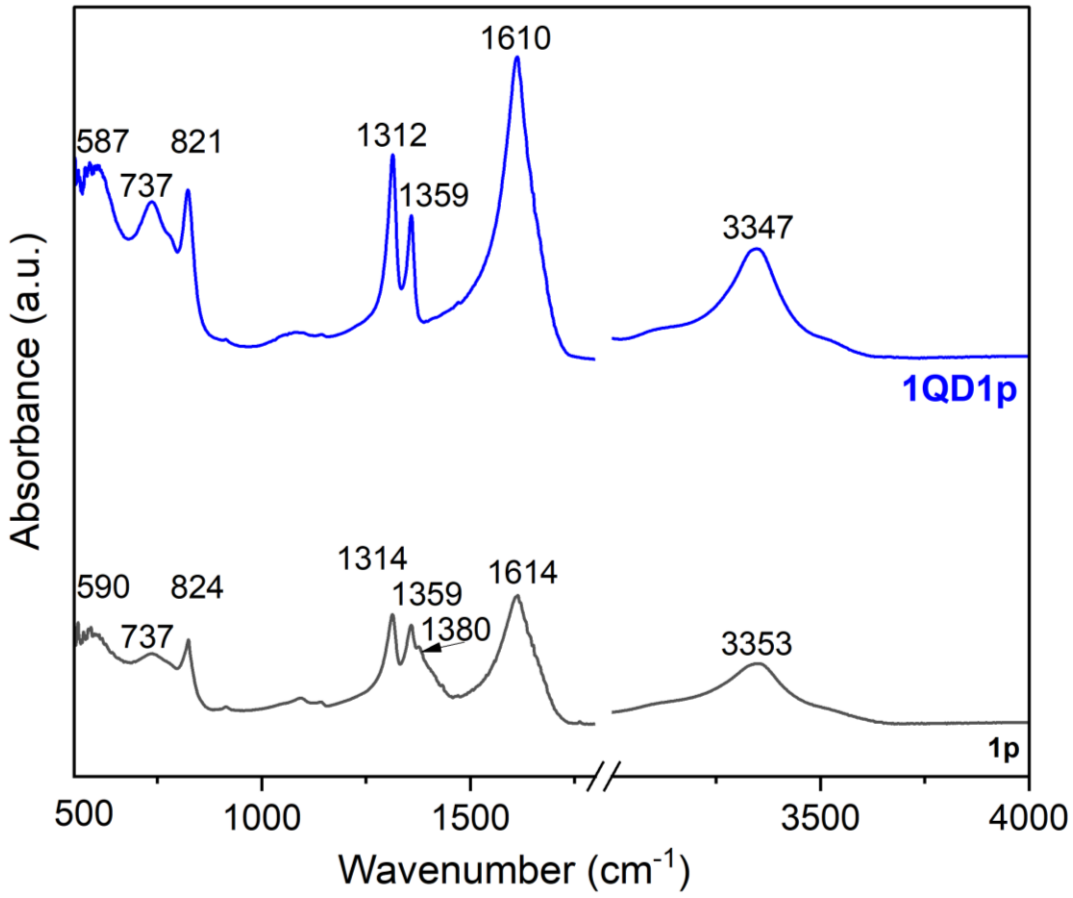

Figure 18 FT-IR of unmodified 1p and 1QD1p cobalt oxide.

3.6 Transmission electron microscopy (TEM):

The morphology of the samples 1p and 1QD1p was studied using TEM that is shown in the Figure 19 along with selected area electron diffraction pattern (SAED). The Figure 19 (a) shows the

agglomerated QDs that can be seen in the form of spheres and the attached insets is the elemental mapping where trace molybdenum (Mo) and sulfur (S) is observed. The rod like structure of 1p to which spherical QDs are physically attached can be seen in Figure 19 (b) and elemental mapping of Co in Figure 19 (f). This attachment is likely attributed to van der Waals force of attraction between the two surfaces [212]. Investigating this further, the elemental mapping shows the presence of Mo and S elements confirming the existence of the QD in Figure 19 (d) and (e). The Figure 19 (c) is the SAED pattern index the crystalline structure of 1QD1p where the diffraction rings are sharper for crystal lattice 111 and 440 and presence of bright spots near plane 111 refers to the metallic Co [213]. TEM of the other sample presented in the literature also agrees with the reported size that is the average width to be around 80 nm to 270 nm and length may vary to several microns [173, 174]

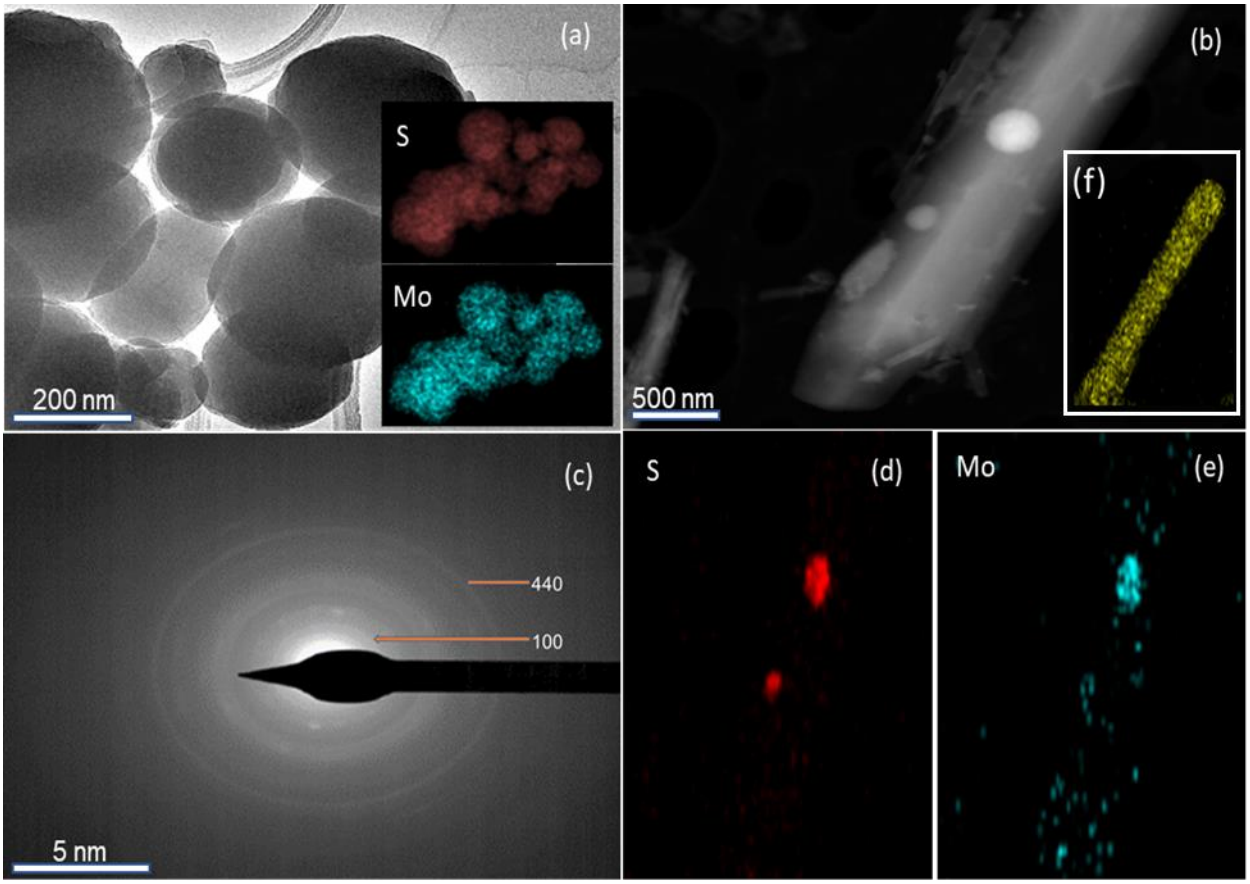

Figure 19 TEM images. (L-R) (a) Pure MoS2 QD (EDX insects: Mo, S elements), (b)Modified cobalt oxide (EDX insect: Co element (f)), (c) SAED for MoS2 QD, (d,e) EDX for modified cobalt oxide showing S, Mo element.

3.7 Photocatalytic Mechanism:

The illustrative representation of charge migration and recombination pathways is shown in Figure 20 (a). In the unmodified 1p sample, a complex network of pathways exist that contributes to undesired charge recombination due to the shorter distance between them and charge attraction. This leads to the recombination phenomenon identified as surface and bulk recombination. This phenomenon has significant implications as it consumes the electron and limits its interaction towards reducing the water molecule, resulting in a reduction in the efficiency of the HER.

Conversely, the modification with QD shown in Figure 20 (b) demonstrates the Z-Scheme mechanism of enhanced charge separation. This is achieved by facilitating the charge migration (e^-) by promoting the electron migration from the conduction band (CB) of 1p to the valance band (VB) of the QD. This migration is facilitated by the favorable reduction potential of MoS_2 compared to 1p (cobalt oxide) and additionally the presence of more active sites contributes towards improved charge separation [214, 215]. Hence, it is reasonable to infer that the electrons will predominantly travel to the QD rather than the opposing direction. That implies the interfacial charge transfer operates from 1p to 1QD1p because of the Z-scheme mechanism. Therefore, it can be concluded that the enhanced performance of the modified photocatalyst is the result of the optimal interaction between QD and 1p [181].

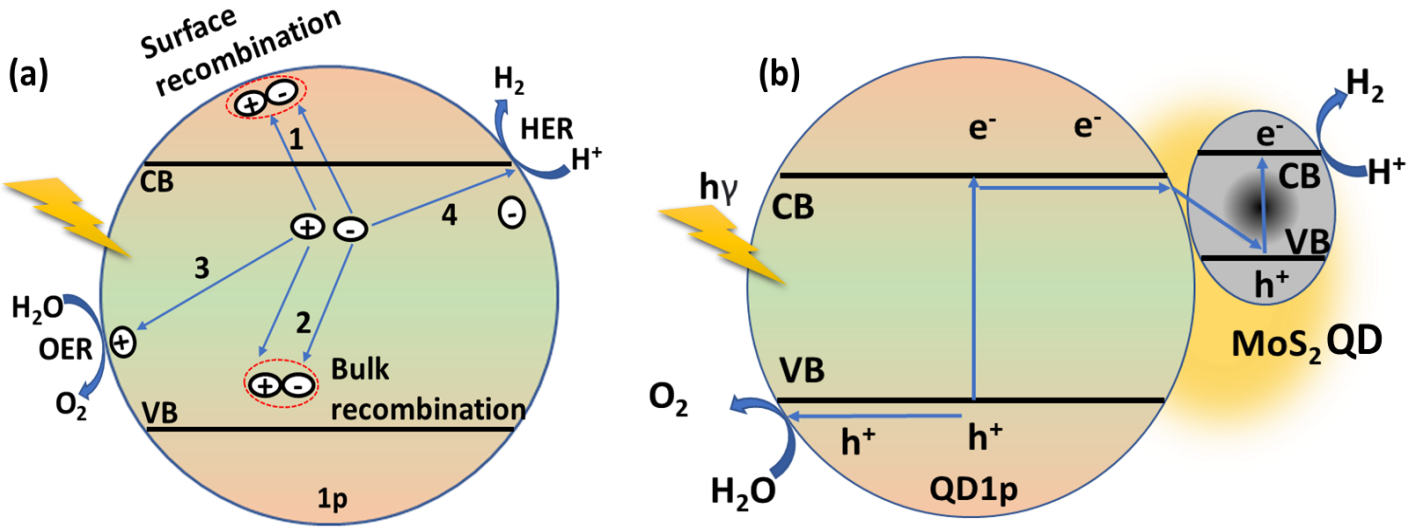

Figure 20 shows the 1p sample with various pathways of charge recombination (a) and the Z-scheme heterojunction formed between QD and 1p (b).

4. Conclusion:

The prepared Cobalt oxide and MoS_2QD photocatalyst using microwave irradiation have successfully demonstrated HER that outperformed the commercial source Sigma Aldrich Co_3O_4. PVA has been proven beneficial as a template to optimise the base 1p sample owing to its involvement in expediting the material synthesis process to a minimal of 2 minutes reaction time. The modification strategy with QD and the formed Z-Scheme heterojunction have outperformed the unmodified by 16.2 times (1.3 μmol $h^{-1}g^{-1}$) for 0.5QD1p and 22.5 times (1.8 μmol $h^{-1}g^{-1}$) for 1QD1p respectively. This enhancement is due to better light absorption, reduced band gap by 0.05 eV, enhanced electron and hole separation which is supported by the optical study (UV-Vis-NIR and PL) respectively. Along with lattice compression shown in XRD and electrochemical changes with increased concentration of reactive Co^{3+} species supported by XPS analysis. This study has generated empirical evidence of employing rapid microwave technique as a rapid and modern approach towards the synthesis of nanomaterials that can add newer finding in the field of material synthesis.

Credit authorship contribution statement

Upalee Labhane: Conceptualization; Data curation, Writing - original draft. **Zelio Fusco**: Characterization, data analysis. **Jia Ding**: Data analysis. **Yi-Chen Lin**: Characterization, data analysis, experimental design. **Hashim Jalil Khan**: Characterization, data analysis. **Sarina Sarina**: writing review and editing, **David Alam**: reaction design, writing review and editing. **Sergio Londono**: writing review and editing, **Alejandro Montoya**: writing review and editing, **David K. Wang**: supervision, writing review, editing, funding acquisition.

Declaration of Competing Interest

The authors declare no competing financial interest.

Acknowledgement.

The authors gratefully acknowledge the financial support given by the Australian Research Council (DP190101734) and Sydney Southeast Asia Centre Collaborative Research Grant. We also acknowledge the facilities from Sydney Analytical and Australian Centre for Microscopy and Microanalysis.

Supplementary information:

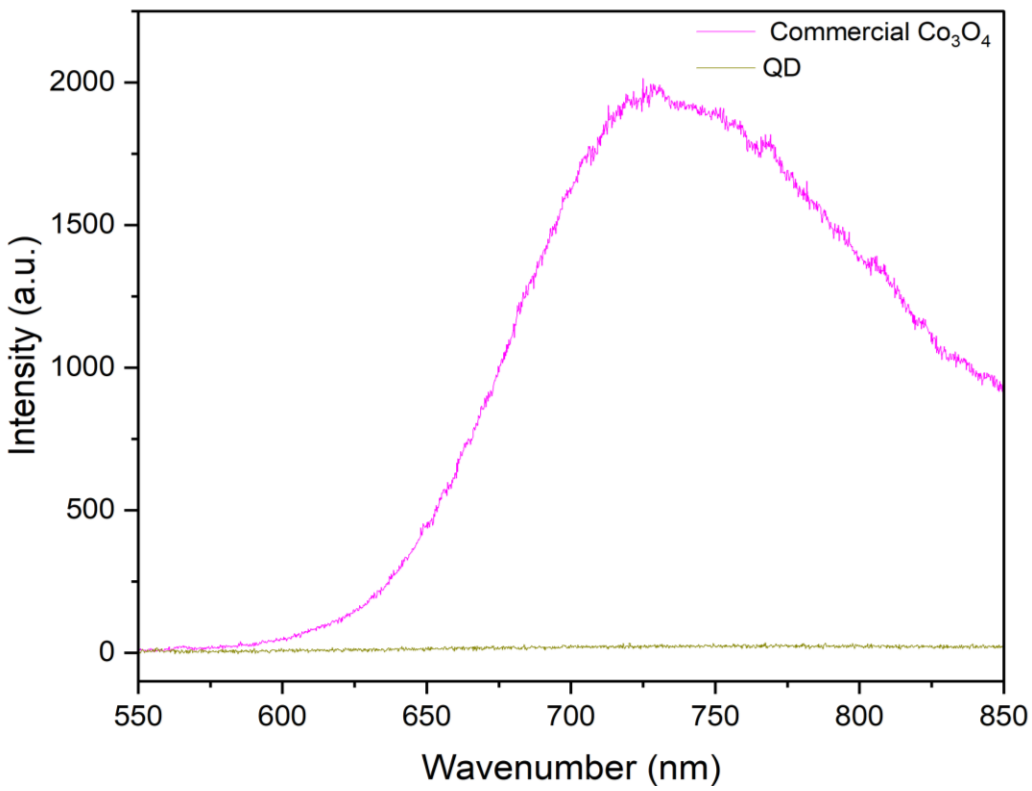

Figure 21 S1 PL for Commercial Co3O4

Photoluminescence: Pure QD does not demonstrate any peaks due to its excitation lying within the UV spectrum and the used PL laser source 550nm [216]. In contrast, commercial Co_3O_4 shows photoluminescence spectra, that demonstrates the highest charge recombination. Commercial Co_3O_4 has a comparative narrow peak maxima around 700 nm range, with high PL intensity compared to 1p sample.

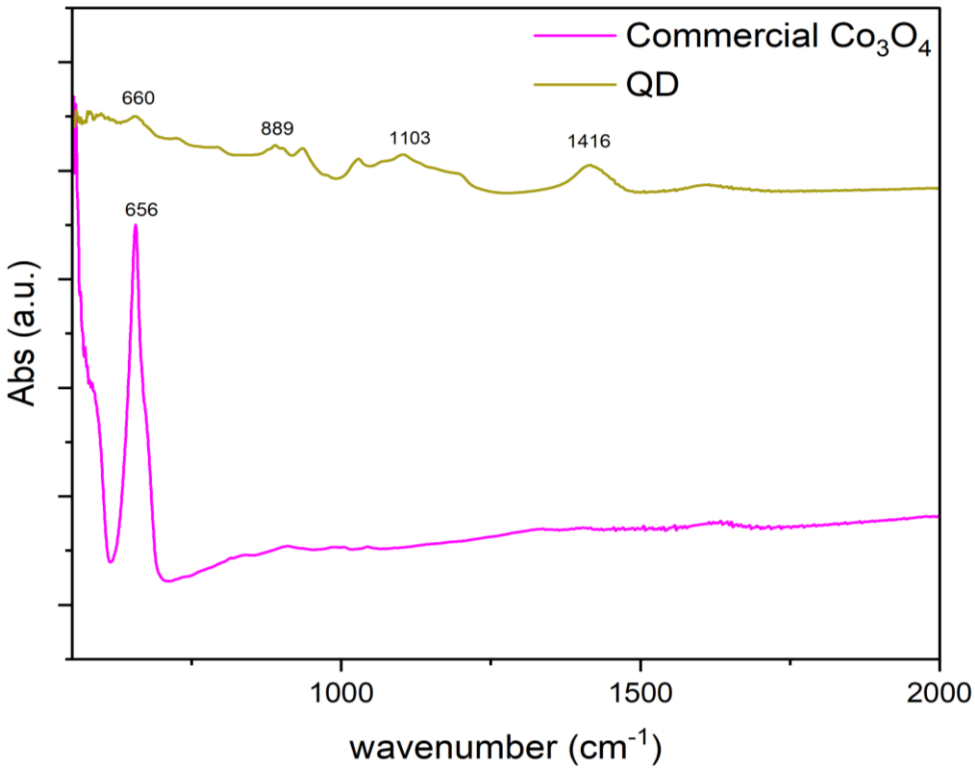

Figure 22 S2 FTIR Commercial Co3O4 and MoS2 QD

Microwave prepared MoS_2 has a characteristic peak at 660 nm, 889 nm, 1121 nm, 1416 nm and commercial Co_3O_4 656 nm and 739 nm as characteristic cobalt peaks.

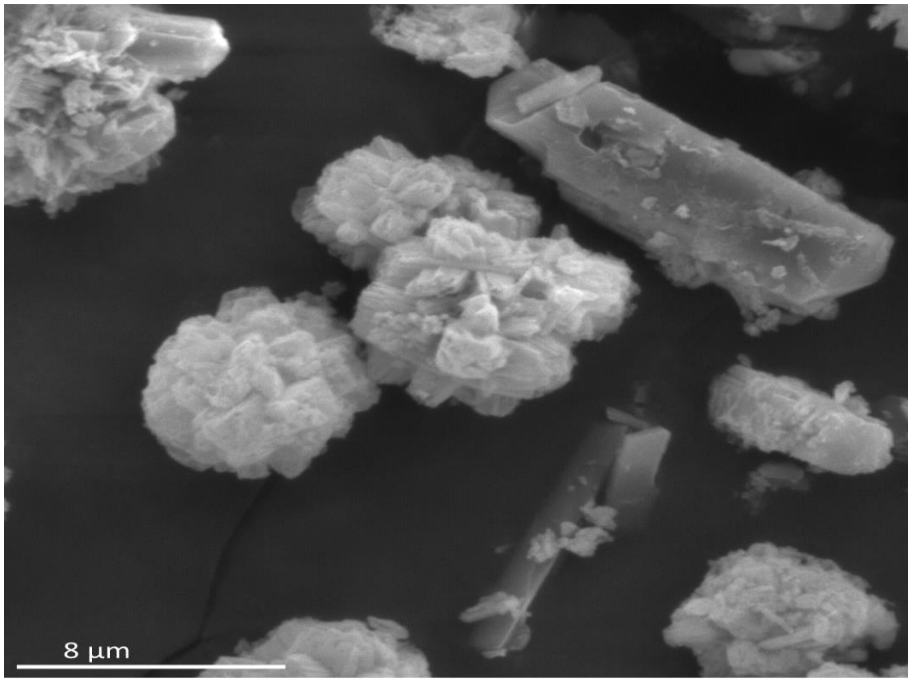

Figure 23 S3 SEM image showing rods and spheres.

SEM image (Figure 23 S3) shows the presence of rod shaped cobalt oxide and sphere like agglomerated oxalates that consists of irregular shaped nanomaterials attached to each other at rare ends and thus forming a sphere-shaped overall structure. this assumption is based on the fact that the irregularity in the physical structure is attributed in amorphous nature and the rods are more closely defined, confirming the crystallinity [217]. SEM observation is supported by XRD, where we confirmed the as synthesized cobalt comprises of oxide and oxalates.

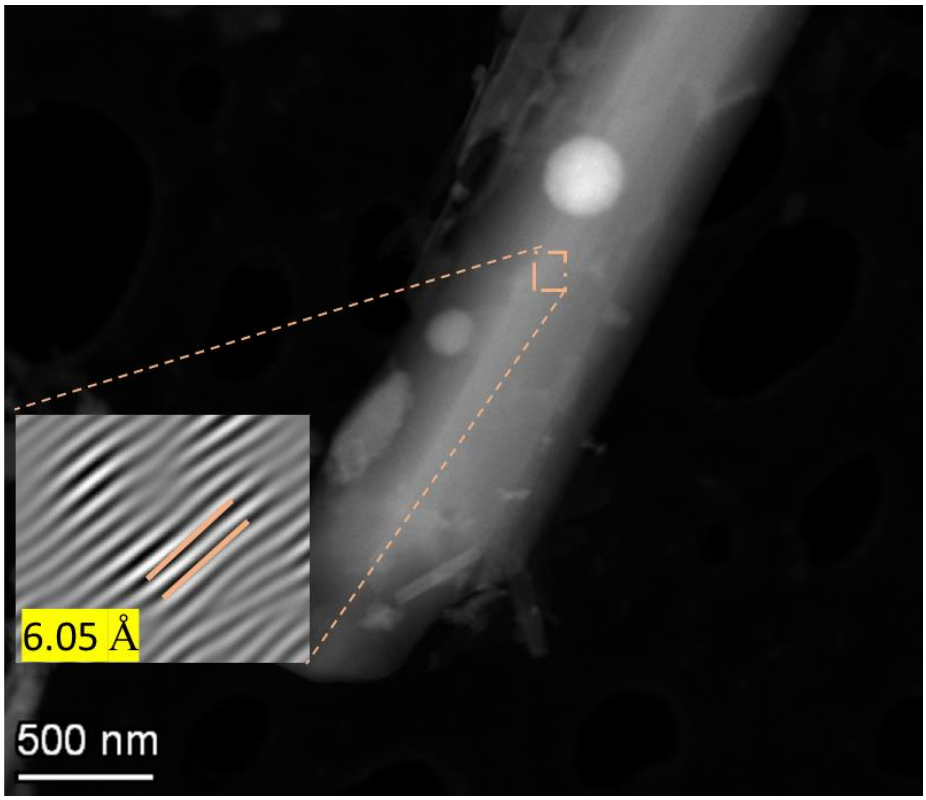

Figure 24 S4 lattice spacing of the modified 1QD 1p as it experiences the lattice change after introducing QD that is evident in the brighter spot attached over the rod.

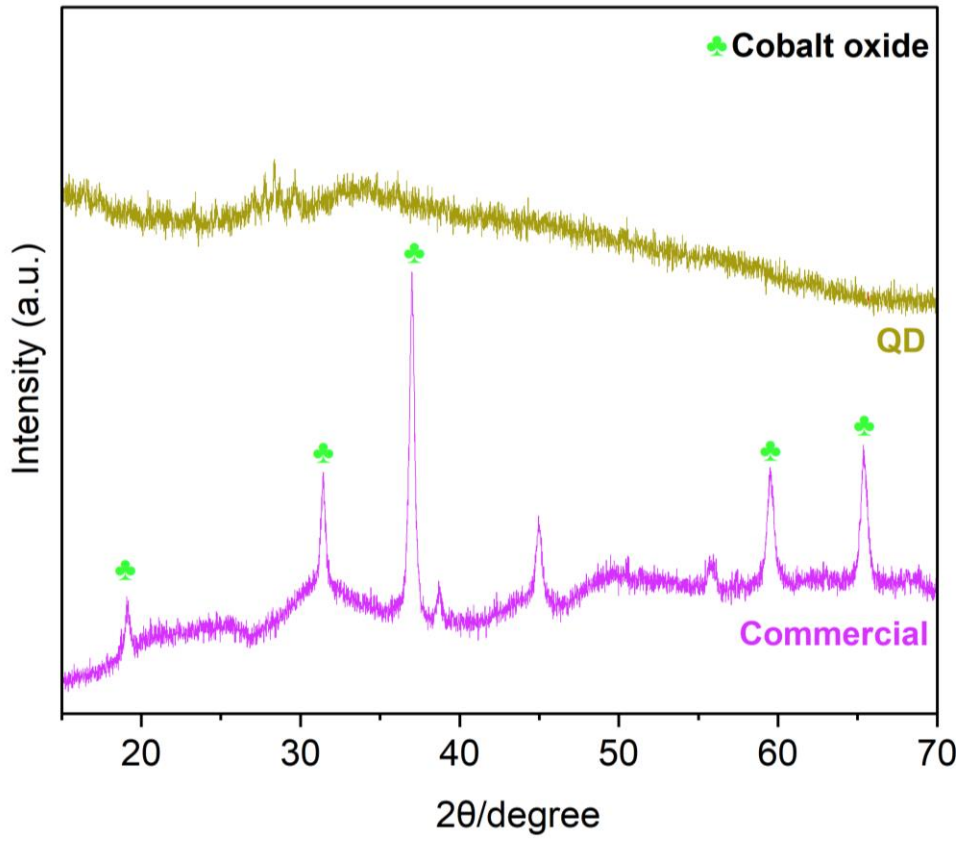

Figure 25 S5. XRD pattern for Commercial Co3O4 and pure QD.

Figure 25 S5 shows Commercially sourced Sigma Adrich, Co_3O_4 shows peaks at 2θ =19.1° 2θ, 31.24° 2θ, 36.9° 2θ, 59.5° 2θ, 65.4° 2θ these peaks correspond to crystallographic planes (111), (220), (311), (511), (440) that confirms the spinal Co_3O_4 cubic structure [218-220].

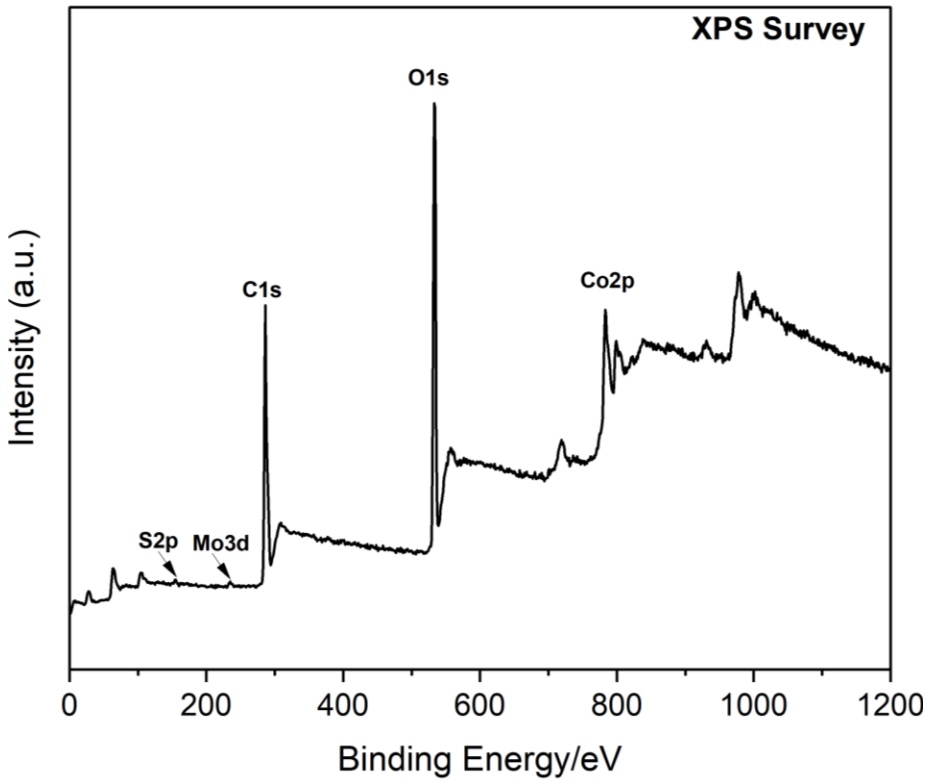

Figure 26 S6 XPS survey for 1QD1p sample.

The survey spectra in the Figure S6 shows the presence of Co2p, O1s, C1s, Mo3d, S2p. Also, the Carbon C1s reference peak was found to be at 284.8 eV for C-C bond and C-O-C at 286 eV.

Chapter 4. Microwave synthesised cobalt oxide and sigma Adrich sourced mmolybdenum disulfide bulk with two sets of sacrificial agents.

These sections have been submitted to the journal (Applied catalysis B: Environment and is under review. The corresponding data is attached in the appendix section contributing to the methodology, experimentation results and discussion on microwave synthesised cobalt oxide and molybdenum disulfide bulk with two sacrificial agents 1. 9:1 (v/v) water/TEOA and 2. Mixture of 1.25 M Na_2S + 1.75 M Na_2SO_3. These manuscripts highlight the need of using SA in order to scale up the hydrogen generation to commercialize the water splitting. Also, supports the finding that both, MoS_2Bulk and MoS_2QD can be used for HER.

Boosting Hydrogen Generation with Microwaved MoS2-Cobalt Oxide: Effect of sacrificial agents.

Upalee Labhane [a], Zelio Fusco [b], David Alam [a], Yi-Chen Lin [a], Hashim Jalil Khan [a], Jia Ding [a], Sarina Sarina [a], Sergio Londono [a], Alejandro Montoya [a], David K. Wang [a2]

[a] School of Chemical and Biomolecular Engineering. The University of Sydney, New South Wales, 2006, Australia
[b] College of Engineering, Computing and Cybernetics, Australian National University, Canberra, ACT, 2601, Australia.

[2] Corresponding author: David.wang1@sydney.edu.au

Abstract

The hydrogen evolution reaction (HER) performance of molybdenum disulfide (MoS_2) incorporated cobalt oxide photocatalysts has been successfully synthesized using rapid thermal microwave irradiation process. This study focuses on studying the effect of MoS_2 and sacrificial agents using triethanolamine (TEOA), sodium sulfide (Na_2S), and sodium sulfite (Na_2SO_3). Increasing MoS_2 concentration from 0, 0.5 to 1.5 wt%, the HER performance of the doped 1.5 $MoS_2Co_xO_y$ and undoped Co_xO_y were 11.21 and 0.30 $mmolg^{-1}h^{-1}$ respectively, while the commercial Co_3O_4 photocatalyst was 0.03 $mmolg^{-1}h^{-1}$ in TEOA. Similarly, the HER rate of the photocatalyst under Na_2S and Na_2SO_3 as a sacrificial agent was 16.64 $mmolg^{-1}h^{-1}$ for the 1.5 $MoS_2Co_xO_y$, while for the undoped Co_xO_y (0.32 $mmolg^{-1}h^{-1}$) and the commercial Co_3O_4 (0.22 $mmolg^{-1}h^{-1}$), respectively. The increment is 37 and 52 times respectively. The significant improvement of the HER performance was attributed to the changes in chemical and optical properties of the MoS_2 modified Co_xO_y samples.

Keywords: Photocatalyst; Water splitting; Cobalt oxides; Molybdenum disulfide (MoS2); Sacrificial agents.

1. Introduction.

Hydrogen is an ideal energy source due to its high combustion potential and minimal pollution generation [152, 221]. It has a wide range of industrial applications, serving as a vital energy source for vehicle fuel cells and fulfilling critical roles in industrial processes such as ammonia synthesis, CO_2 hydrogenation, methanol production, electronics, and the semiconductor industry. Various methods for hydrogen production have been explored, including electrolysis, thermo-catalysis, and photocatalysis [222]. Among these, photocatalytic hydrogen evolution reaction by water splitting

has become one of the most favourable pathways for achieving greener and more sustainable hydrogen production [1, 4].

In a typical water-splitting reaction, a semiconductor is excited by photon absorption, generating electrons and holes within the material. These charges are transferred to the surface of the semiconductor in contact with water molecules. The photocatalyst must overcome the redox potential as free energy change of water splitting, also known as the band gap energy (1.23 eV) [223]. This is the minimum amount of energy required for a water molecule to split into hydrogen (hydrogen evolution reaction, HER) and oxygen gas (oxygen evolution reaction, OER) shown in Figure 1 [224].

Cobalt oxide has been used for oxygen evolution reactions (OER) as a standalone, but many researchers have incorporated with Ni, Pt, Fe, and TiO_2 to achieve HER or OER [225]. Owing to its smaller bandgap, cobalt oxide can absorb light in the UV region (200 – 400 nm) similar to TiO_2, but can additionally absorb light in the visible wavelength range (400 – 700 nm)[226]. It has a more stable structure which can show long lasting hydrogen evolution [227]. Moreover, it possesses two main oxidation states (Co^{2+} and Co^{3+}) which can form several morphological phases into Co_3O_4, Co_2O_3, CoO, CoO_2 and cobalt oxalate , which can be used in water-splitting reactions [228]. Each phase can be tuned as an optimal heterojunction (modification) to achieve a desired band gap semiconductor, capable of harvesting visible light and maintaining the charge separation for higher water splitting [229]. However, the performance is limited by recombining electrons and holes in the bulk material and the surface that is one of the limiting characteristic also demonstrated in Figure 27 [230].

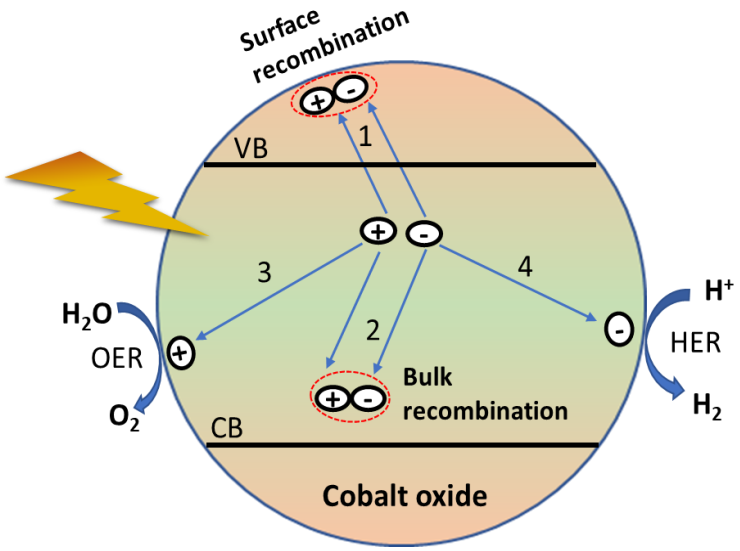

Figure 27 Electron-hole generation and potential pathways via photocatalysis in cobalt oxide nanomaterial.

Another main challenge of cobalt oxide photocatalyst is limited light absorption and active sites for the generated charge to interact with a water molecule to split [231]. These limitations can be overcome by doping cobalt oxide with a co-catalyst (N-type semiconductor) where cobalt oxide performs as an electron donor (P-type) [232, 233]. For example, noble metals such as Platinum, Iridium, gold, silver [85] or non-noble metals including Aluminium, Zinc, Nikel, Iron, Tin, and Molybdenum [85, 233] have been successfully dopped with cobalt oxide photocatalysts previously. Most notably Pt_3Co/CdS has a hydrogen yield of 45.09 $mmolh^{-1}g^{-1}$ after modification with dealloyed Pt_3Co that resulted in the addition of active sites and sufficient separation of electrons and holes [115]. Production rates of 20.65 $mmolh^{-1}g^{-1}$ was reported for Co-2TPABTz/Ag-NP due to the surface plasmonic resonance of the silver nanoparticles [98].

Recent studies have shown that Molybdenum disulfide (MoS_2) can be an alternative to noble metals for efficient solar-to-hydrogen conversion, offering scalability and sustainability for practical applications [190]. MoS_2 is a two-dimensional layered metal chalcogenide possessing a direct band gap. Its beneficial properties such as high edge site owing to the layered structure whereby the sulfur atoms have a strong affinity towards the hydrogen atoms and high surface area making it optimal for HER [190]. Similarly to cobalt oxides, MoS_2 has two oxidation states involving Mo (III) and Mo (IV) that enables charge transfer from Mo^{4+} to Mo^{3+} for HER [234].

The use of MoS_2 with Co_xO_y photocatalyst in aqueous solution for light-induced photocatalysis alone is insufficient for practical and commercial applications. Another important parameter in the water splitting reaction is the presence of a sacrificial agent, which provides electrons and holes to the photocatalyst and thus improves the performance. They also limit the side reaction and control the electron-hole recombination (Figure 27, pathways 1 and 2) [235]. Sacrificial agents can be categorized as electron donors or electron acceptors to generate hydrogen or oxygen gases as they undergo oxidation or reduction in the water splitting reaction and promote the energy uphill reaction ΔH_0 = 286 kJ mol^{-1} [236]. A few examples are sodium oxalates, potassium persulfate, silver nitrate, and methanol, ethanol, lactic acid, triethanolamine (TEOA), sodium sulfide (Na_2S), and sodium sulfite (Na_2SO_3) [237].

This work investigates cobalt-based photocatalysts synthesised by microwave irradiation and modified with MoS2 in concentrations ranging from 0.5 to 1.5 wt% for aqueous-based hydrogen evolution reaction. The effect of TEOA, Na_2S, and Na_2SO_3 as sacrificial agents on hydrogen generation from water-splitting reactions is elucidated.

2. Materials and Methodology

2.1 Materials

Unless specified otherwise, all chemicals were purchased and used as received from Sigma Aldrich. Molybdenum disulfide (reagent grade ≥98.0%), Cobalt oxide (99.5% trace metal basis) <50 nm particle size, Cobalt nitrate hexahydrate (ACS reagent, ≥ 98%), potassium oxalate monohydrate (ACS reagent, 99%), poly (vinyl alcohol) (99+% hydrolysed), sodium hydroxide (reagent grade, ≥98%), Ammonium tetra-thiomolybdate (99.97% trace metals basis), Hydrazine hydrate (reagent grade, N_2H_4 50-60 %), and Ethanol (ACS reagent, ≥99.5%), Triethanolamine (purity≥99.0%), Sodium sulfide (Na_2S) and Sodium sulfite (Na_2SO_3) (ACS reagent, ≥98.0%) were used.

2.2 Synthesis of pure cobalt oxide photocatalyst

Individual stock solutions for both cobalt nitrate hexahydrate and potassium oxalate were made in 100 mL with a concentration of 0.2M, respectively. Stoichiometric equivalent of each were combined (30 mL) and $K_2C_2O_4$ solution was added later dropwise. This solution was stirred for 15 minutes and then 90 mL suspension of PVA (0.5, 1.0, 1.5 and 2.0 wt.%) was added slowly along with the stirring (varying grams of PVA powder was added to 100 mL of DI water and stirred for 24 hours) [174]. This suspension was stirred for 15 minutes again, and 400 uL of 1M NaOH was added. This was then transferred to a sample vial for MW irradiation (Microwave Digestor, Ethos One from Milestone). Microwave synthesis of pure cobalt oxide photocatalyst was carried out at 900 W, 200 °C for 2 minutes. The resulting cobalt nanopartitcle suspension was centrifuged at 10,000 rpm for 10 minutes and washed with diethyl ether three times. The sample was then dried in an oven at 60 °C overnight, and grinded into a powder by mortar and pestle for 5 minutes to get a fine power

2.3. Synthesis of $MoS_2Co_xO_y$ heterojunction photocatalyst

Microwave prepared cobalt oxide photocatalyst was weighed and was added to 100 ml ethanol. A amount of MoS_2 in 0.5, 1.0, 1.5 wt.% was added. This suspension was stirred for 24 hours at 500 rpm at 25 °C, transferred to a centrifuge tube and centrifuged for 5 mins at 10,000 rpm and the $MoS_2Co_xO_y$ was then collected and dried overnight at 60 °C.

2.4. Hydrogen evolution reaction

In the hydrogen evolution experiment setup, a 300 W Xenon bulk lamp with a λ <420 nm filter was used as a light source from Aulight, China. The experiments occurred in a 200 mL stainless steel reactor fitted with a quartz glass window at the top for light penetration and this reactor was maintained at 0.9 bar and 25°C. A glass container was charged with the sacrificial agent solution one at each time. 1. DI water to TEOA 9:1 (v/v) and 2. Stoichiometric equivalent of 1.25M (Na_2S) + 1.75M (Na_2SO_3) [99, 238]. Subsequently, 20 mg of photocatalyst was added to this 40 mL volume of sacrificial agent solution. A PerkinElmer Gas Chromatograph with a thermal conductivity detector (TCD, 5 Å molecular sieve column) was used for analysing the produced hydrogen gas. Before starting the experiments, the reactor system was put under vacuum for 15 minutes using a vacuum pump to degas any atmospheric gases from the reactor, followed by dark condition for 30 minutes. After turning on the light source (1525 LUX), at every 1-hour interval, the produced gas in the reactor was drawn off using a soil gas tight syringe and manually injected into the PerkinElmer Gas Chromatograph (Arnel 590) with TCD and argon as a carrier gas to detect the amount of hydrogen generated. The photocatalyst was recovered and used again with the same amount of sacrificial agent added into the aqueous solution for repeat cycling tests.

2.5 Photocatalyst characterization:

Powder X-ray diffraction (XRD) patterns were recorded by PANalytical X'Pert3 powder diffraction. The d -spacing was calculated using the Bragg's Law formula, $\lambda = 2d \sin \theta$, where λ is the wavelength (1.54 Å for Cu Kα) [172]. Thermo Fisher K-Alpha+ XPS/UPS was used for investigating the chemical composition of the photocatalyst. UV-Vis-NIR Spectrophotometer UV-3600 with triple detectors from Shimadzu was used for light absorbance spectroscopy. CHI electrochemical workstation (532 nm laser) apparatus with 3 electrode system and a 0.5 M Na_2SO_4 electrolyte and a Ag/AgCl electrolyte was used for Photoluminescence. Nicolet iS20 FTIR Spectrometer from ThermoFisher was used for FTIR analysis that confirmed the functional groups present in the samples.

3. Results and Discussion.

Figure 28 shows x-ray diffraction (XRD) and x-ray photo-electron spectroscopy (XPS) patterns for the as-synthesised cobalt oxide catalyst and its Mo, S modified counterpart. The presence of two cobalt oxide phases (Cobalt tetraoxide (Co_3O_4) and Cobalt oxalate (CoC_2O_4)) are confirmed.

3.1 X-Ray diffraction analysis (XRD).

In the unmodified Co_xO_y sample, two major cobalt phases were identified. Firstly, the peaks for 19.1° (111), and 33.9° 2θ confirmed the monoclinic structure of Co_3O_4 catalyst (Figure 28) [183, 184]. In addition, another cobalt phase with peaks at 18.7° , 30.3° , 35.0° 2θ confirmed the presence of cobalt oxalate with orthorhombic structure [239, 240]. As for the modified 1.5 $MoS_2Co_xO_y$ sample, the two adjacent cobalt oxalates (18.7° and 19.1° 2θ) were merged into a single broad peak at 18.7° 2θ [241]. This change is attributed to the crystal lattice expansion as MoS_2 has larger particle size than the cobalt oxalate in the MoS_2 Co_xO_y sample [241]. From the d-spacing estimation, the lattice spacing changed from 7.63 Å (unmodified) to 9.91 Å (1.5 $MoS_2Co_xO_y$) (Figure 32) and agrees well with the literature (oxalates have a d-spacing of > 7 Å) [172]. This

peak shift due to the lattice spacing change in the modified photocatalyst has been suggested to capture a wider light spectrum [242]. XRD results suggested that the addition of MoS_2 has changed the lattice structure of cobalt oxalate and cobalt oxides, thus expanded lattice slits are exposed. Secondly, the inherently larger sized cobalt oxalate lattice is expanded, substituting the oxygen valences in oxides [241]. Another evidence of Co_xO_y morphological change after MoS_2 modification can be found at 29.8° 2θ which is shifted from 30.3° 2θ [243]. Thus, these results demonstrated that MoS_2 modification has altered the base photocatalyst. XRD spectra of 0.5, 1, 1.51.5 $MoS_2Co_xO_y$ sample is shown in Figure 32.

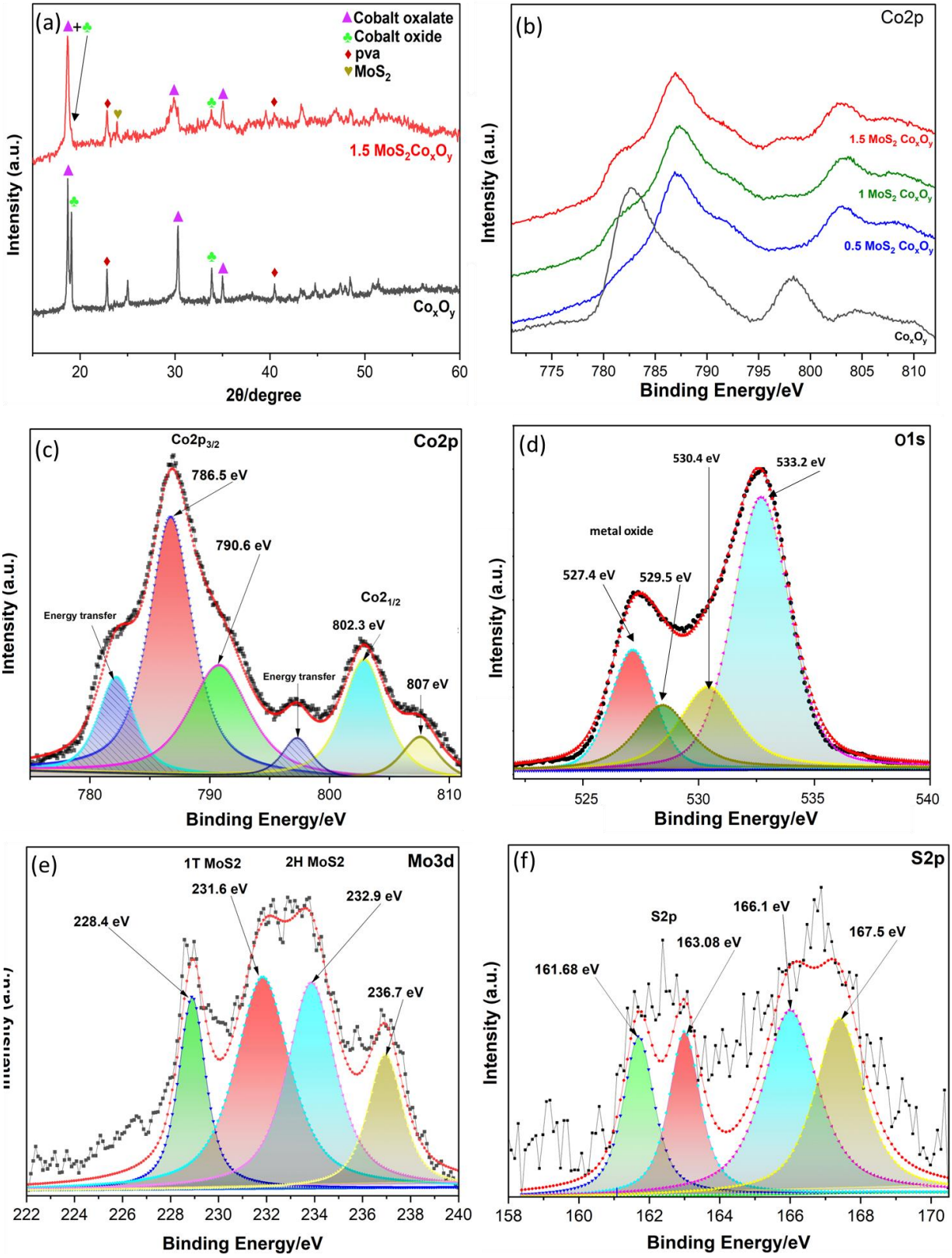
(a)
Cobalt oxalate
Cobalt oxide
pva
MoS2
1.5 MoS2CoxOy
CoxOy
Intensity (a.u.)
2θ/degree
(b)
Co2p
1.5 MoS2 CoxOy
1 MoS2 CoxOy
0.5 MoS2 CoxOy
CoxOy
Intensity (a.u.)
Binding Energy/eV
(c)
Co2p
Co2p3/2
786.5 eV
790.6 eV
Energy transfer
Energy transfer
Co21/2
802.3 eV
807 eV
Intensity (a.u.)
Binding Energy/eV
(d)
O1s
530.4 eV
533.2 eV
metal oxide
527.4 eV
529.5 eV
Intensity (a.u.)
Binding Energy/eV
(e)
1T MoS2
2H MoS2
Mo3d
231.6 eV
232.9 eV
228.4 eV
236.7 eV
Binding Energy/eV
(f)
S2p
S2p
166.1 eV
163.08 eV
167.5 eV
161.68 eV
Intensity (a.u.)
Binding Energy/eV

Figure 28 Chemical Properties of As-synthesized 1.5 MoS2CoxOy Catalyst, XRD for CoxOy and 1.5 MoS2CoxOy with symbols to identify constituting peak (a), Co2p region (b), deconvolute Co2p (c), deconvolute O1s (d), deconvolute Mo3d (e), deconvolute S1p (f).

3.2 X-ray photoelectron spectroscopy (XPS).

The XPS survey was conducted for chemical identification for the photocatalysts. In the XPS survey (Figure 36) Co2p, O1s, C1s, Mo3d, and S1p elements were detected, and the Carbon C1s reference peak was standardised to 284.7 eV for C-C bond and C-O at 286.4 eV. The major peak difference for 1.5 $MoS_2Co_xO_y$ was the appearance of the energy transfer peak for both regions ($Co2p_{3/2}$ and $2p_{1/2}$) along with a 4.3 eV red shift is an indicative of alteration of cobalt oxidation states and chemical bonding with the modifier atom [192]. Also, the redshift in the Co2p towards the higher energy demonstrates an increment in the electronic density after modification and an opposite trend, a blue shift (electron deficient) in the O1s indicative of the charge transfer phenomenon. Hence, considering the interfacial electric field, the electrons generated in the Cobalt oxide (conduction band) are transfer to the MoS_2QD (valence band) resulting in Z-scheme formation (Supporting data Figure S6) [244].

Figure 28 (c) shows the region between 773 to 791 eV is for the binding energy of $Co2p_{3/2}$ and 791 to 820 eV for the binding energy of $Co2p_{1/2}$. In this region, two Co valence states identified as Co(III) and Co(II) were attributed to both cobalt oxide and oxalate. The peak at 786.5 eV is indexed to Co^{2+} of $2p_{3/2}$ and 790.6 eV is for Co^{3+} of $2p_{3/2}$ [221, 245]. The latter peak is the region's binding energies due to the blue shift stretching after doping. The other major peak at 802.3 eV is associated to $Co^{2+}2p_{1/2}$ and the peak at 807 eV is assigned to $Co^{3+}2p_{1/2}$ [246, 247]. The area under

Co^{2+}:Co^{3+} in Co_xO_y was measured to be 4:1 which decreased to 2:1 for the 1.5 $MoS_2Co_xO_y$ suggesting that there is a proportionally higher concentration of Co^{3+} [248]. After deconvoluting O1s in figure 2d, two maxima are observed. The peaks located at 527.4 eV corresponds to the pre-edge peak that is the result of internal charge transfer from cobalt to oxygen and 529.5 eV is attributed to the cobalt metal oxides [249, 250]. However, the larger signals at 530.4 eV is of the oxyhydroxides that are regarded as active sites for HER and 533.2 eV is identified as absorbed water peaks [251].

Figure 28 (e) shows that Mo3d spectrum peaks are located at 228.4 (Mo^{4+} $3d_{5/2}$) and 231.4 eV (Mo^{4+} $3d_{3/2}$) of Mo^{4+} is for 1T MoS_2 [252]. The other phase is 2H MoS_2 that is observed at 232.9 eV (Mo^{4+} $3d_{5/2}$) and 236.5 eV (Mo^{4+} $3d_{3/2}$), also these peaks can overlap with the corresponding to Mo^{+6} that are associated to Mo-O bonding [253] with Co_xO_y. For S2p (Figure 2f), after deconvoluting, 161.68 eV ($S2p_{3/2}$) and 163.08 eV ($S2p_{1/2}$) supports the presence of S atom in MoS_2 [254]. Additionally, the peaks present at 166.1 eV and 167.5 eV are caused by the formation of bonded sulfonic group and oxygen group [255, 256] which agrees with the deconvoluted peaks in the O1s region.

3.3 Fourier transform infrared reflectance (FTIR).

FTIR spectrum of the functional group after doping with MoS_2 is shown in Figure 33. Both Co_xO_y and 1.5 $MoS_2Co_xO_y$ show similar FTIR characteristic peaks due to their similar chemical functionality. The cobalt-oxygen characteristic peaks are observed at 824 $cm^{-1,}$ indicative of abridging oxalate group and 737 cm^{-1} are assigned to Co-O in which Co is in the form of $Co^{2+}$and 570 cm^{-1} as Co^{3+} are attributed to cobalt oxide and oxalate groups which are also seen in the 1.5 $MoS_2Co_xO_y$ sample [185, 209]. However, all the peaks intensities and positions in Co_xO_y

increased with a red shift after modification which has been attributed to enhanced lattice slits exposure due to the ethanol use in the modification process of the 1.5 $MoS_2Co_xO_y$ photocatalyst [210]. Notably, the absence of 1375 cm^{-1} peak adjacent to 1356 cm^{-1} in 1.5 $MoS_2Co_xO_y$ indicates Co-O-H dissociation and OH deformation [211, 257].

3.4 UV-Vis NIR.

Figure 29 (a) shows the absorbance of unmodified and modified samples from 200 nm (UV) range to 1600 nm (near infrared spectrum) that covers two regions of light UV-Vis-NIR. The increase of MoS_2 dopant concentration, an increment was seen in overall absorbance intensity, particularly in the range from 400 to 1000 nm in the visible light range as compared with the unmodified Co_xO_y. This increase in the visible light absorption in the modified photocatalyst can be ascribed to O^{2-} to Co^{3+} charge transfer [258]. Characteristically, the region near 330 nm relates to the band gap transition of cobalt oxide from valence band to conduction band [259]. As shown in the inset of Figure 29, Tauc plots was used to calculate the band gap of the photocatalysts where n=2. The band gap of Co_xO_y decrease from 3.41 eV to 3.35 eV after MoS_2 modification. This is due to the charge transfer from O^{2-} to Co^{3+} because of MoS_2 cobalt oxide structure formation, which again agrees with the overall enhanced light absorption finding [260].

3.5 Photoluminescence (PL).

Photoluminescence technique crucially characterize the electron-hole separation behavior for the photocatalysts. The pure MoS_2 PL intensity is shown in Figure 35. From Figure 29 (b), it can be clearly observed that the unmodified Co_xO_y photocatalyst possesses significantly high peak intensity in the range 630 to 750 nm. This peak range is related to the direct band gap transition region, this result shows that the electrons and holes of Co_xO_y sample are recombining at a rapid

rate and resulting in reduced possibility of reaction with water molecule for HER. This behaviour suggests that the Co_xO_y attains the excitation state, but due to the short life spans of these excitons, the electrons rapidly transition back to the ground state. In contrast, all the modified samples have shown a significant reduction in the PL intensity along with a slight blue shift. Due to the surface effect by MoS_2 which emits the photons with higher energy levels, the electrons are excited for longer times. Thus, emittance energy difference forming a direct proportionality with enhance photocatalytic performance for the modified samples. This ability of the photocatalyst to retain the excitation state is critical and is evident in PL spectrum. The PL intensity increased in the order of 1.5 $MoS_2Co_xO_y$ < 1 $MoS_2Co_xO_y$ < 0.5 $MoS_2Co_xO_y$ < Co_xO_y.

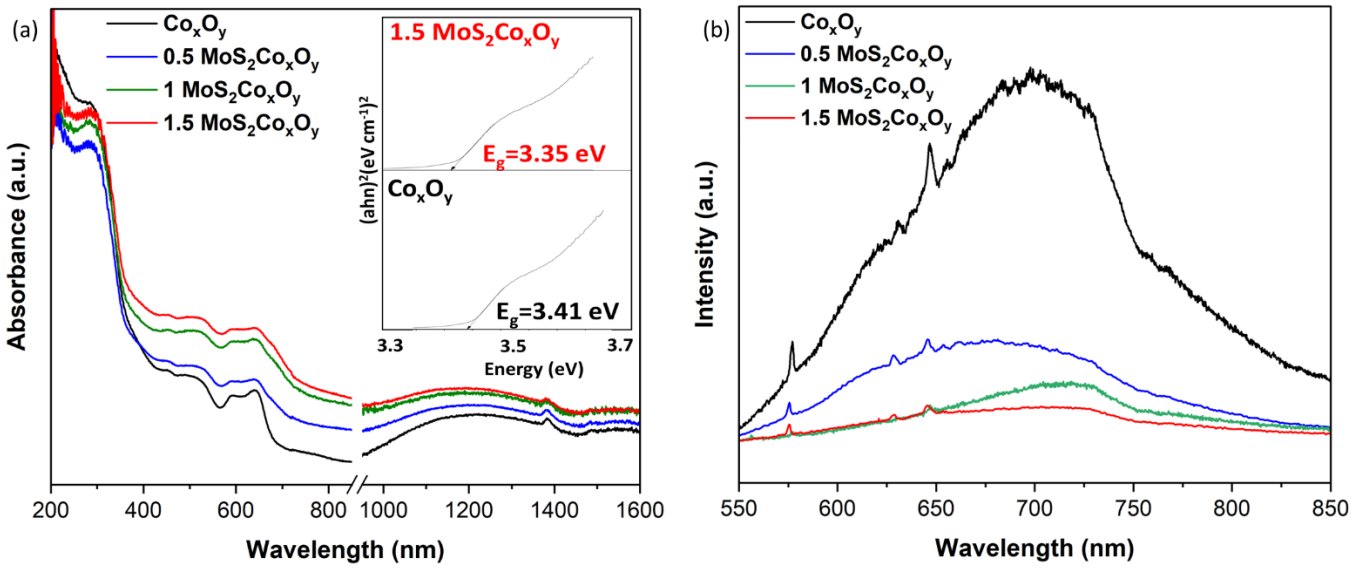

Figure 29 Optical study. UV Vis NIR spectra of CoxOy and MoS2 modified CoxOy. Inset images show Tauc plots for CoxOy and 1.5 MoS2CoxOy.alongwith bank gap energy estimation (a), Photoluminescence for CoxOy and modified MoS2CoxOy samples (b).

3.6 Hydrogen evolution reaction (HER) performance

In our study we investigated two sets of sacrificial agents (TEOA and mixture of Na_2S + Na_2SO_3) to test the photocatalytic performance along with the MoS_2 modified cobalt oxide photocatalyst. Figure 30 (a) and (b) show the photocatalysts' hydrogen concentration and the HER rate in the TEOA system, respectively. Firstly, the hydrogen concentration for the unmodified photocatalysts (Co_xO_y and the commercial Co_3O_4 and MoS_2) show very little increase over time (Figure 4a). This result translated into the lowest HER rate of 0.03 $mmolg^{-1}h^{-1}$ for the commercial Co_3O_4. Similarly, the pure MoS_2 had a relatively low HER rate of only 0.12 $mmolg^{-1}h^{-1}$, which was four times greater than the commercial Co_3O_4. Compared to all the stand-alone pure photocatalysts, the microwave synthesized Co_xO_y achieved a better HER rate with 0.30 $mmolg^{-1}h^{-1}$. In comparison, the MoS_2 modified photocatalysts showed a significant enhancement in the hydrogen production. For $MoS_2Co_xO_y$, the HER rate was 1.86 $mmolg^{-1}h^{-1}$ (0.5 $MoS_2Co_xO_y$), 3.16 $mmolg^{-1}h^{-1}$ (1 $MoS_2Co_xO_y$), and 11.21 $mmolg^{-1}h^{-1}$ (1.5 $MoS_2Co_xO_y$). This equates to one to two magnitude increase compared to the unmodified Co_xO_y, and the commercial sample.

Comparatively, the effect of sodium sulfide/sulfite sacrificial agent for HER and the results are displayed in Figure 30 (c) and (d). In our study, this mixture performed better than the TEOA series. Firstly, the commercial Co_3O_4 achieved a production rate of 0.22 $mmolg^{-1}h^{-1}$, followed by the commercial pure MoS_2 (0.31 $mmolg^{-1}h^{-1}$), and the microwave synthesized Co_xO_y (0.32 $mmolg^{-1}h^{-1}$). Similar trends in activity were observed with that of TEOA, 0.5 $MoS_2Co_xO_y$ photocatalyst showed hydrogen production rate of 4.79 $mmolg^{-1}h^{-1}$, 1 $MoS_2Co_xO_y$ with a value of 10.22 $mmolg^{-1}h^{-1}$ and finally, the highest performance was recorded at 16.64 $mmolg^{-1}h^{-1}$ for 1.5 $MoS_2Co_xO_y$. Compared to Co_xO_y, the enhancements equate to 15, 37 and 52 times increases in HER, respectively.

The cyclic study was performed for both TEOA and Na_2S + Na_2SO_3 sacrificial agent systems (Figure 30 (e) and Figure 30 (f)). Both systems showed relatively good cyclic stability as there is high reproducibility of hydrogen production in cycles 2 and 3. TEOA showed a lesser overall loss of hydrogen production (1.5 $mmolg^{-1}h^{-1}$) compared to that of the Na_2S + Na_2SO_3 system (2.3 $mmolg^{-1}h^{-1}$). An explanation for this decrease could be the intermediate complexes' blockage of the active sites [261]. Photo-corrosion is another possible reason of the reduced performance as the presence of sulfides and sulfites has been found to cause photo-corrosion of the cobalt oxides catalyst [262, 263]. On the other hand the uncertainty, and reproducibility in the error bars is due to the manual errors while sucking the hydrogen gas produced in the reactor and also to the amount of detected gas via the manual inject port of the GC equipment.

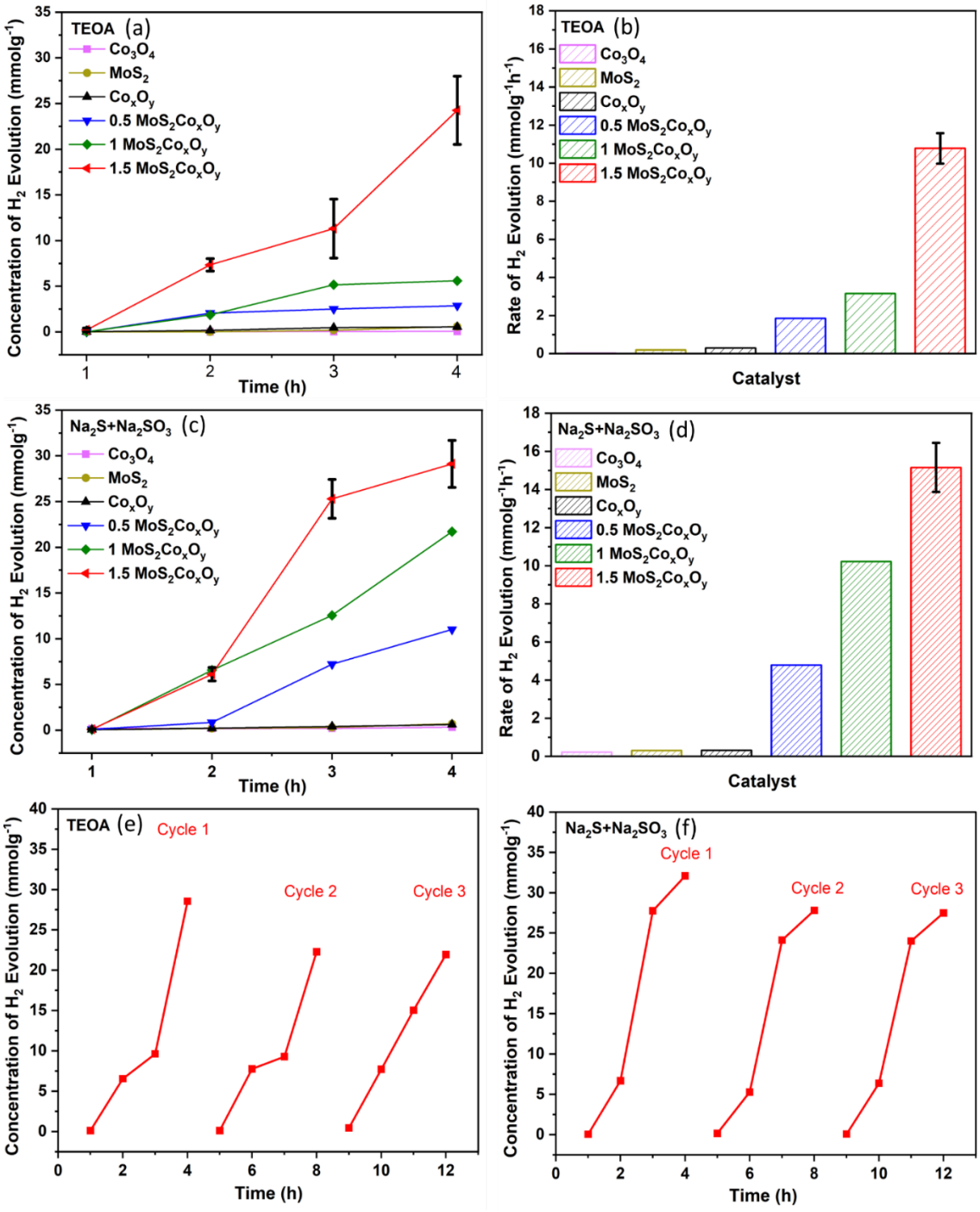

Figure 30 Photocatalytic hydrogen evolution reaction performance of photocatalysts (CoxOy and the commercial Co3O4 and MoS2) and MoS2 modified CoxOy showing hydrogen concentration (a, c) and rate of hydrogen production (b, d) for TEOA and Na2S+Na2SO3 along with cyclic test (e, f).

4. Mechanism for TEAO and $Na_2S + Na_2SO_3$ mixture.

In the Figure 31 (a), the proposed multistage mechanism for hydrogen generation shows electron movement upon excitation and oxidation. Upon light irradiation of the photocatalyst, the electron (e^-) in the ground state promoted to the excitation state (step 1) then the cobalt is oxidized by the excited electron from Co^{3+} to Co^{2+} (step 2). IN the absence of SA, a performance limiting step is possible at this stage where the electron can travel back to the valance band resulting in loss of change (Step 3). Alternatively, the photogenerated electron travels to TEOA (Step 4 start) and oxidizes TEOA by losing an electron Step 4 (end). It is oxidized TEOA to a TEOA$^\bullet$ radical releasing a H^+ radical (Step 5) and the dissociation of TEOA (cation) forming α-amino radical as an intermediate complex 1, releasing an electron at Step 6. Further (step 7), this strong reducing intermediate (α-amino radical) along with the water molecule forms asecondary amines and aldehydes irreversibly via hydrolysis by the end of step 8 [264, 265]. This results in the second H^+ proton (Step 6 and Step 8), which migrates to MoS_2 active site due to its inherent reduction potential and both protons are reduced to H_2 gas. These steps are described by the following Equations [265]

$C_6H_{15}NO_3 \rightarrow C_6H_{15}NO_3^+ + e^-$ Eq (1)

$C_6H_{15}NO_3^+ \rightarrow C_6H_{15}NO_3^\bullet + H^+$ … Step 5 Eq (2)

$C_6H_{15}NO_3^\bullet \rightarrow C_6H_{14}NO_3^+ + e^-$ … Step 6 Eq (3)

$C_6H_{14}NO_3^+ + H_2O$ … Step 70 Eq (4)

$C_6H_{14}NO_3^+ + H_2O \rightarrow C_6H_{11}NO_3 + CH_3CHO + H^+$… Step 8 Eq (5)

A similar multistage pathway is proposed for $Na_2S + Na_2SO_3$ system as shown in Figure 31 (b). However, the Equations for $Na_2S + Na_2SO_3$ system are shown below [265, 266]

$Na_2S + Na_2SO_3 \rightarrow S^{2-} + SO_3^{2-}$ … Step 4 Eq(1)

$S^{2-} + SO_3^{2-} + H_2O \rightarrow H^+ + S_2^{2-} + SO_4^{2-} / S_2O_6^{2-} + 2e^-$… Step 5 Eq(2)

$2H_2O + 2e^- \rightarrow H_2 + 2OH^-$… Step 6 Eq(3)

In the $Na_2S + Na_2SO_3$ system, the assumption is the oxidation state of the heterojunction is positive for the sulfur species to be oxidized thus forming the S species [267]. The first 3 step are same in this series of sacrificial agent. However, both $Na_2S + Na_2SO_3$ are oxidized to S^{2+} and SO_3^{2-} species in Step 4. In presence of H_2O these two S species are further oxidized as S_2^{2-} liberating H^+ proton and the reminder SO_3^{2-} can be oxidized into two schemes 1. SO_3^{2-} to SO_4^{2-} and 2. SO_3^{2-} to $S_2O_6^{2-}$ complex in Step 5. Then electron from this scheme can interact with water molecule $2H_2O + 2e^-$ (Step 6) and further reduce to $H_2 + 2OH^-$ (Step 7) at the MoS_2 site as shown in figure 5b.

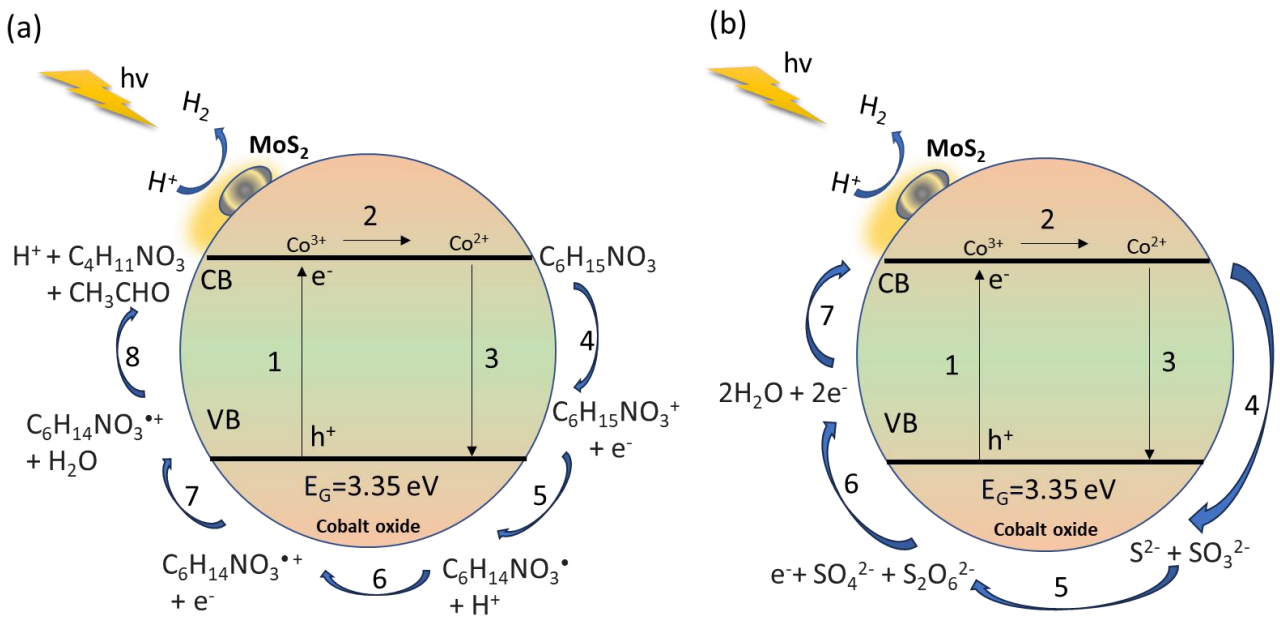

Figure 31 Proposed photocatalytic mechanism using modified MoS2CoxOy sample, TEOA (a) and Na2S + Na2SO3 (b).

Table 3 compares the hydrogen production rate of state-of-the-art cobalt based photocatalysts in the literature where cobalt was investigated as a base or co-catalyst in different sacrificial agents. At the outset, it should be noted that HER performance between studies is difficult to be directly compared due to the different dopant modifiers, sacrificial agents (SA), and their concentrations used in each of the report, as well as reaction conditions (light intensity, wavelength, temperature, pressure). Hence, Table 1 is compiled as a generalized benchmarking exercise between the literature best values and the results obtained in this study.

To date, the highest HER rates achieved by cobalt based photocatalysts reached 226.2 $mmolg^{-1}h^{-1}$ for Au-Co/TiO_2 (methanol) [93]. The enhanced performance for the above was due to electron-hole charge separation and ohmic contact generated between Au-Pd. Both studies use organic

sacrificial agents at 11% (v/v) of methanol. The optical concentration of TEOA is calculated by apparent quenching rate constant, this was studied by Ma B., at al (2019) [103] that the higher TEOA concentration showed a decrease in HER, this can be attributed to the promotion of side reactions and hinder the light absorption onto the photocatalyst surface. Also, comparing the dosage (mg/mL), our study lies within the comparable range with the literature. Comparing to the TEOA and sulfide/sulfite systems, the HER rates for a variety of heterojunction photocatalysts can be seen as high as 40.2 $mmolg^{-1}h^{-1}$ with (TEOA) for $Cu_{0.9}Co_{2.1}S_4@MoS_2$ [103], 45.1 $mmolg^{-1}h^{-1}$ with $(NH_4)_2SO_3$) for Pt_3Co/CdS [115] and 17.0 $mmolg^{-1}h^{-1}$ with ($Na_2S+Na_2SO_3$) for $NiCo_2O_4/Mn_{0.05}Cd_{0.95}S$ [111]. It is important to note that, despite the high HER rates reported in the previous studies, the complex chemistry, and chemical compositions of these photocatalysts typically involve noble metals, quantum dots and 1D/2D layered nanomaterials such as graphene oxides and double hydroxides. In contrast, our study on MoS_2 and microwave synthesized Co_xO_y Z-scheme heterojunction produced competitive HER rate of 16.6 $mmolg^{-1}h^{-1}$ compared to 3.8 $mmolg^{-1}h^{-1}$ for the MoS_2/Co_3O_4 S-scheme heterojunction [114], and 16.5 $mmolg^{-1}h^{-1}$ for the $Mn_{0.2}Cd_{0.8}S/MoS_2/Co_3O_4$ p-n type heterojunction [110] under similar SA system and conditions.

Table 3 Comparison of cobalt-based catalysts' hydrogen production rate with co-catalyst and modifier under different sacrificial agent systems.

Cobalt-based Photocatalyst	**Catalyst (mg)**	**[Dosage] (mg/mL)**	**Sacrificial agent**	**HER rate ($mmolg^{-1}h^{-1}$)**	**Ref.**
Pt_3Co/CdS	30	2	1M $(NH_4)_2SO_3$	45.1	[115]
Plasmonic AuNP@CoTPy	-	-	0.1% Methanol[a]	3.2	[95]
$Au\text{-}Co/TiO_2$	100	0.5	Methanol	226.0	[93]
$CdS\ (QD)/Co_9S_8$	20	0.2	$Na_2S + Na_2SO_3$	1.06	[113]
$Ag@CoFe_2O_4/g\text{-}C_3N_4$	5	0.1	TEOA	0.3	[105]
Co_2P/RP	-	-	Na_2S/Na_2SO_3	5.9	[106]
Co_3O_4	50	1	TEOA[a b]	0.6	[99]

$CuCo_2O_4$/g-C_3N_4	10	0.1	20% TEOA[a]	4.1	[102]
$Cu_{0.9}Co_{2.1}S_4$@MoS_2	1	0.04	5.3% TEOA[a]	40.2	[103]
$NiCo_2O_4$/$Mn_{0.05}Cd_{0.95}S$	30	0.3	0.35M Na_2S + 0.25M Na_2SO_3	17.0	[111]
$Mn_{0.2}Cd_{0.8}S$/MoS_2/Co_3O_4	5	0.5	0.5M Na_2S, 0.5M Na_2SO_3	16.5	[110]
MoS_2/Co_3O_4	30	0.15	Na_2SO_3 & 10% lactate	3.8	[114]
Commercial Co_3O_4	20	0.5	TEOA[a]	0.03	[d]
Commercial Co_3O_4	20	0.5	Na_2S/Na_2SO_3[b]	0.2	[d]
Co_xO_y	20	0.5	TEOA[a]	0.3	[d]
Co_xO_y	20	0.5	Na_2S/Na_2SO_3[b]	0.3	[d]
1.5 $MoS_2Co_xO_y$	20	0.5	TEOA[a]	11.2	[d]
1.5 $MoS_2Co_xO_y$	20	0.5	Na_2S/Na_2SO_3[b]	16.6	[d]

[a] volume percent, [b]10% TEOA and [c] 1.25M Na_2S + 1.75M Na_2SO_3, [d] This work.

In this study, it is worth mentioning that the HER rates between the modified 1.5 $MoS_2Co_xO_y$ and unmodified sample differs by two orders of magnitude. This is attributed to the change in crystalline and electro-chemical properties inferred from spectral peak shift, lattice broadening, diffraction redshift, XRD and increase concentration of Co^{3+} species where Co^{3+} species are more likely to be the reactive towards water dissociation observed at XPS analyses. In addition, the optical study concludes that the enhanced light harvesting properties, narrowed band gap and the reduced excitons recombination deduced from UV-Vis-NIR and PL analyses, respectively. This study also compares the HER performance of the photocatalysts in TEOA and sodium sulfide/sulfite systems in the same process conditions. Both sacrificial agents are commonly used in photocatalysis systems involving cobalt based nanomaterials. The effective quenching of generated holes that enhances the migration of the holes to the conduction band instead of electron-hole recombination is enabled by the use of sacrificial agents. The Z-scheme heterojunction established between the MoS_2 and Co_xO_y interface facilitates the charge transfer as illustrated in supplementary data Figure S5.1.

5. Conclusion:

A Co_xO_y photocatalyst has been synthesised using a fast and reliable microwave digestor which exceeded performance better than the commercial Co_3O_4 for the HER utilising two sacrificial agent systems (TEOA and Na_2S/Na_2SO_3). After modification with MoS_2 the heterojunction 0.5-1.5 $MoS_2Co_xO_y$ photocatalysts have shown significant increase in the H_2 evolution rate compared to the undoped Co_xO_y photocatalyst (34 and 55 times). This enhancement is due to better light absorption, electron-hole separation and electronic changes within the photocatalyst. Further, the photocatalyst testing in the two sacrificial agent systems of TEOA and a mixture of 1.25 M Na_2S and 1.75 M Na_2SO_3 demonstrated that Na_2S/Na_2SO_3 system facilitated the photocatalytic performance and increased the hydrogen generation by 1.4 times over the TEOA system due to the two active sulfide/sulfite species involved in the photoreaction. Lastly, the cyclic test revealed that photocatalyst can retain its three-cycle performance over 12 hours of test runs with good performance stability. This study has shed light in the understanding the performance efficiency and mechanism of sacrificial agent for microwave derived MoS_2 and cobalt based heterojunction photocatalysts.

Credit authorship contribution statement

Upalee Labhane: Conceptualization; Data curation, Writing - original draft. **Zelio Fusco**: Characterization, data analysis. **Jia Ding**: Data analysis. **Yi-Chen Lin**: Characterization, data analysis, experimental design. **Hashim Jalil Khan**: Characterization, data analysis. **Sarina Sarina**: writing review and editing, **David Alam**: reaction design, writing review and editing. **Sergio Londono**: writing review and editing, **Alejandro Montoya**: writing review and editing, **David K. Wang**: supervision, writing review, editing, funding acquisition.

Declaration of Competing Interest

The authors declare no competing financial interest.

Acknowledgement.

The authors gratefully acknowledge the financial support given by the Australian Research Council (DP190101734) and Sydney Southeast Asia Centre Collaborative Research Grant. We also acknowledge the facilities from Sydney Analytical and Australian Centre for Microscopy and Microanalysis.

Supporting Information:

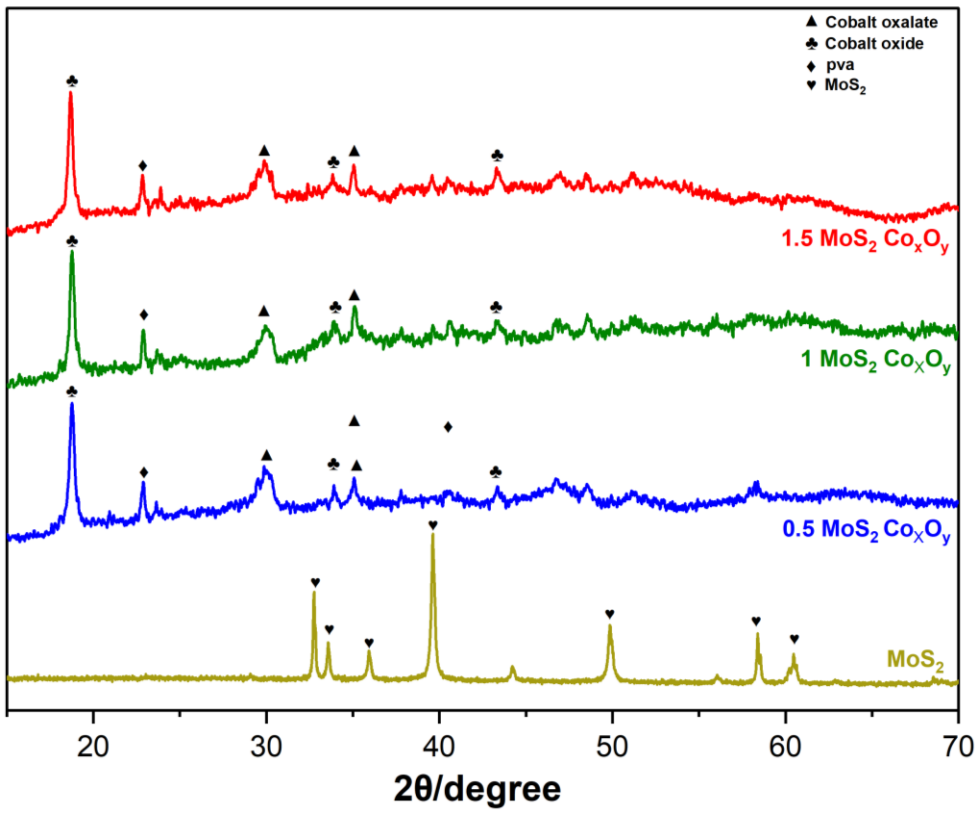

Figure 32 S1.1 XRD for All modifications and Pure MoS2.

All the peaks in pure MoS_2 disappeared in the heterojunction because of two reasons: 1. The quantity of MoS2 as compared to cobalt nanomaterial is quite minimal so it cannot be dedicated by the XRD instrument. 2. The peaks of MoS2 are undiscernible because they are shielded by the strong peaks from cobalt nanomaterial [268]. The additional peak at 23.9 θ is indexed to the crystalline (111 plane) of S element from MoS_2 [269]. No peak changes for pva peaks are observed.

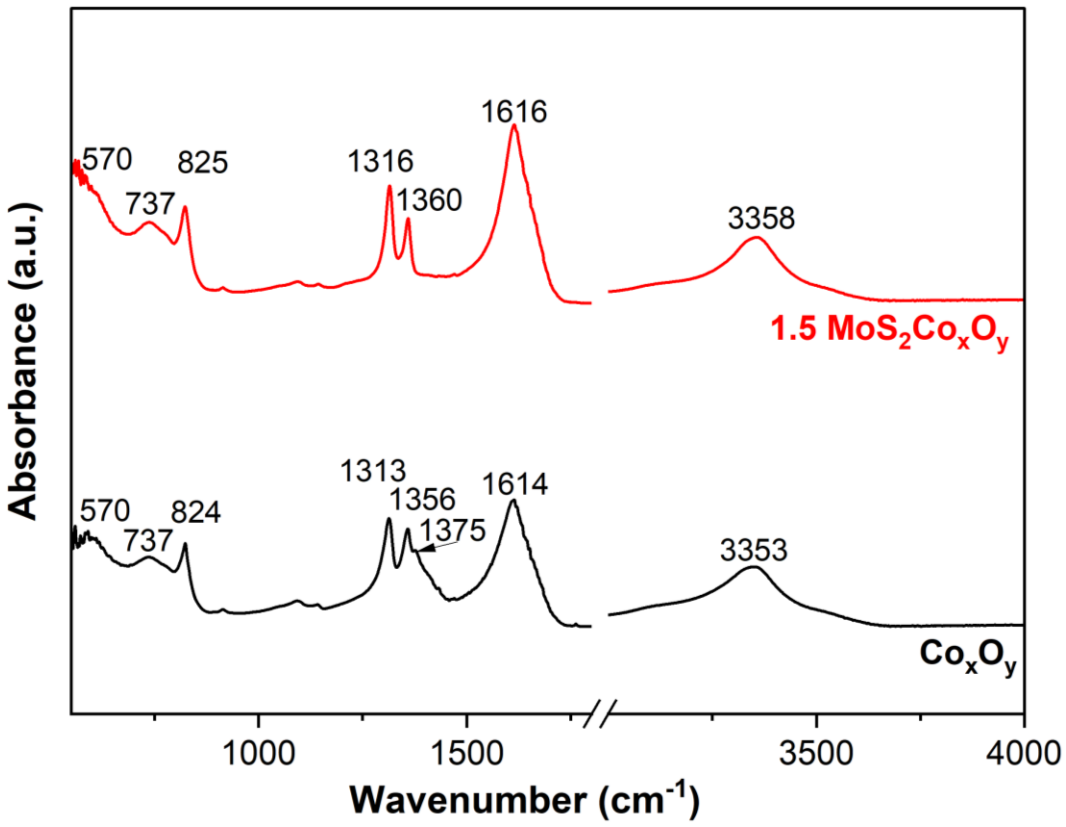

Figure 33 S2.1 FTIR for pure CoxOy and modified 1.5 MoS2CoxOy

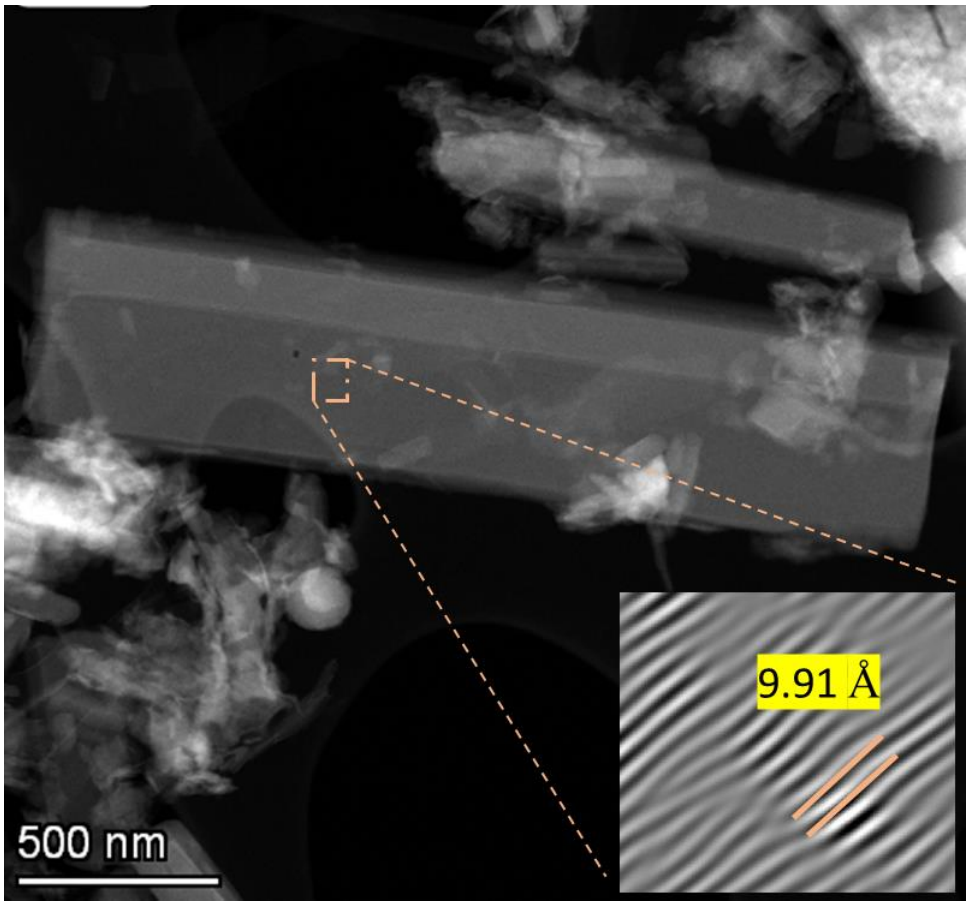

Figure 34 S3.1 HRTEM 1.5 MoS2CoxOy inset interlayer d-spacing that shows the enhanced lattice space to 9.91 nm due to the addition of MoS2.

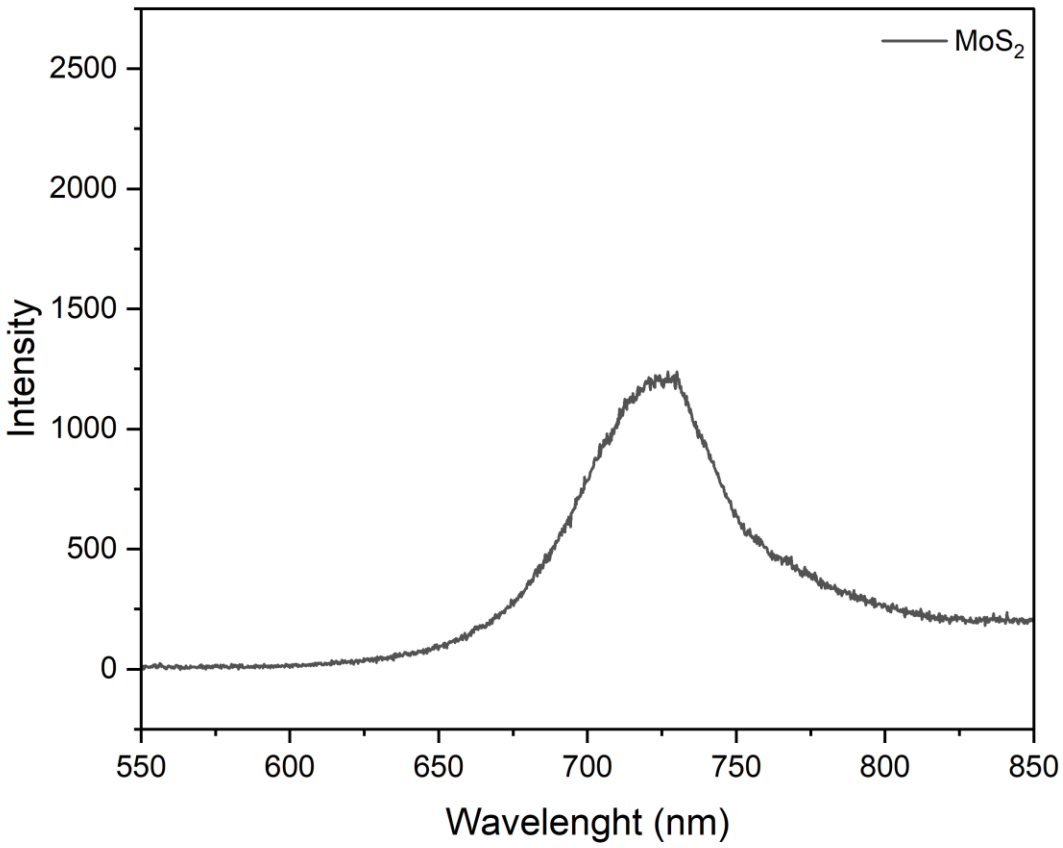

Figure 35 S4.1 PL spectra for Pure MoS2 that has a spectrum between 650 -750 nm however for the remaining wavelength the photocatalyst does not show a distinctive peak.

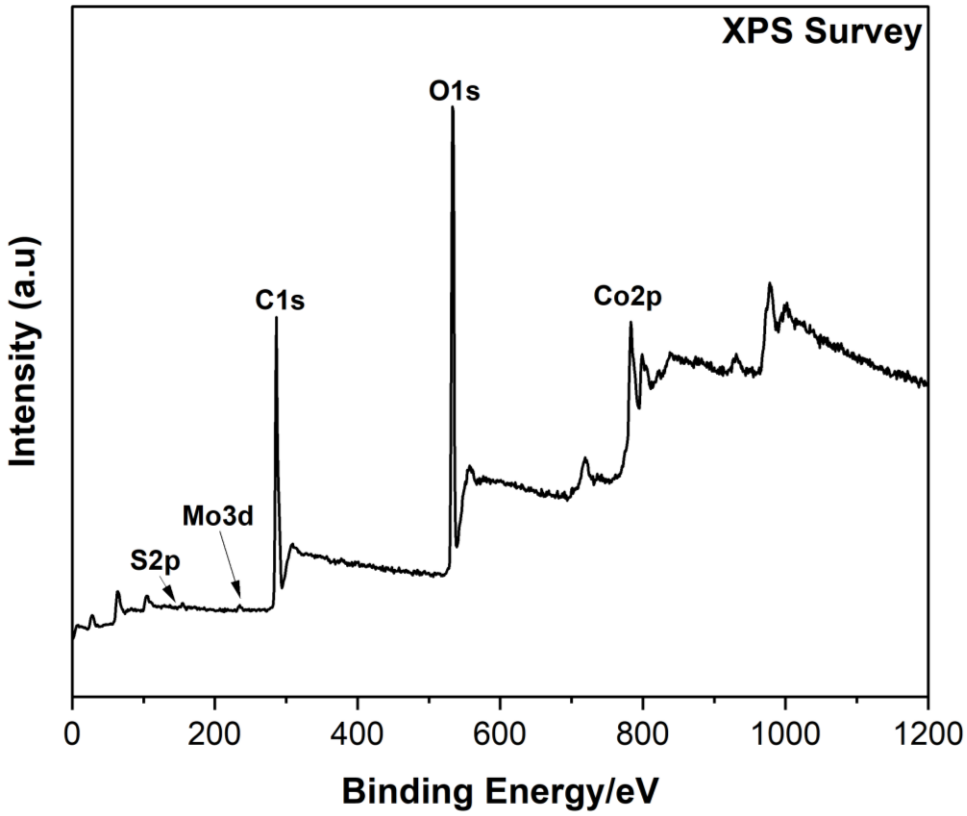

Figure 36 S5.1 XPS survey spectra discussing the presence of Co2p, O1s, C1s, MoS3d, and S2p.

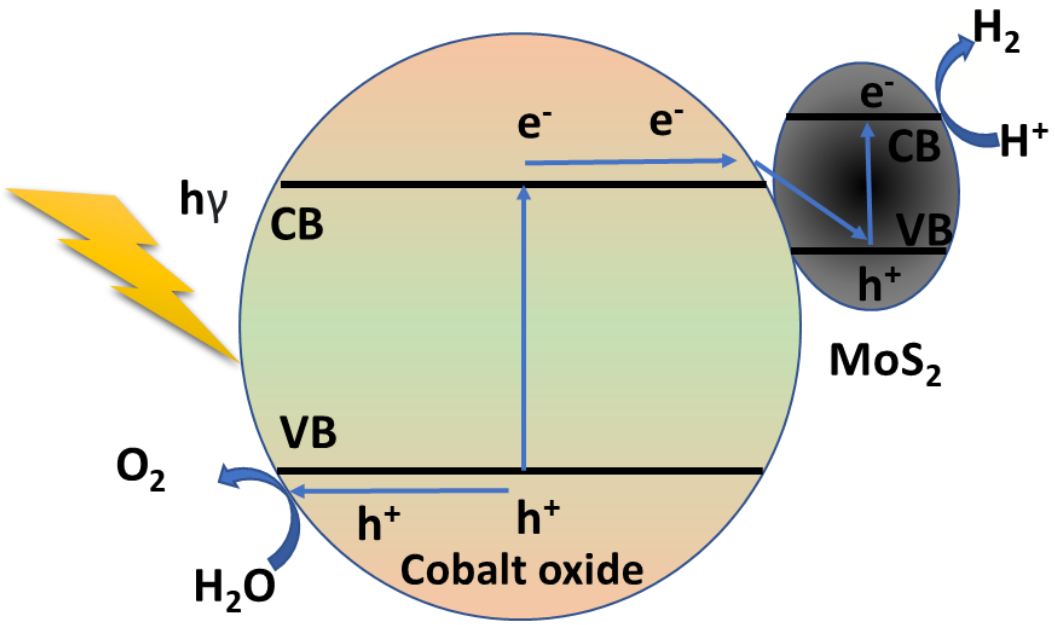

Figure 37 S6.1 Z-scheme heterojunction formed between MoS2CoxOy photocatalyst showing the charge transfer from CB of CoxOy to VB of MoS2.

Chapter 5. comparison Between MoS_2QD and MoS_2bulk

This short chapter highlights the key differences and observations that are derived from comparing the following characterisation results. For detailed findings and explanations, one should be referred to Chapters 3 and 4 for modified cobalt oxide photocatalyst with MoS2QD and MoS2Bulk, respectively. In chapter 3, MoS_2QD were incorporated to investigate the effects of quantum confinement and photoluminescence induced QDs and its combination with Cobalt oxide in a custom-made quartz reactor. Later these findings were compared and benchmark against the conventionally explored MoS_2bulk material to critically understanding the effect of MoS structure in an upgraded stainless-steel reactor with a quartz window. In our study we observed that the MoS_2QD had an improved effect on cobalt oxide for HER. Similarly, the latter reactor offered significant improvement in light confinement and photocatalysis reactor optimisation. For all figures in chapter 5, sample code '1p' is the same as 'Co_xO_y' which follows the similar sample codes in Chapter 3 and 4, respectively.

Figure 38 is the comparative XRD analysis of the modification by MoS_2QD and MoS_2bulk. First of all, common observation in Figure 38 (a) (1p), Figure 38 (b) (Co_xO_y), have the presence of cobalt tetraoxide (Co_3O_4, monoclinic) and cobalt oxalate (orthorhombic) phase. These two phases are identified in all modifications (QD and Bulk). The major difference in cobalt oxides photocatalyst due to the QD size confinement are in the latices compression from 6.33 Å to 6.05 Å for 1QD1p modification and contrasting the modification due to the S-Mo-S bulk sheets (1.5 $MoS_2Co_xO_y$) results in lattice expansion from 7.63 Å to 9.91 Å. Another noteworthy observation in the comparative XRD is the peak shift restricted only for MoS_2bulk (Figure 38 (b)), particularly 18.7° and 19.1° 2θ were merged into a single broad peak at 18.7° 2θ and a peak at 29.8° 2θ is a

result of shift from 30.3° 2θ. This peak merger and shift are attributed to the lattice expansion as explained in chapter 4 (Chapter 4 section 3.1 XRD).

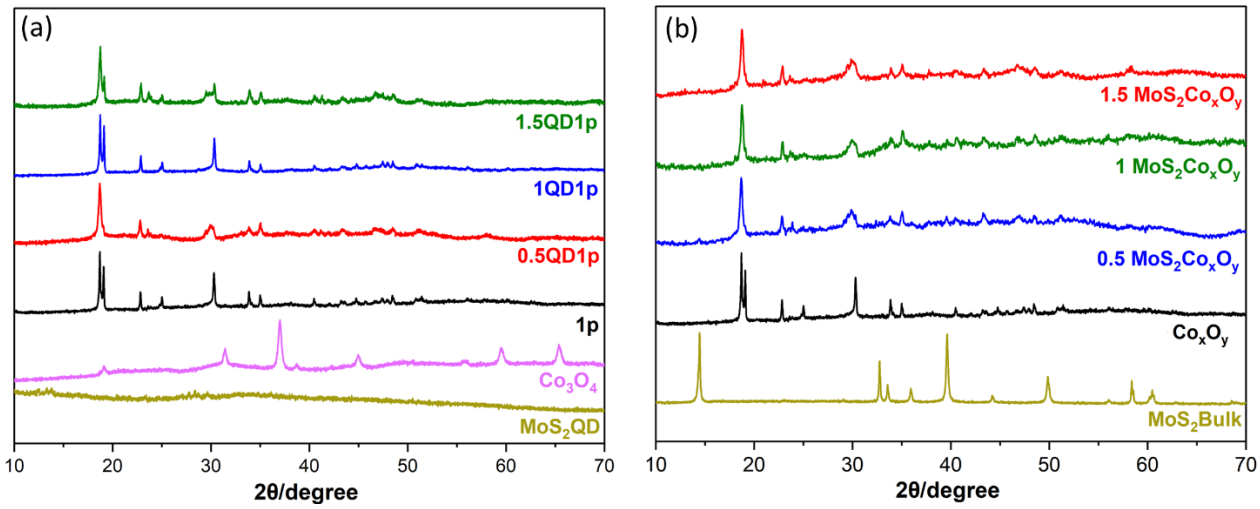

Figure 38. XRD comparison of the modified cobalt oxide sample with MoS2QD (a) and MoS2Bulk (b).

5.1 XPS comparison

Figure 39 presents the comparative analysis of MoS_2QD and MoS_2bulk, respectively. For Co2p spectra shown in Figure 39 (a), we have obvserved a redshift of 2 eV (chapter 3, section 3.4 X-ray photoelectron spectroscopy) for MoS_2QD and and 5 eV (chapter 4, section 3.2 X-ray photoelectron spectroscopy) for MoS_2bulk that indicates the change in the electronic denisty. For MoS_2bulk, additonal energy peaks for both Co2p3/2 and Co2p1/2 peaks are observed at 781.5 eV and 797.5 eV (chapter 4, section 3.2 X-ray photoelectron spectroscopy). These peaks are absent for MoS_2QD photocatalyst as due to the size confiment of QDs. For O1s spectra shown in Figure 39 (b), the MoS_2QD two peaks are shown as Co-O bonding and an hybridisation peak. In MoS_2bulk sample, four peaks were observd in which two corrosponds to metal oxide, one for metal oxyhydroxide,

and a water peak, this could arise from the mositure abosrbed while sample preaparation for XPS (chapter 4, section 3.2 X-ray photoelectron spectroscopy). The presence of MoS_2 as Mo3d spctra is shown in Figure 39 (c, d) where 1T MoS_2 phase has been obserbved and followed by 2H MoS_2 phase (Figure 39 (d)) these peaks are not as prominent for QDs as they inherit the smaller sized (approaching to Bohr radius [62]) monolayered QD arraingment. S2p spectrum shown in Figure 39 (e, f) both does not show any peak addition or major changes except the formation of sufonic group and bonding with oxygen. XPS survey in Figure 39 (g, h) does not show any addition of peaks resembling impurities.

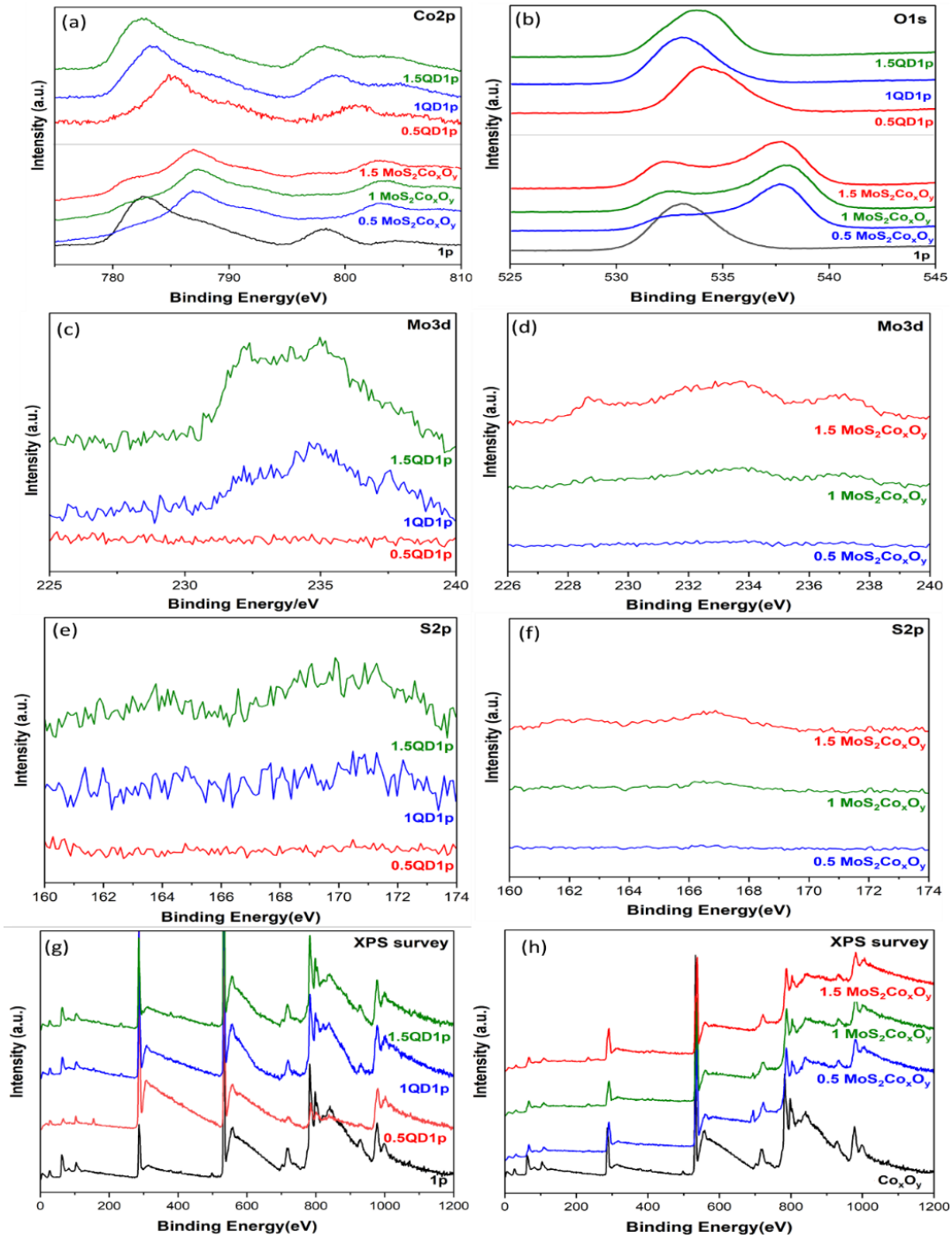

Figure 39 XPS comparison of the modified cobalt oxide sample with MoS_2QD and MoS_2Bulk. Co2p spectra (MoS_2QD, top and MoS_2Bulk, bottom) (a), O1s spectra (MoS_2QD, top and MoS_2Bulk, bottom) (b), Mo3d spectra (MoS_2QD) (c), Mo3d spectra (MoS_2bulk) (d), S2p spectra (MoS_2QD) (e), S2p spectra (MoS_2bulk) (f), XPS survey (MoS_2QD) (g), XPS survey (MoS_2bulk) (h),

5.2 PL comparision

Figure 40 shows the comparison of PL spectra between MoS_2QD (a) and MoS_2bulk (b). Notably in Figure 40 (a), MoS_2QD does not show PL spectra because of instrument limitations (The analysis PL work station used was equipped with 550 nm light source whereas excitations of MoS_2QD requires UV range light source). In contrast to that is the stand alone Co_3O_4 and 1p sample showing the highest spectra indicating significant recombition phenomenon (Figure 40 (a)) as discussed in chapter 2 section 2.3. Cobalt oxide faces high recombination rate as a standalone photocatalyst. MoS_2bulk shows PL spectra for a narrow region between 700 nm to 750 nm shown in Figure 40 (b) attributed to the charactersitics of MoS_2 exitation range hence the HER performance is low. Figure 40 (a) the PL spectra is in the following order 1QD1p < 1.5QD1p < 0.5QD1p <1p < Co_3O_4, thus the HER for 1QD1p is highest while for Co_3O_4 is lowest. For Figure 40 (b) the PL spectra is in the following order 1.5 $MoS_2Co_xO_y$ < 1 $MoS_2Co_xO_y$ < 0.5 $MoS_2Co_xO_y$ <MoS_2bulk< Co_xO_y. These trends are as is reflected in the HER performance of the photocatalyst due to electron hole recombination characteristics. The remaining details regarding PL spectrum are shown in chapter 3 section 3.1 (MoS_2QD) and chanpter 4 section 3.5 (MoS_2bulk).

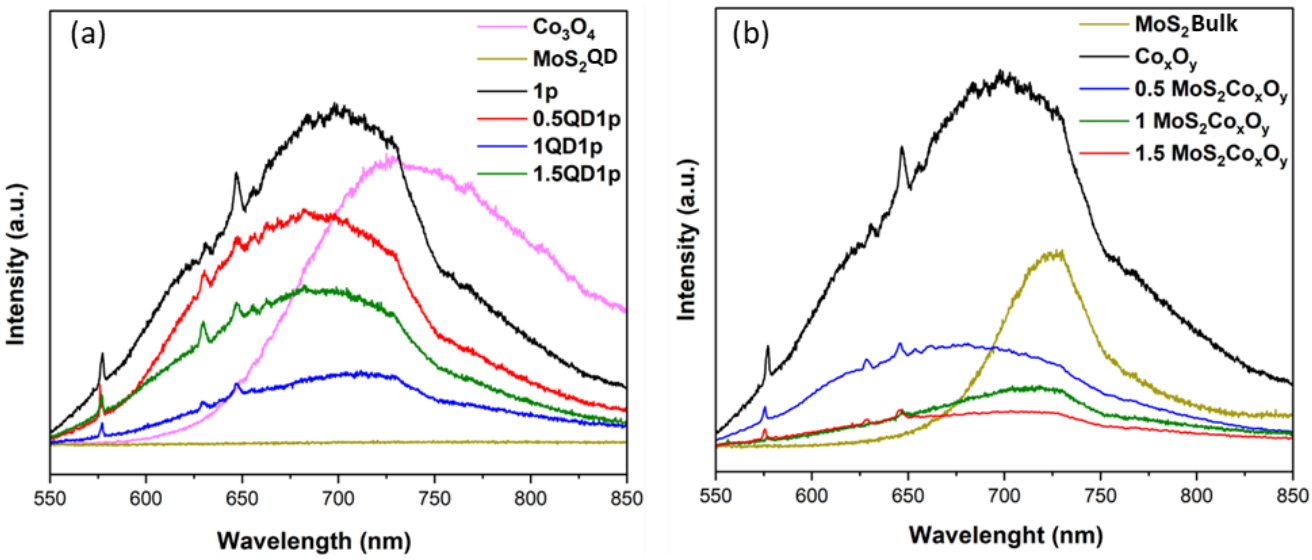

Figure 40 shows the PL comparison between MoS2QD (a) and MoS2bulk (b).

5.3 UV Vis NIR comparison

Figure 41 shows the UV-Vis-NIR comparison between MoS_2QD (a) and MoS_2bulk (b). For the commercial sourced Co_3O_4 Figure 41 (a) showed a considerbale light absorbance in the visible range, this increase in the visible light absorption can be ascribed to O^{2-} to Co^{3+} charge transfer, followed by a major dip in the 750 nm – 1100 nm range and large intensity flutuations (noise) in the NIR. It can be due to the change in instrument's ligh detector for NIR region for this perticaluar sample [258]. Along with that, MoS_2QD shown in Figure 41 (a) and MoS_2bulk shown in Figure 41 (b) have a common observation regarding adequate absorption in visisble light range whichaligns with MoS_2's characteristic excitation range. However, for MoS_2QD the UV range photoresponse is better than bulk, which can be attributed to quantum confiment and photoluminescence [132]. Along with that the size alteration of MoS_2QD results in the enhancement of photoluminescence properties [134]. After both modifications, the band gaps has been reduced by 0.05 eV.

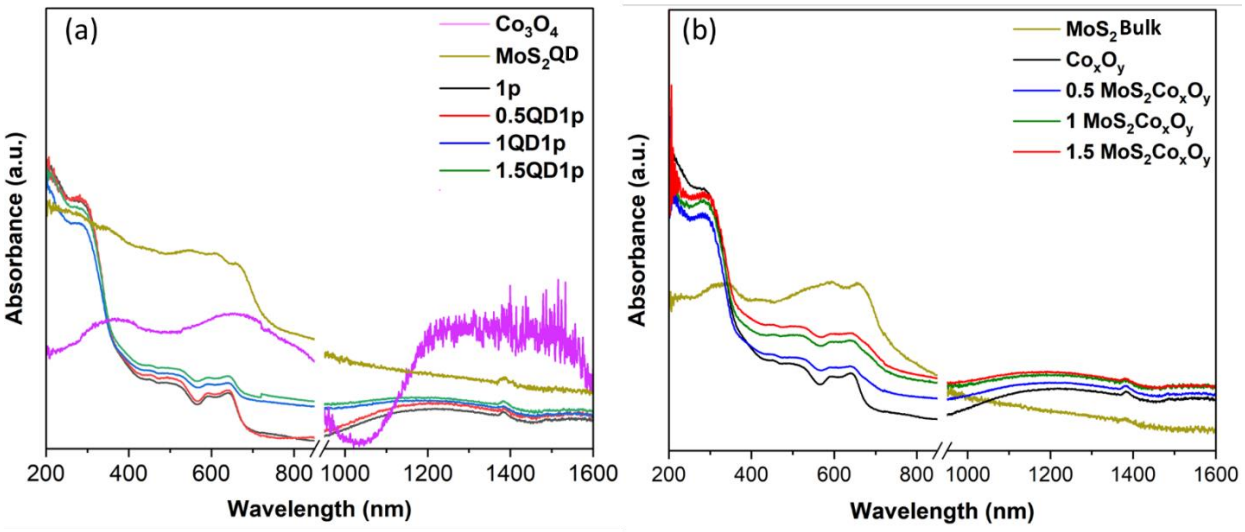

Figure 41 shows the UV-Vis-NIR comparison between MoS2QD (a) and MoS2bulk (b).

5.4 SEM comparison

Figure 42 shows the SEM image with elemental mapping of MoS_2QD (a) and MoS_2bulk (b). The common observations in both samples are the mixed structure of cobalt oxide that comprises of rods and spheres. As reported by Zhang et al, MoS_2QD and MoS_2bulk are likely attached to another solid nano-construct by Van der Walls force [212]. The increased in Mo concentration from 4.5 atom% to 7.63 atom% is observed in 1QD1p and 1.5 $MoS_2Co_xO_y$. Where the concentration is increased from 1 wt% to 1.5 wt%. Sulfur cannot be detected owing to the limitations of SEM element analyser.

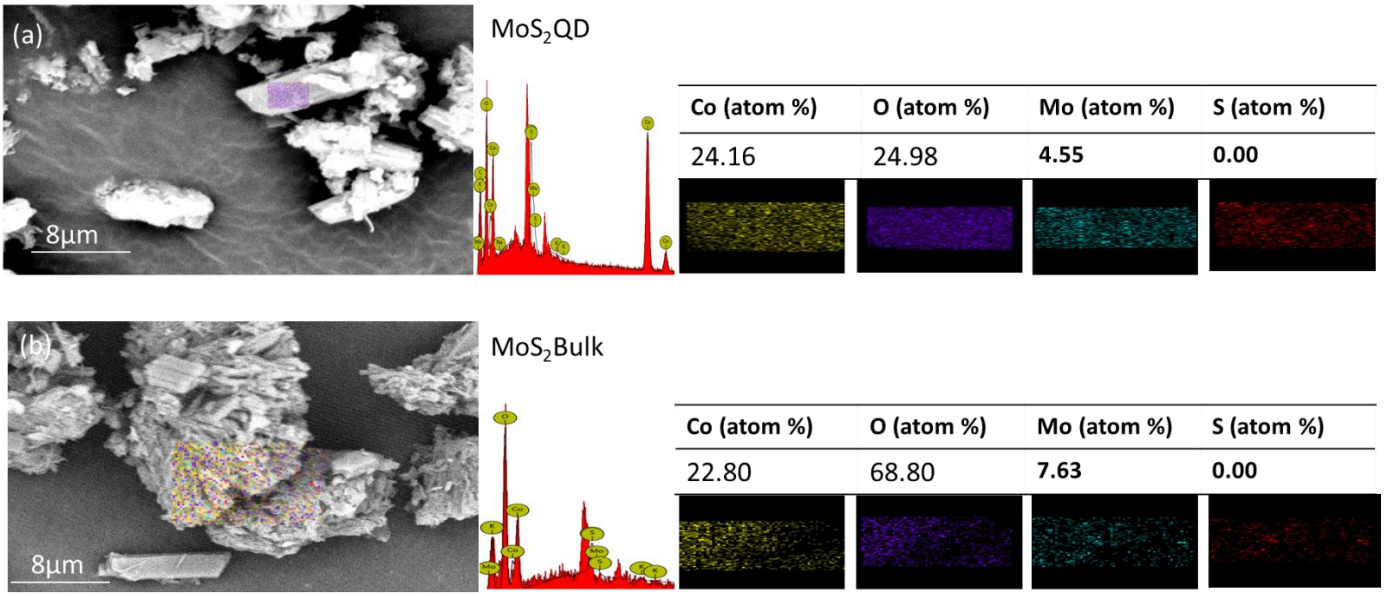

Figure 42 shows the SEM analysis along with elemental mapping MoS2QD (a) and MoS2bulk (b)

5.5 Photocatalytic reactor design.

System 1 (Borosilicate Glass reactor along with online gas sampling).

Figure 43 (a) and (b) shows the first system, that included a glass reactor with a cooling water circulating system to maintain 25^{o}C and a microGC. Fitted with quartz glass window on the top for light penetration. However, the design challenge for this system is the inability to keep airtight conditions. This was translated into several leaks either form the gasket on top of the reactor that separated the quartz window and the borosilicate glass reactor body, or the regulator nobs mentioned in Figure 43 (a). Additionally, an inline hydrogen detection line was designed that had a mass flow controller on one end equipped with 30 SCCM Argon gas, passing through the reactor and entering the microGC for hydrogen detection.

To troubleshooting the leaks, a custom design was suggested for fabrication so as to modify the glass reactor. This approach included the GL14 fittings the at the input and output ends shown in

Figure 43 (b) that reduced the challenges but did not eliminate. Also, a moisture cold trap was designed to condense the moisture traveling to the GC thus preventing the damage shown in Figure 44 (c). Finally with the limitations persisting, a new design setup was proposed.

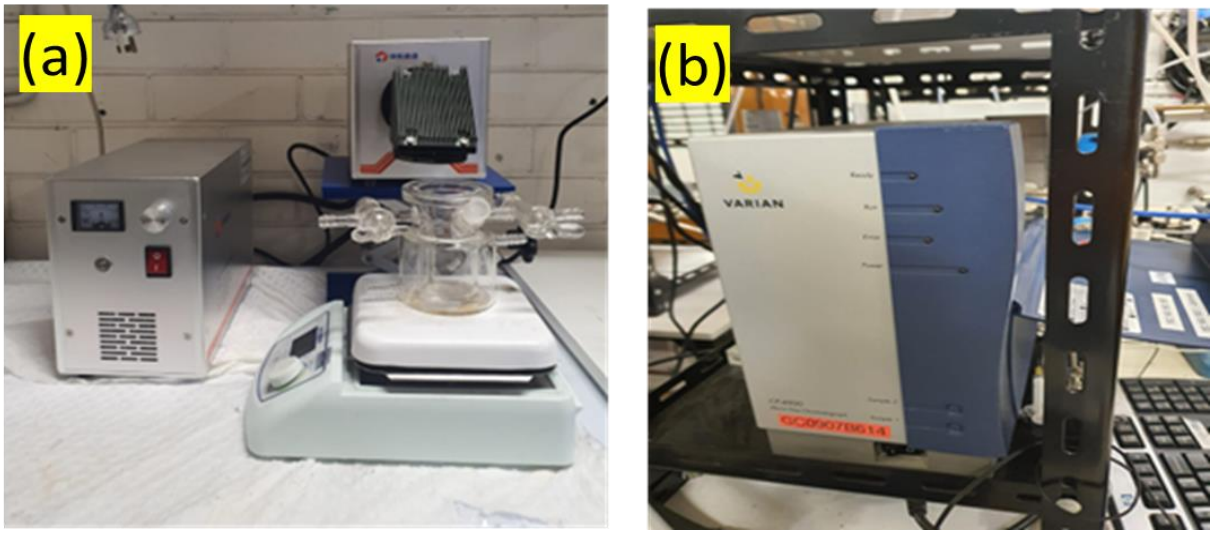

Figure 43 shows the system one that included glass reactor (a) with a microGC for gas analysis (b).

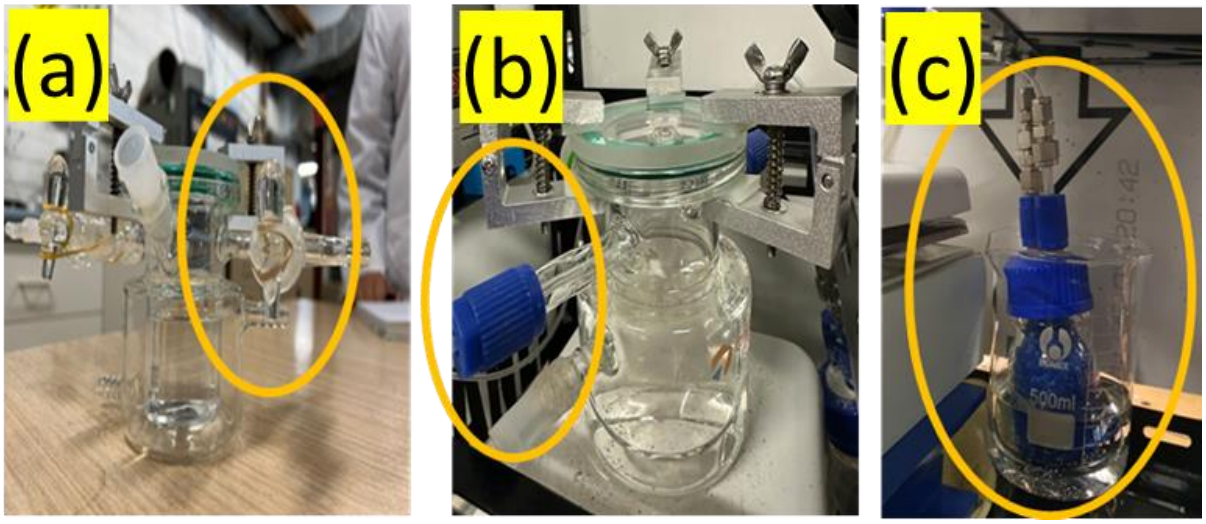

Figure 44 Trouble shooting for glass reactor system. Glass nobs (a), modified GL14 fittings (b), cold moisture trap (c).

System 2 (Stainless steel reactor with manual injection for gas sampling)

Figure 45 (a, b c) shows a completely new partially custom-made stainless-steel reactor system was sourced that included Swagelok fittings and a quartz glass on the top for light penetration. The reactor was maintained at 25^{o}C and 0.9 bar pressure. A manual gas injection setup was adopted for produced hydrogen gas analysis to a PerkinElmer GC Arnel 590 shown in Figure 45(c, d).

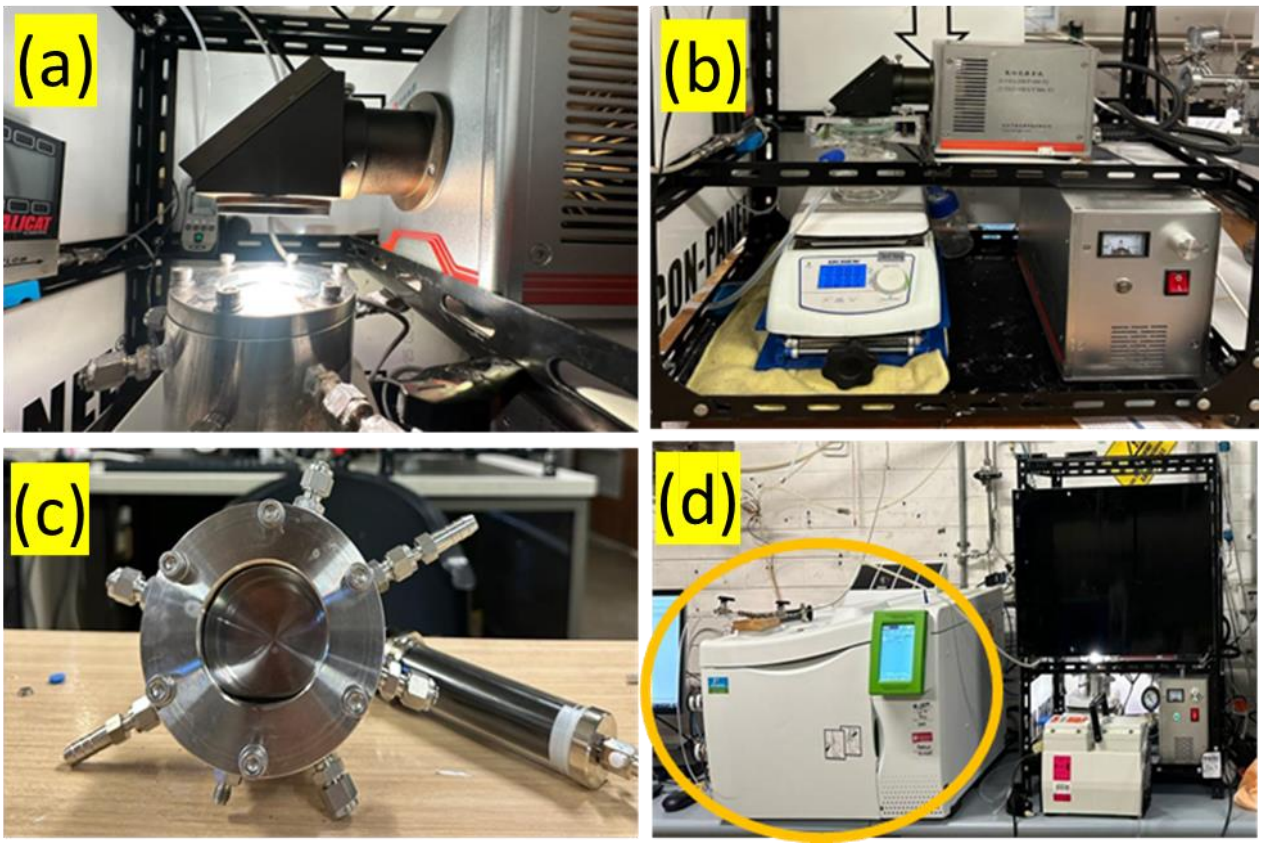

Figure 45 Setup two with stainless steel reactor with gas tight syringe and PerkinElmer GC.

This Stainless-steel reactor system was employed for MoS_2Bulk heterojuntion photocatalytic experimations (Chatper 4) and additional experiments with DI water in the absence of SA. The

results are in line with the same trend as SA systems. Where 0.6 mmolg^{-1}h^{-1}, 0.3 mmolg^{-1}h^{-1}, 0.1 mmolg^{-1}h^{-1}, 0.01 mmolg^{-1}h^{-1} hydrogen yield was observed for 1.5 $MoS_2Co_xO_y$, 1 $MoS_2Co_xO_y$, 0.5 $MoS_2Co_xO_y$, Co_xO_y respectively. Following the modification with MoS_2bulk, the photocatalyst showed an increament of 1 fold. However a low hydrogen yield of 0.006 mmolg^{-1}h^{-1}, 0.01 mmolg^{-1}h^{-1} was observed for Commercial source Co_3O_4 and MoS_2Bulk respectively shown in Figure 46 (a, b). The reduced HER performance with the DI water system can be attributed to the absence of electron donor and hole quenching mechanim of the sacrificial agents and reducing the facilitation of thermodynamic barrier. Also, 1QD1p sample was test for DI water system and it recorded a 1.26 mmolg^{-1}h^{-1} hydrogen yield shown in Figure 46 (c,d).

To comprehend the disparity in the hydorgen yeild between glass setup and stainless steel system, a photocatalyst of interest (1QD1p) was chosen. A significant increament in the amount of hydorgen produced was recorded from 0.0018 mmolg^{-1}h^{-1} for the glass reactor to 1.26 mmolg^{-1}h^{-1} for stainless streel reactor (shown in Figure 46 (e)). This increment in HER is attributed to the design configuration of the photocatalytic rector. It was noted that different researchers employ unique setups by studying researches concluded from a few examples from Table 1, with variations in vacuum conditions, sampling system, and gas detection so it is difficult to standardize the photocatalytic evaluation reaction system. According to the review by Xing et al., [270] there are various factors influencing the hydrogen performance including the light source, reactor configuration and material (in this case glass and stainless steel), vacuum condition (the glass rector was under atmospheric pressure and stainless steel was under vacuum conditions, this system eliminates the presence of other competing gas for detection, and vacuum assist the transfer of the gas from the solid catalyst surface to gaseous phase) thus enhancing the performance. Also, for the glass reactor the incident light escaped after traveling from the source into the reactor

however in the stainless-steel reactor the light was trapped within hence provided enhanced light exposure to the photocatalyst.

Figure 46 (f) shows the highest recorded hydrogen yield for 1QD1p sample with, 1.26 $mmolg^{-1}h^{-1}$, 16.3 $mmolg^{-1}h^{-1}$ and 17.5 $mmolg^{-1}h^{-1}$ for DI water, 9.1 (v/v) of TEOA respectively, 1.25M (Na_2S) + 1.75M (Na_2SO_3) respectively.

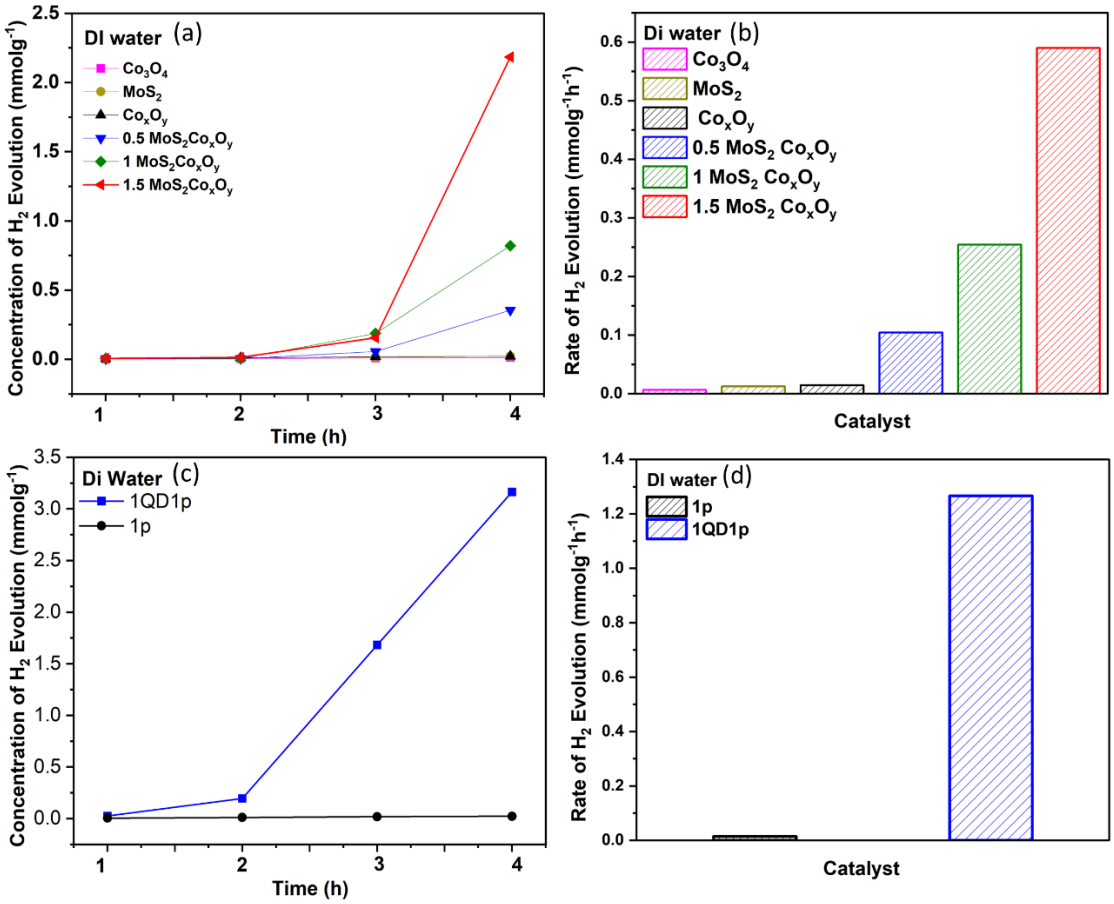

(e)

Rate of hydrogen evolution (mmol $h^{-1}g^{-1}$)	Catalyst (1QD1p)
0.002	Glass reactor
1.26	Stainless steel reactor.

Figure 46 Hydrogen yield for DI water system with System two. MoS2bulk with DI water (a, b), 1QD1p (c, d) and comparison of 1QD1p with and without sacrificial agents (e), change in hydrogen yield from glass reactor to stainless steel reactor.

In summary, Chapter 5 discusses the importance of engineering design in choosing the appropriate reaction system to measure the hydrogen rate. Shown in this chapter, the reduced HER for 1.5 $MoS_2Co_xO_y$ in DI water system due to the absence of electron doners (sacrificial agent) that facilitates the thermodynamic barrier. Importantly, upgrading the system from glass reactor to stainless steel under vacuum have significantly increased the HER by 3 folds. Also, HER under DI water and two SA system has been demonstrated that implies the formed 1QD1p photocatalyst shows HER under all three systems.

6 Conclusions & Recommendations

In conclusion, cobalt oxide being a well-established photocatalyst faces limitations owing to its semiconduction characteristics nature such as electron-hole recombination, light absorption, limited active sites for photocatalysts, charge density and insufficient band gap. Additionally, from the synthesis perspective, the synthesis time for cobalt oxide is larger (average of 21 hours for hydrothermal and solvothermal) that poses a significant issue regarding energy consumption to maintain the required high temperature. To address the characteristic limitations, we have proposed the use of MoS_2QD and bulk as a co-catalyst. Both the strategies have been successful in overcoming the limitations of cobalt oxide due to MoS_2's posing a direct band gap, edge effect, sulfur atom's affinity towards hydrogen, improved charge transfer and migration that limits the electron hole recombination (chapter 2 section 2.2.3 and 2.4). Specifically, to MoS_2QD, the high volume to surface ratio, quantum confinement effect, photoluminescence, up-conversion effect served a critical role. One of the novelty lies in the innovative use of microwave irradiation for the rapid synthesis of cobalt oxide and MoS_2QD that reduces the time required from an average of 21 hours to 2 minutes.

In terms of HER, the conclusion of this thesis can be categorised into three sections.

Chapter 3 investigated the MoS_2 quantum dot and the Z-scheme heteojunction phtocatalyst resulted an increased HER from 0.07 µmol $h^{-1}g^{-1}$ (unmodified cobalt oxide (1p)) to 1.8 µmol $h^{-1}g^{-1}$ (modified cobalt oxide (1DQ1p)) in the absence of sacrificial agents (SA).

In the succeeding Chapter 4, the use of both MoS_2 bulk and SA significantly enhanced the HER performance by three orders of magnitude from 0.3 mmol$g^{-1}h^{-1}$ (Co_xO_y) to 11.21 mmol$g^{-1}h^{-1}$ (1.5

$MoS_2Co_xO_y$) for 9:1 TEOA, and 0.32 $mmolg^{-1}h^{-1}$ (Co_xO_y) to 16.64 $mmolg^{-1}h^{-1}$ (1.5 $MoS_2Co_xO_y$) for $Na_2S+Na_2SO_3$.

In Chapter 5, equivalent 1QD1p and 1.5 $MoS_2Co_xO_y$ sample were compared and discussed. 1QD1p sample showed HER of 16.3 $mmolg^{-1}h^{-1}$and 17.5 $mmolg^{-1}h^{-1}$ (Figure 46 (f)) for TEOA and $Na_2S+Na_2SO_3$. Also, for DI water system HER of 0.6 $mmolg^{-1}h^{-1}$ compared to 1.26 $mmolg^{-1}h^{-1}$ for 1.5 $MoS_2Co_xO_y$ and 1QD1p respectively, where 1QD1p sample shows double HER over 1.5 $MoS_2Co_xO_y$.

Conclusion and reasoning regarding HER, the microwave synthesised cobalt oxide along with optima concentration of pva showed higher photocatalytic performance compared to commercially source Sigma Aldrich (Merk) Co_3O_4 and MoS_2 in unmodified form. Notably, both MoS_2QD and MoS_2Bulk modifications have led to substantial two and three fold increase for the hydrogen yield. This increament can be attributed to electronic properties characteristed by XRD, XPS that revealed the lattice contraction for MoS_2QD from 6.33 Å to 6.05 Å and expansion for MoS_2Bulk from 7.63 Å to 9.91 Å, along with increased Co^{3+} species concentration after QD modifications (1:4 to 1:3.5) and bulk (1:4 to 1:2). Furthermore, the opitcal properties characterisation by UV-Vis-NIR showed a reduction in band gap energy (0.05 eV) and from PL spectra additional confirmation on reduced recombination was concluded (1QD1p and 1.5 $MoS_2Co_xO_y$). The enchaced performance was further substantiated by the foramtion of Z-scheme heterojunction between the base and co-catalyst. Thus, it can be concluded that the synthesised base catalyst and co-catalyst employing microwave synthesis method represents the effective strategy with promising future applications. This work contributes to the sustainable and effective hydrogen production for rising energy needs.

Recommendations based on the finding of this work,

1. Synthesis of the cobalt oxide base photocatalyst by systematically varying microwave synthesis time and magnetron power should be comprehensive investigated. As reviewed in section 2.6, increasing magnetron power leads to faster heating, which results in unique heterojunction structure of the photocatalyst, and thus changes the reaction kinetic.
2. A range of semiconductor material as base and co-catalyst can be investigated for photocatalyst synthesis via microwave technique. This can further confirm that a variety of semiconductors can be synthesised using microwave thus making it a versatile synthesis technique.
3. The photocatalytic reaction can be conducted with increased temperatures for better phase separation of the gaseous molecules. In the section 2.2.2, current state of art, demonstrates that the pH and temperature of the photocatalytic system influences the HER thus an optimal HER conditions can be investigated.
4. The used of monochromatic light can be investigated to observe the hydrogen yield as light of specific wavelength is beneficial for the better performance of the photocatalyst.
5. Study on sacrificial agents can add value in choosing the best suited SA. As the Table 1. Shows the use of different SA like Lactic acid and others in general can influence the HER of a give photocatalyst.

References

1. Ramachandran, R. and R.K. Menon, *An overview of industrial uses of hydrogen.* International Journal of Hydrogen Energy, 1998. **23**(7): p. 593-598.
2. Alwazeer, D., et al., *Evaluation of the impact of hydrogen-rich water on the deaccumulation of heavy metals in butter.* Journal of Food Safety, 2022. **42**(6): p. e13005.
3. Yue, M., et al., *Hydrogen energy systems: A critical review of technologies, applications, trends and challenges.* Renewable and Sustainable Energy Reviews, 2021. **146**: p. 111180.
4. Cecere, D., E. Giacomazzi, and A. Ingenito, *A review on hydrogen industrial aerospace applications.* International Journal of Hydrogen Energy, 2014. **39**(20): p. 10731-10747.
5. Zemin, J., *Energy Development Trends and Major Energy Conservation Measures**Article published in the Journal of Shanghai Jiao Tong University, No. 3, 1989, a revision of the presentation Jiang Zemin made at the university in March 1989 on his appointment as professor there*, in *Research on Energy Issues in China*, J. Zemin, Editor. 2010, Academic Press: Singapore. p. 53-87.
6. Osman, A.I., et al., *Hydrogen production, storage, utilisation and environmental impacts: a review.* Environmental Chemistry Letters, 2022. **20**(1): p. 153-188.
7. Sathre, R., et al., *Life-cycle net energy assessment of large-scale hydrogen production via photoelectrochemical water splitting.* Energy & Environmental Science, 2014. **7**(10): p. 3264-3278.
8. Mussabek, G., et al., *Kinetics of Hydrogen Generation from Oxidation of Hydrogenated Silicon Nanocrystals in Aqueous Solutions.* Nanomaterials, 2020. **10**(7): p. 1413.
9. Braga, L.B., et al., *Hydrogen production by biogas steam reforming: a technical, economic and ecological analysis.* Renewable and Sustainable Energy Reviews, 2013. **28**: p. 166-173.
10. Vidas, L. and R. Castro, *Recent Developments on Hydrogen Production Technologies: State-of-the-Art Review with a Focus on Green-Electrolysis.* Applied Sciences, 2021. **11**(23): p. 11363.
11. Navas-Anguita, Z., et al., *Revisiting the role of steam methane reforming with CO2 capture and storage for long-term hydrogen production.* Science of the total Environment, 2021. **771**: p. 145432.
12. Holladay, J.D., et al., *An overview of hydrogen production technologies.* Catalysis today, 2009. **139**(4): p. 244-260.
13. Tong, W., et al., *Electrolysis of low-grade and saline surface water.* Nature Energy, 2020. **5**(5): p. 367-377.
14. Kuleshov, N., et al., *Development and performances of a 0.5 kW high-pressure alkaline water electrolyser.* International Journal of Hydrogen Energy, 2019. **44**(56): p. 29441-29449.
15. Vu, M.-H., M. Sakar, and T.-O. Do, *Insights into the Recent Progress and Advanced Materials for Photocatalytic Nitrogen Fixation for Ammonia (NH3) Production.* Catalysts, 2018. **8**(12): p. 621.
16. Asghari, E., et al., *Advances, opportunities, and challenges of hydrogen and oxygen production from seawater electrolysis: An electrocatalysis perspective.* Current Opinion in Electrochemistry, 2022. **31**: p. 100879.
17. Maeda, K., *Photocatalytic water splitting using semiconductor particles: History and recent developments.* Journal of Photochemistry and Photobiology C: Photochemistry Reviews, 2011. **12**(4): p. 237-268.
18. Wunderling, N., et al., *Interacting tipping elements increase risk of climate domino effects under global warming.* Earth System Dynamics, 2021. **12**(2): p. 601-619.
19. Ayers, K.E., et al., *Research Advances towards Low Cost, High Efficiency PEM Electrolysis.* ECS Transactions, 2010. **33**(1): p. 3.

20. Zhang, T., et al., *Co3O4 nanoparticles anchored on nitrogen-doped reduced graphene oxide as a multifunctional catalyst for H2O2 reduction, oxygen reduction and evolution reaction.* Scientific Reports, 2017. **7**(1): p. 43638.
21. Jin, X., et al., *MoS 2 quantum dot decorated gC 3 N 4 composite photocatalyst with enhanced hydrogen evolution performance.* RSC advances, 2016. **6**(58): p. 52611-52619.
22. Ghasemi, F., et al., *A high performance supercapacitor based on decoration of MoS 2/reduced graphene oxide with NiO nanoparticles.* RSC advances, 2017. **7**(83): p. 52772-52781.
23. Terrones, H., F. López-Urías, and M. Terrones, *Novel hetero-layered materials with tunable direct band gaps by sandwiching different metal disulfides and diselenides.* Scientific reports, 2013. **3**(1): p. 1549.
24. Tee, S.Y., et al., *Recent Progress in Energy-Driven Water Splitting.* Advanced Science, 2017. **4**(5): p. 1600337.
25. Yu, J., J. Zhang, and M. Jaroniec, *Preparation and enhanced visible-light photocatalytic H2-production activity of CdS quantum dots-sensitized Zn1−xCdxS solid solution.* Green Chemistry, 2010. **12**(9): p. 1611-1614.
26. Zhu, J., et al., *Recent advances in electrocatalytic hydrogen evolution using nanoparticles.* Chemical reviews, 2019. **120**(2): p. 851-918.
27. Ji, M. and J. Wang, *Review and comparison of various hydrogen production methods based on costs and life cycle impact assessment indicators.* International Journal of Hydrogen Energy, 2021. **46**(78): p. 38612-38635.
28. Lu, Y., et al., *A Critical Review of Sustainable Energy Policies for the Promotion of Renewable Energy Sources.* Sustainability, 2020. **12**(12): p. 5078.
29. Sun, L., et al., *Single-atom catalysts for photocatalytic hydrogen evolution: A review.* International Journal of Hydrogen Energy, 2022. **47**(40): p. 17583-17599.
30. Council, H., *Path to hydrogen competitiveness: a cost perspective.* 2020.
31. Anwar, S., et al., *Recent development in electrocatalysts for hydrogen production through water electrolysis.* International Journal of Hydrogen Energy, 2021. **46**(63): p. 32284-32317.
32. Singla, S., et al., *Photocatalytic water splitting hydrogen production via environmental benign carbon based nanomaterials.* International Journal of Hydrogen Energy, 2021. **46**(68): p. 33696-33717.
33. Manoharan, Y., et al., *Hydrogen Fuel Cell Vehicles; Current Status and Future Prospect.* Applied Sciences, 2019. **9**(11): p. 2296.
34. Pagliaro, M.V., et al., *Carbon supported Rh nanoparticles for the production of hydrogen and chemicals by the electroreforming of biomass-derived alcohols.* RSC Advances, 2017. **7**(23): p. 13971-13978.
35. Mozdzierz, M., et al., *Towards a thermal optimization of a methane/steam reforming reactor.* Flow, turbulence and combustion, 2016. **97**: p. 171-189.
36. Oni, A.O., et al., *Comparative assessment of blue hydrogen from steam methane reforming, autothermal reforming, and natural gas decomposition technologies for natural gas-producing regions.* Energy Conversion and Management, 2022. **254**: p. 115245.
37. Ramezani, R., L.D. Felice, and F. Gallucci, *A review of chemical looping reforming technologies for hydrogen production: recent advances and future challenges.* Journal of Physics: Energy, 2023. **5**(2): p. 024010.
38. Ahmadi, P. and E. Kjeang, *Realistic simulation of fuel economy and life cycle metrics for hydrogen fuel cell vehicles.* International Journal of Energy Research, 2017. **41**(5): p. 714-727.
39. Jamesh, M.-I. and X. Sun, *Recent progress on earth abundant electrocatalysts for oxygen evolution reaction (OER) in alkaline medium to achieve efficient water splitting–A review.* Journal of Power Sources, 2018. **400**: p. 31-68.

40. Giordano, L., et al., *pH dependence of OER activity of oxides: Current and future perspectives.* Catalysis Today, 2016. **262**: p. 2-10.
41. Carmo, M., et al., *A comprehensive review on PEM water electrolysis.* International journal of hydrogen energy, 2013. **38**(12): p. 4901-4934.
42. Reier, T., M. Oezaslan, and P. Strasser, *Electrocatalytic oxygen evolution reaction (OER) on Ru, Ir, and Pt catalysts: a comparative study of nanoparticles and bulk materials.* Acs Catalysis, 2012. **2**(8): p. 1765-1772.
43. Leung, D.Y., et al., *Hydrogen production over titania-based photocatalysts.* ChemSusChem, 2010. **3**(6): p. 681-694.
44. Yang, J.-X., et al., *PtO nanodots promoting Ti3C2 MXene in-situ converted Ti3C2/TiO2 composites for photocatalytic hydrogen production.* Chemical Engineering Journal, 2021. **420**: p. 129695.
45. Zhao, H., et al., *Size effect of bifunctional gold in hierarchical titanium oxide-gold-cadmium sulfide with slow photon effect for unprecedented visible-light hydrogen production.* Journal of Colloid and Interface Science, 2021. **604**: p. 131-140.
46. Som, N.N. and P.K. Jha, *Hydrogen evolution reaction of metal di-chalcogenides: ZrS2, ZrSe2 and Janus ZrSSe.* International Journal of Hydrogen Energy, 2020. **45**(44): p. 23920-23927.
47. Kudo, A., H. Kato, and I. Tsuji, *Strategies for the development of visible-light-driven photocatalysts for water splitting.* Chemistry letters, 2004. **33**(12): p. 1534-1539.
48. Navarro Yerga, R.M., et al., *Water Splitting on Semiconductor Catalysts under Visible-Light Irradiation.* ChemSusChem, 2009. **2**(6): p. 471-485.
49. Ran, J., et al., *Earth-abundant cocatalysts for semiconductor-based photocatalytic water splitting.* Chemical Society Reviews, 2014. **43**(22): p. 7787-7812.
50. Shanmugaratnam, S., et al., *Recent Progress and Approaches on Transition Metal Chalcogenides for Hydrogen Production.* Energies, 2021. **14**(24): p. 8265.
51. Marschall, R., *50 Years of Materials Research for Photocatalytic Water Splitting.* European Journal of Inorganic Chemistry, 2021. **2021**(25): p. 2435-2441.
52. Chen, S., T. Takata, and K. Domen, *Particulate photocatalysts for overall water splitting.* Nature Reviews Materials, 2017. **2**(10): p. 17050.
53. Yang, J., et al., *Roles of Cocatalysts in Photocatalysis and Photoelectrocatalysis.* Accounts of Chemical Research, 2013. **46**(8): p. 1900-1909.
54. Yan, H., et al., *Visible-light-driven hydrogen production with extremely high quantum efficiency on Pt–PdS/CdS photocatalyst.* Journal of Catalysis, 2009. **266**(2): p. 165-168.
55. Silva, L.A., et al., *Photocatalytic Hydrogen Production with Visible Light over Pt-Interlinked Hybrid Composites of Cubic-Phase and Hexagonal-Phase CdS.* The Journal of Physical Chemistry C, 2008. **112**(32): p. 12069-12073.
56. Tang, L., et al., *Engineering Noble Metal-like Bi onto Hierarchical SrWO4 for the Enhancement of Photocatalytic Activity.* Catalysts, 2022. **12**(7): p. 787.
57. Huang, Q., et al., *NiCoP modified lead-free double perovskite Cs 2 AgBiBr 6 for efficient photocatalytic hydrogen generation.* New Journal of Chemistry, 2022. **46**(16): p. 7395-7402.
58. Zhang, J., et al., *Strong metal-support interactions induced by an ultrafast laser.* Nature Communications, 2021. **12**(1): p. 6665.
59. Du, H., et al., *Nanoheterostructured photocatalysts for improving photocatalytic hydrogen production.* Chinese Journal of Catalysis, 2017. **38**(8): p. 1295-1306.
60. Yang, S., et al., *A new post-synthetic polymerization strategy makes metal–organic frameworks more stable.* Chemical Science, 2019. **10**(17): p. 4542-4549.
61. Sun, P., et al., *Recent advances in quantum dots photocatalysts.* Chemical Engineering Journal, 2023. **458**: p. 141399.

62. Xue, J., et al., *Fabrication, photoluminescence and applications of quantum dots embedded glass ceramics.* Chemical Engineering Journal, 2020. **383**: p. 123082.
63. Su, H., et al., *Recent advances in quantum dot catalysts for hydrogen evolution: Synthesis, characterization, and photocatalytic application.* Carbon Energy, 2023. **5**(9): p. e280.
64. Abd Rani, U., et al., *A review of carbon quantum dots and their applications in wastewater treatment.* Advances in colloid and interface science, 2020. **278**: p. 102124.
65. Pal, A., F. Arshad, and M.P. Sk, *Emergence of sulfur quantum dots: Unfolding their synthesis, properties, and applications.* Advances in Colloid and Interface Science, 2020. **285**: p. 102274.
66. Yu, S., et al., *Efficient photocatalytic hydrogen evolution with ligand engineered all-inorganic InP and InP/ZnS colloidal quantum dots.* Nature communications, 2018. **9**(1): p. 4009.
67. Li, F., et al., *"Green", gradient multi-shell CuInSe2/(CuInSexS1-x) 5/CuInS2 quantum dots for photo-electrochemical hydrogen generation.* Applied Catalysis B: Environmental, 2021. **280**: p. 119402.
68. Su, H., et al., *Recent advances in quantum dot catalysts for hydrogen evolution: Synthesis, characterization, and photocatalytic application.* Carbon Energy. **n/a**(n/a): p. e280.
69. Jin, L., et al., *Quantum dots-based photoelectrochemical hydrogen evolution from water splitting.* Advanced Energy Materials, 2021. **11**(12): p. 2003233.
70. Wu, H.L., et al., *Semiconductor quantum dots: an emerging candidate for CO2 photoreduction.* Advanced Materials, 2019. **31**(36): p. 1900709.
71. Liu, Q., et al., *Unraveling the roles of hot electrons and cocatalyst toward broad spectrum photocatalytic H2 generation of g-C3N4 nanotube.* Solar RRL, 2021. **5**(6): p. 2000504.
72. Zhang, L., et al., *Construction of a dual-channel mode for wide spectrum-driven photocatalytic H 2 production.* Journal of Materials Chemistry A, 2019. **7**(3): p. 1076-1082.
73. Reddy, N.L., et al., *Multifunctional Cu/Ag quantum dots on TiO2 nanotubes as highly efficient photocatalysts for enhanced solar hydrogen evolution.* Journal of Catalysis, 2017. **350**: p. 226-239.
74. Li, R., X. Wang, and M. Chen, *Non-Noble Metal and Nonmetallic Plasmonic Nanomaterials with Located Surface Plasmon Resonance Effects: Photocatalytic Performance and Applications.* Catalysts, 2023. **13**(6): p. 940.
75. Liang, C., et al., *Construction of 2D heterojunction system with enhanced photocatalytic performance: Plasmonic Bi and reduced graphene oxide co-modified Bi5O7I with high-speed charge transfer channels.* Journal of hazardous materials, 2019. **361**: p. 245-258.
76. Talebi, P., et al., *Unveiling the role of carbonate in nickel-based plasmonic core@ shell hybrid nanostructure for photocatalytic water splitting.* Applied Energy, 2022. **322**: p. 119461.
77. Derikvandi, H., M. Vosough, and A. Nezamzadeh-Ejhieh, *A comprehensive study on the enhanced photocatlytic activity of a double-shell mesoporous plasmonic Cu@ Cu 2 O/SiO 2 as a visible-light driven nanophotocatalyst.* Environmental Science and Pollution Research, 2020. **27**: p. 27582-27597.
78. Yuan, L., et al., *Morphology-dependent reactivity of a plasmonic photocatalyst.* ACS nano, 2020. **14**(9): p. 12054-12063.
79. Mangrulkar, P.A., et al., *Plasmonic nanostructured Zn/ZnO composite enhances carbonic anhydrase driven photocatalytic hydrogen generation.* Journal of CO2 Utilization, 2017. **17**: p. 207-212.
80. Matsko, N., *Formation of normal surface plasmon modes in small sodium nanoparticles.* Physical Chemistry Chemical Physics, 2020. **22**(23): p. 13285-13291.
81. Hopper, E.R., et al., *Opportunities and challenges for alternative nanoplasmonic metals: magnesium and beyond.* The Journal of Physical Chemistry C, 2022. **126**(26): p. 10630-10643.

82. Nan, H., et al., *Strong photoluminescence enhancement of MoS2 through defect engineering and oxygen bonding.* ACS nano, 2014. **8**(6): p. 5738-5745.
83. Hong, W., et al., *NiO Quantum Dot Modified TiO2 toward Robust Hydrogen Production Performance.* ACS Sustainable Chemistry & Engineering, 2018. **6**(1): p. 889-896.
84. Wang, X., T.-T. Li, and Y.-Q. Zheng, *Co3O4 nanosheet arrays treated by defect engineering for enhanced electrocatalytic water oxidation.* International Journal of Hydrogen Energy, 2018. **43**(4): p. 2009-2017.
85. Sun, W., et al., *Recent advances and perspectives in cobalt-based heterogeneous catalysts for photocatalytic water splitting, CO2 reduction, and N2 fixation.* Chinese Journal of Catalysis, 2022. **43**(9): p. 2273-2300.
86. Zhang, S.L., et al., *Metal atom-doped Co3O4 hierarchical nanoplates for electrocatalytic oxygen evolution.* Advanced Materials, 2020. **32**(31): p. 2002235.
87. Guo, W., et al., *Ge-Doped Cobalt Oxide for Electrocatalytic and Photocatalytic Water Splitting.* ACS Catalysis, 2022. **12**(19): p. 12000-12013.
88. Menezes, P.W., et al., *Cobalt–manganese-based spinels as multifunctional materials that unify catalytic water oxidation and oxygen reduction reactions.* ChemSusChem, 2015. **8**(1): p. 164-171.
89. Tien, T.-M., Y. Chuang, and E.L. Chen, *Z-scheme driven of MoS2/Co3O4 nano-heterojunction for efficient photocatalysis hydrogen evolution and Rhodamine B degradation.* Journal of Photochemistry and Photobiology A: Chemistry, 2023. **444**: p. 114986.
90. Chen, W., et al., *Non-noble metal Co as active sites on TiO2 nanorod for promoting photocatalytic H2 production.* Materials Research Bulletin, 2019. **116**: p. 16-21.
91. Xu, H., et al., *In-situ synthesis of novel plate-like Co(OH)2 co-catalyst decorated TiO2 nanosheets with efficient photocatalytic H2 evolution activity.* International Journal of Hydrogen Energy, 2017. **42**(36): p. 22877-22886.
92. Liu, J., et al., *Highly Dispersed NiCo2O4 Nanodots Decorated Three-Dimensional g-C3N4 for Enhanced Photocatalytic H2 Generation.* ACS Sustainable Chemistry & Engineering, 2019. **7**(14): p. 12428-12438.
93. Barrios, C.E., et al., *Photocatalytic hydrogen production over titania modified by gold – Metal (palladium, nickel and cobalt) catalysts.* International Journal of Hydrogen Energy, 2016. **41**(48): p. 23287-23300.
94. Takashima, T., T. Sano, and H. Irie, *Cocatalyst modification of niobium-substituted silver tantalate photocatalyst for enhanced solar water-splitting activity.* International Journal of Hydrogen Energy, 2019. **44**(42): p. 23600-23609.
95. Sheng, H., et al., *Strong synergy between gold nanoparticles and cobalt porphyrin induces highly efficient photocatalytic hydrogen evolution.* Nature Communications, 2023. **14**(1): p. 1528.
96. Li, S., et al., *Novel photocatalyst incorporating Ni-Co layered double hydroxides with P-doped CdS for enhancing photocatalytic activity towards hydrogen evolution.* Applied Catalysis B: Environmental, 2019. **254**: p. 145-155.
97. An, H., et al., *Increased Active Sites by in Situ Growth of CoP Quantum Dots on CdS/rGO To Achieve Efficient Photocatalytic H2 Production.* ACS Applied Energy Materials, 2019. **2**(6): p. 4195-4204.
98. Huo, J. and H. Zeng, *Silver nanoparticles-sensitized cobalt complex for highly-efficient photocatalytic activity.* Applied Catalysis B: Environmental, 2016. **199**: p. 342-349.
99. Wu, M., et al., *Optimization of the facet structure of cobalt oxide catalysts for enhanced hydrogen evolution reaction.* Catalysis Science & Technology, 2020. **10**(4): p. 1040-1047.
100. Qi, K., et al., *Photocatalytic H2 generation via CoP quantum-dot-modified g-C3N4 synthesized by electroless plating.* Chinese Journal of Catalysis, 2020. **41**(1): p. 114-121.

101. Luo, B., et al., *Towards the prominent cocatalytic effect of ultra-small CoP particles anchored on g-C3N4 nanosheets for visible light driven photocatalytic H2 production.* Applied Catalysis B: Environmental, 2019. **256**: p. 117819.
102. Xue, W., et al., *Highly dispersed copper cobalt oxide nanoclusters decorated carbon nitride with efficient heterogeneous interfaces for enhanced H2 evolution.* Journal of Colloid and Interface Science, 2020. **576**: p. 203-216.
103. Ma, B., et al., *Bimetal–Organic-Framework-Derived Nanohybrids Cu0.9Co2.1S4@MoS2 for High-Performance Visible-Light-Catalytic Hydrogen Evolution Reaction.* ACS Applied Energy Materials, 2019. **2**(2): p. 1134-1148.
104. Li, H., P. Deng, and Y. Hou, *Cobalt disulfide/graphitic carbon nitride as an efficient photocatalyst for hydrogen evolution reaction under visible light irradiation.* Materials Letters, 2018. **229**: p. 217-220.
105. Bellamkonda, S., et al., *Rational design of plasmonic Ag@CoFe2O4/g-C3N4 p-n heterojunction photocatalysts for efficient overall water splitting.* International Journal of Hydrogen Energy, 2022. **47**(43): p. 18708-18724.
106. Li, C., et al., *In situ synthesis of Co 2 P-decorated red phosphorus nanosheets for efficient photocatalytic H 2 evolution.* Catalysis Science & Technology, 2020. **10**(7): p. 2221-2230.
107. Liu, Y., et al., *Construction of CdS/CoOx core-shell nanorods for efficient photocatalytic H2 evolution.* Applied Catalysis B: Environmental, 2018. **234**: p. 109-116.
108. Chu, J., et al., *Ultrafine CoO nanoparticles as an efficient cocatalyst for enhanced photocatalytic hydrogen evolution.* Nanoscale, 2019. **11**(33): p. 15633-15640.
109. Zhao, H., et al., *A homojunction–heterojunction–homojunction scaffold boosts photocatalytic H 2 evolution over Cd 0.5 Zn 0.5 S/CoO hybrids.* Journal of Materials Chemistry A, 2020. **8**(4): p. 1955-1965.
110. Feng, H.-Q., et al., *An efficient ternary Mn0.2Cd0.8S/MoS2/Co3O4 heterojunction for visible-light-driven photocatalytic H2 evolution.* International Journal of Hydrogen Energy, 2020. **45**(18): p. 10764-10774.
111. Liu, H., et al., *A sea-urchin-structured NiCo 2 O 4 decorated Mn 0.05 Cd 0.95 S p–n heterojunction for enhanced photocatalytic hydrogen evolution.* Dalton Transactions, 2020. **49**(38): p. 13393-13405.
112. Wang, Y., et al., *Effective interface contact on the hierarchical 1D/2D CoO/NiCo-LDH heterojunction for boosting photocatalytic hydrogen evolution.* Applied Surface Science, 2021. **549**: p. 149108.
113. Qiu, B., et al., *Efficient Solar Light Harvesting CdS/Co9S8 Hollow Cubes for Z-Scheme Photocatalytic Water Splitting.* Angewandte Chemie International Edition, 2017. **56**(10): p. 2684-2688.
114. Tien, T.-M. and E.L. Chen, *S-Scheme System of MoS2/Co3O4 Nanocomposites for Enhanced Photocatalytic Hydrogen Evolution and Methyl Violet Dye Removal under Visible Light Irradiation.* Coatings, 2023. **13**(1): p. 80.
115. Jia, X., et al., *Improvement of photocatalytic hydrogen generation of leaves-like CdS microcrystals with a surface decorated by dealloyed Pt-Cox nanoparticles.* Solar Energy, 2020. **206**: p. 8-17.
116. Zhang, Y. and W.-D. Zhang, *Ternary catalysts based on amino-functionalized carbon quantum dots, graphitic carbon nitride nanosheets and cobalt complex for efficient H2 evolution under visible light irradiation.* Carbon, 2019. **145**: p. 488-500.
117. Li, N., et al., *Efficient, Full Spectrum-Driven H2 Evolution Z-Scheme Co2P/CdS Photocatalysts with Co–S Bonds.* ACS Applied Materials & Interfaces, 2019. **11**(25): p. 22297-22306.

118. Li, C., et al., *Mesoporous 3D/2D NiCoP/g-C3N4 Heterostructure with Dual Co–N and Ni–N Bonding States for Boosting Photocatalytic H2 Production Activity and Stability.* ACS Sustainable Chemistry & Engineering, 2020. **8**(34): p. 12934-12943.
119. Sun, X. and H. Du, *Acid-Exfoliated Metallic Co0.85Se Nanosheets as Cocatalyst on Cd0.5Zn0.5S for Photocatalytic Hydrogen Evolution under Visible-Light Irradiation.* ACS Sustainable Chemistry & Engineering, 2019. **7**(19): p. 16320-16328.
120. Takashima, T., T. Sano, and H. Irie, *Improvement of The Photocatalytic Water Splitting Activity of Silver Tantalate by Photodeposited Platinum and Cobalt-Oxide Nanoclusters.* Electrochemistry, 2016. **84**(10): p. 784-788.
121. Chen, Z., et al., *Ternary Co3O4/CdS/SrTiO3 core-shell pn junctions toward enhanced photocatalytic hydrogen production activity.* Journal of Environmental Chemical Engineering, 2021. **9**(1): p. 104895.
122. Bai, Y., et al., *Photocatalytic Overall Water Splitting Under Visible Light Enabled by a Particulate Conjugated Polymer Loaded with Palladium and Iridium**.* Angewandte Chemie International Edition, 2022. **61**(26): p. e202201299.
123. Liu, Y., et al., *Nanoplasmonic zirconium nitride photocatalyst for direct overall water splitting.* Chinese Chemical Letters, 2022. **33**(3): p. 1271-1274.
124. Zhang, P., et al., *Design of plasmonic CuCo bimetal as a nonsemiconductor photocatalyst for synchronized hydrogen evolution and storage.* Applied Catalysis B: Environmental, 2019. **242**: p. 389-396.
125. Zhang, P., H. Liu, and X. Li, *Plasmon-driven engineering in bimetallic CuCo combined with reduced graphene oxide for photocatalytic overall water splitting.* Applied Surface Science, 2021. **559**: p. 149865.
126. Dai, Z., et al., *Surface structure of bulk 2H-MoS2 (0001) and exfoliated suspended monolayer MoS2: A selected area low energy electron diffraction study.* Surface Science, 2017. **660**: p. 16-21.
127. Li, X. and H. Zhu, *Two-dimensional MoS2: Properties, preparation, and applications.* Journal of Materiomics, 2015. **1**(1): p. 33-44.
128. Shang, C., et al., *Superconductivity in the metastable $1{T}^{\ensuremath{'}}$ and $1{T}^{\ensuremath{'}\ensuremath{''}}$ phases of $\mathrm{Mo}{\mathrm{S}}_{2}$ crystals.* Physical Review B, 2018. **98**(18): p. 184513.
129. Tang, Q. and D.-e. Jiang, *Mechanism of Hydrogen Evolution Reaction on 1T-MoS2 from First Principles.* ACS Catalysis, 2016. **6**(8): p. 4953-4961.
130. Voiry, D., et al., *Conducting MoS2 nanosheets as catalysts for hydrogen evolution reaction.* Nano letters, 2013. **13**(12): p. 6222-6227.
131. Benson, J., et al., *Electrocatalytic hydrogen evolution reaction on edges of a few layer molybdenum disulfide nanodots.* ACS applied materials & interfaces, 2015. **7**(25): p. 14113-14122.
132. Mohammad-Andashti, P., et al., *Rapid and green synthesis of highly luminescent MoS2 quantum dots via microwave exfoliation of MoS2 powder and its application as a fluorescence probe for cortisol detection in human saliva.* Colloids and Surfaces A: Physicochemical and Engineering Aspects, 2022. **647**: p. 129048.
133. Zhu, S., et al., *Photoluminescence mechanism in graphene quantum dots: Quantum confinement effect and surface/edge state.* Nano Today, 2017. **13**: p. 10-14.
134. Presolski, S. and M. Pumera, *Covalent functionalization of MoS2.* Materials Today, 2016. **19**(3): p. 140-145.
135. Qiao, W., et al., *Monolayer MoS 2 quantum dots as catalysts for efficient hydrogen evolution.* RSC advances, 2015. **5**(118): p. 97696-97701.

136. Ranjit, K.T. and B. Viswanathan, *Synthesis, characterization and photocatalytic properties of iron-doped TiO2 catalysts.* Journal of Photochemistry and Photobiology A: Chemistry, 1997. **108**(1): p. 79-84.
137. Low, J., et al., *Heterojunction Photocatalysts.* Advanced Materials, 2017. **29**(20): p. 1601694.
138. Maeda, K., *Z-Scheme Water Splitting Using Two Different Semiconductor Photocatalysts.* ACS Catalysis, 2013. **3**(7): p. 1486-1503.
139. Yu, J., et al., *Enhanced photocatalytic performance of direct Z-scheme gC 3 N 4–TiO 2 photocatalysts for the decomposition of formaldehyde in air.* Physical Chemistry Chemical Physics, 2013. **15**(39): p. 16883-16890.
140. Chen, S., et al., *Preparation and characterization of direct Z-scheme photocatalyst Bi2O3/NaNbO3 and its reaction mechanism.* Applied Surface Science, 2014. **292**: p. 357-366.
141. Ye, L., et al., *Solid-state Z-scheme assisted hydrated tungsten trioxide/ZnIn2S4 photocatalyst for efficient photocatalytic H2 production.* Materials Futures, 2022. **1**(3): p. 035103.
142. Yang, G. and S.-J. Park, *Conventional and Microwave Hydrothermal Synthesis and Application of Functional Materials: A Review.* Materials, 2019. **12**(7): p. 1177.
143. Sun, J., W. Wang, and Q. Yue, *Review on microwave-matter interaction fundamentals and efficient microwave-associated heating strategies.* Materials, 2016. **9**(4): p. 231.
144. Motshekga, S.C., et al., *Recent trends in the microwave-assisted synthesis of metal oxide nanoparticles supported on carbon nanotubes and their applications.* Journal of Nanomaterials, 2012. **2012**: p. 51-51.
145. Haque, K.E., *Microwave energy for mineral treatment processes—a brief review.* International journal of mineral processing, 1999. **57**(1): p. 1-24.
146. Wilson, G.J., et al., *Efficient microwave hydrothermal preparation of nanocrystalline anatase TiO 2 colloids.* Journal of Materials Chemistry, 2002. **12**(6): p. 1787-1791.
147. Yao, K., et al., *Comparative study of CuO crystals on the cellulose substrate by the microwave-assisted hydrothermal method and hydrothermal method.* Materials & Design, 2016. **90**: p. 129-136.
148. Huang, H., et al., *Rapid and energy-efficient microwave pyrolysis for high-yield production of highly-active bifunctional electrocatalysts for water splitting.* Energy & Environmental Science, 2020. **13**(2): p. 545-553.
149. Maeda, K. and K. Domen, *Photocatalytic Water Splitting: Recent Progress and Future Challenges.* The Journal of Physical Chemistry Letters, 2010. **1**(18): p. 2655-2661.
150. Li, Q., X. Li, and J. Yu, *Chapter 10 - Surface and interface modification strategies of CdS-based photocatalysts*, in *Interface Science and Technology*, J. Yu, M. Jaroniec, and C. Jiang, Editors. 2020, Elsevier. p. 313-348.
151. Tsuji, I., et al., *Photocatalytic H2 evolution reaction from aqueous solutions over band structure-controlled (AgIn) x Zn2 (1-x) S2 solid solution photocatalysts with visible-light response and their surface nanostructures.* Journal of the American Chemical Society, 2004. **126**(41): p. 13406-13413.
152. Yu, T., et al., *Constructing Ni2P/Cd0.5Zn0.5S/Co3O4 ternary heterostructure for high-efficient photocatalytic hydrogen production.* Applied surface science, 2020. **509**: p. 145371.
153. Megía, P.J., et al., *Hydrogen Production Technologies: From Fossil Fuels toward Renewable Sources. A Mini Review.* Energy & Fuels, 2021. **35**(20): p. 16403-16415.
154. Arora, I., et al., *Advances in the strategies for enhancing the photocatalytic activity of TiO2: Conversion from UV-light active to visible-light active photocatalyst.* Inorganic Chemistry Communications, 2022. **143**: p. 109700.
155. Moridon, S.N.F., et al., *Cobalt oxide as photocatalyst for water splitting: Temperature-dependent phase structures.* International journal of hydrogen energy, 2019. **44**(47): p. 25495-25504.

156. Mohammadi, M.R., et al., *Exploring the limits of self-repair in cobalt oxide films for electrocatalytic water oxidation.* ACS Catalysis, 2020. **10**(14): p. 7990-7999.
157. Duo, F., et al., *High performance visible light response 0D/2D MoS2QDs/BiOCl photocatalyst with synergetic effects of up-conversion and direct Z-scheme heterojunction.* Journal of Alloys and Compounds, 2023. **962**: p. 171161.
158. Liu, Z., J. Wu, and J. Zhang, *Quantum dots and plasmonic Ag decorated WO3 nanorod photoanodes with enhanced photoelectrochemical performances.* International Journal of Hydrogen Energy, 2016. **41**(45): p. 20529-20535.
159. Sun, J., et al., *Synthesis of MoS2 quantum dots cocatalysts and their efficient photocatalytic performance for hydrogen evolution.* Chemical Engineering Journal, 2018. **332**: p. 449-455.
160. Yang, L., S. Guo, and X. Li, *Au nanoparticles@MoS2 core-shell structures with moderate MoS2 coverage for efficient photocatalytic water splitting.* Journal of Alloys and Compounds, 2017. **706**: p. 82-88.
161. Sriram, P., et al., *Hybridizing Strong Quadrupole Gap Plasmons Using Optimized Nanoantennas with Bilayer MoS2 for Excellent Photo-Electrochemical Hydrogen Evolution.* Advanced energy materials, 2018. **8**(29): p. n/a.
162. Chen, K., et al., *Integrating metallic nanoparticles of Au and Pt with MoS 2–CdS hybrids for high-efficient photocatalytic hydrogen generation via plasmon-induced electron and energy transfer.* RSC advances, 2017. **7**(42): p. 26097-26103.
163. Yaning, Z., et al., *Microwave-Assisted Pyrolysis of Biomass for Bio-Oil Production*, in *Pyrolysis*, S. Mohamed, Editor. 2017, IntechOpen: Rijeka. p. Ch. 6.
164. D E Clark, a. and W.H. Sutton, *Microwave Processing of Materials.* Annual Review of Materials Science, 1996. **26**(1): p. 299-331.
165. Kuznetsov, M.V., Y.G. Morozov, and O.V. Belousova, *Synthesis of copper ferrite nanoparticles.* Inorganic Materials, 2013. **49**(6): p. 606-615.
166. Yakovleva, I.S., et al., *Microwave synthesis of LaBO3 (B = Co, Fe) perovskites using graphite and citric acid additions.* Kinetics and Catalysis, 2014. **55**(5): p. 630-638.
167. Saremi-Yarahmadi, S., W. Whittow, and B. Vaidhyanathan, *Electromagnetic simulation studies of microwave assisted heating for the processing of nanostructured iron oxide for solar driven water splitting.* Applied Surface Science, 2013. **275**.
168. Saremi-Yarahmadi, S., W. Whittow, and B. Vaidhyanathan, *Electromagnetic simulation studies of microwave assisted heating for the processing of nanostructured iron oxide for solar driven water splitting.* Applied surface science, 2013. **275**: p. 65-70.
169. Mahmoudi, M., et al., *Optimal Design and Characterization of Superparamagnetic Iron Oxide Nanoparticles Coated with Polyvinyl Alcohol for Targeted Delivery and Imaging.* The Journal of Physical Chemistry B, 2008. **112**(46): p. 14470-14481.
170. Anbarasu, M., et al., *Synthesis and characterization of polyethylene glycol (PEG) coated Fe3O4 nanoparticles by chemical co-precipitation method for biomedical applications.* Spectrochimica Acta Part A: Molecular and Biomolecular Spectroscopy, 2015. **135**: p. 536-539.
171. Afzal, H.M., et al., *Influence of microwave irradiation on thermal properties of PVA and PVA/graphene nanocomposites.* Journal of Thermal Analysis and Calorimetry, 2020. **139**(1): p. 353-365.
172. Dai, M., et al., *Ordered Mesoporous Carbon Composite Films Containing Cobalt Oxide and Vanadia for Electrochemical Applications.* Chemistry of Materials, 2011. **23**(11): p. 2869-2878.
173. Ai, L.-H. and J. Jiang, *Rapid synthesis of nanocrystalline Co3O4 by a microwave-assisted combustion method.* Powder Technology, 2009. **195**: p. 11-14.

174. Kundu, S. and M. Jayachandran, *Shape-selective synthesis of non-micellar cobalt oxide (CoO) nanomaterials by microwave irradiations.* Journal of Nanoparticle Research, 2013. **15**(4): p. 1543.
175. Gang, R., et al., *Fabrication of MoS(2) QDs/ZnO nanosheet 0D/2D heterojunction photocatalysts for organic dyes and gaseous heavy metal removal.* J Colloid Interface Sci, 2020. **579**: p. 853-861.
176. Mukherjee, S., et al., *Novel Colloidal MoS2 Quantum Dot Heterojunctions on Silicon Platforms for Multifunctional Optoelectronic Devices.* Scientific Reports, 2016. **6**(1): p. 29016.
177. Gopalakrishnan, D., D. Damien, and M.M. Shaijumon, *MoS2 quantum dot-interspersed exfoliated MoS2 nanosheets.* ACS nano, 2014. **8**(5): p. 5297-5303.
178. Ali, L., et al., *Ion-Intercalation Assisted Solvothermal Synthesis and Optical Characterization of MoS 2 Quantum Dots.* Journal of the Korean Physical Society, 2019. **74**: p. 191-195.
179. Guo, M., et al., *WS2 quantum dots/MoS2@WO3-x core-shell hierarchical dual Z-scheme tandem heterojunctions with wide-spectrum response and enhanced photocatalytic performance.* Applied Catalysis B: Environmental, 2019. **257**: p. 117913.
180. Zhang, Y., et al., *Synergistic effect of reduced graphene oxide and near-infrared light on MoS2-mediated electrocatalytic hydrogen evolution.* Chemical Engineering Journal, 2021. **418**: p. 129343.
181. Jiao, Y., et al., *A novel MoS2 quantum dots (QDs) decorated Z-scheme g-C3N4 nanosheet/N-doped carbon dots heterostructure photocatalyst for photocatalytic hydrogen evolution.* Applied Catalysis B: Environmental, 2019. **247**: p. 124-132.
182. Li, Y., et al., *Simulation-guided synthesis of graphitic carbon nitride beads with 3D interconnected and continuous meso/macropore channels for enhanced light absorption and photocatalytic performance.* Journal of Materials Chemistry A, 2017. **5**(40): p. 21300-21312.
183. Ilyas, M. and M. Saeed, *Oxidation of Benzyl Alcohol in Liquid Phase Catalyzed by Cobalt Oxide.* International Journal of Chemical Reactor Engineering, 2010. **8**(1).
184. Osazuwa, O.U. and C.K. Cheng, *Catalytic conversion of methane and carbon dioxide (greenhouse gases) into syngas over samarium-cobalt-trioxides perovskite catalyst.* Journal of Cleaner Production, 2017. **148**: p. 202-211.
185. Abu-Zied, B.M., et al., *Effect of microwave power on the thermal genesis of Co3O4 nanoparticles from cobalt oxalate micro-rods.* Applied Surface Science, 2015. **351**: p. 600-609.
186. Pourshahbazi, H., et al., *Novel oxygen scavenger screw-cap for shelf-life improvement in virgin olive oil packaging during storage.* Journal of Food Measurement and Characterization, 2022. **16**(4): p. 2831-2837.
187. Tang, C.-M., Y.-H. Tian, and S.-H. Hsu, *Poly(vinyl alcohol) Nanocomposites Reinforced with Bamboo Charcoal Nanoparticles: Mineralization Behavior and Characterization.* Materials, 2015. **8**(8): p. 4895-4911.
188. Yu, Y.-H., et al., *Preparation and properties of poly(vinyl alcohol)–clay nanocomposite materials.* Polymer, 2003. **44**(12): p. 3553-3560.
189. Hameed, R.A., A.-A.H. Abu-Nawwas, and H. Shehata, *Nano-composite as corrosion inhibitors for steel alloys in different corrosive media.* Advances in Applied Science Research, 2013. **4**(3): p. 126-129.
190. Li, B., et al., *Preparation of Monolayer MoS2 Quantum Dots using Temporally Shaped Femtosecond Laser Ablation of Bulk MoS2 Targets in Water.* Scientific Reports, 2017. **7**(1): p. 11182.
191. Qin, M., et al., *Regulating the Crystallization Kinetics and Lattice Strain of Lead-Free Perovskites with Perovskite Quantum Dots.* ACS Energy Letters, 2022. **7**(10): p. 3251-3259.
192. Gole, J.L., et al., *Study of concentration-dependent cobalt ion doping of TiO 2 and TiO 2− x N x at the nanoscale.* Nanoscale, 2010. **2**(7): p. 1134-1140.

193. Pylypenko, S., et al., *Non-platinum oxygen reduction electrocatalysts based on pyrolyzed transition metal macrocycles.* Electrochimica Acta, 2008. **53**(27): p. 7875-7883.
194. Muralee Gopi, C.V.V., et al., *One-pot synthesis of copper oxide–cobalt oxide core–shell nanocactus-like heterostructures as binder-free electrode materials for high-rate hybrid supercapacitors.* Materials Today Energy, 2019. **14**: p. 100358.
195. Leng, X., et al., *In situ prepared reduced graphene oxide/CoO nanowires mutually-supporting porous structure with enhanced lithium storage performance.* Electrochimica Acta, 2016. **190**: p. 276-284.
196. Pietron, J.J., et al., *Electrocatalysis at Co–poly(difluoropyrrole) electrodeposited on Vulcan carbon supports: demonstration of halogenated polypyrrole as an electrocatalytic material.* Journal of Materials Chemistry, 2011. **21**(21): p. 7668-7677.
197. Musat, V., et al., *Sol–gel cobalt oxide–silica nanocomposite thin films for gas sensing applications.* Thin Solid Films, 2008. **516**(7): p. 1499-1502.
198. Li, S., et al., *Carbon-Coated Co(3+)-Rich Cobalt Selenide Derived from ZIF-67 for Efficient Electrochemical Water Oxidation.* ACS Appl Mater Interfaces, 2016. **8**(32): p. 20534-9.
199. Tian, Y., et al., *Hollow cobalt oxide nanoparticles embedded in nitrogen-doped carbon nanosheets as an efficient bifunctional catalyst for Zn–air battery.* Journal of Energy Chemistry, 2019. **33**: p. 59-66.
200. Ghosh, S., et al., *Nickel–cobalt oxalate as an efficient non-precious electrocatalyst for an improved alkaline oxygen evolution reaction.* Nanoscale Advances, 2021. **3**(13): p. 3770-3779.
201. Artyushkova, K., et al., *Predictive Modeling of Electrocatalyst Structure Based on Structure-to-Property Correlations of X-ray Photoelectron Spectroscopic and Electrochemical Measurements.* Langmuir, 2008. **24**(16): p. 9082-9088.
202. Hussain, S., et al., *Novel gravel-like NiMoO4 nanoparticles on carbon cloth for outstanding supercapacitor applications.* Ceramics International, 2020. **46**(5): p. 6406-6412.
203. Yi, T.-F., et al., *Porous spherical NiO@ NiMoO4@ PPy nanoarchitectures as advanced electrochemical pseudocapacitor materials.* Science Bulletin, 2020. **65**(7): p. 546-556.
204. Mawlong, L.P.L., A. Bora, and P.K. Giri, *Coupled Charge Transfer Dynamics and Photoluminescence Quenching in Monolayer MoS2 Decorated with WS2 Quantum Dots.* Scientific Reports, 2019. **9**(1): p. 19414.
205. Guo, J., et al., *The Application of Nano-MoS2 Quantum Dots as Liquid Lubricant Additive for Tribological Behavior Improvement.* Nanomaterials, 2020. **10**(2): p. 200.
206. Merck Darmstadt, G.a.o.i.a.A.R.R. *IR Spectrum Table & Chart*. 2023 [cited 2023 14 September]; Available from: https://www.sigmaaldrich.com/AU/en/technical-documents/technical-article/analytical-chemistry/photometry-and-reflectometry/ir-spectrum-table.
207. Salavati-Niasari, M., N. Mir, and F. Davar, *Synthesis and characterization of Co3O4 nanorods by thermal decomposition of cobalt oxalate.* Journal of Physics and Chemistry of Solids, 2009. **70**(5): p. 847-852.
208. Herrero, M., et al., *Nanosize cobalt oxide-containing catalysts obtained through microwave-assisted methods.* Catalysis Today, 2007. **128**(3): p. 129-137.
209. Zhang, F., et al., *Facile growth of mesoporous Co3O4 nanowire arrays on Ni foam for high performance electrochemical capacitors.* Journal of Power Sources, 2012. **203**: p. 250-256.
210. Yimlamai, I., et al., *Electrical conductivity response and sensitivity of ZSM-5, Y, and mordenite zeolites towards ethanol vapor.* Ionics, 2011. **17**(7): p. 607-615.
211. Jincy, C.S. and P. Meena, *Synthesis, Characterization, and NH3 Gas Sensing Application of Zn doped Cobalt Oxide Nanoparticles.* Inorganic Chemistry Communications, 2020. **120**: p. 108145.

212. Zhang, X., et al., *Anchoring Metallic MoS2 Quantum Dots over MWCNTs for Highly Sensitive Detection of Postharvest Fungicide in Traditional Chinese Medicines.* ACS Omega, 2021. **6**(2): p. 1488-1496.
213. Fei, L., et al., *Direct TEM observations of growth mechanisms of two-dimensional MoS2 flakes.* Nature Communications, 2016. **7**(1): p. 12206.
214. Volkovich, V.A., et al., *Electrode and Redox Potentials of Molybdenum and Stability of Molybdenum Chloro-Species in Alkali Chloride Melts.* Journal of The Electrochemical Society, 2017. **164**(8): p. H5336.
215. Hao, X., et al., *Peculiar synergetic effect of MoS2 quantum dots and graphene on Metal-Organic Frameworks for photocatalytic hydrogen evolution.* Applied Catalysis B: Environmental, 2017. **210**: p. 45-56.
216. Ali, L., et al., *Exfoliation of MoS2 Quantum Dots: Recent Progress and Challenges.* Nanomaterials, 2022. **12**(19): p. 3465.
217. Faid, A.Y. and H. Ismail, *Ternary mixed nickel cobalt iron oxide nanorods as a high-performance asymmetric supercapacitor electrode.* Materials Today Energy, 2019. **13**: p. 285-292.
218. Kamar, E. and S. El-Dek. *Facile sonochemical synthesis of artichoke-like Co3O4-graphene nanocomposites*. in *IOP Conference Series: Materials Science and Engineering*. 2018. IOP Publishing.
219. Nare, R.K., et al., *Sonication-supported synthesis of cobalt oxide assembled on an N-MWCNT composite for electrochemical supercapacitors via three-electrode configuration.* Scientific Reports, 2022. **12**(1): p. 1998.
220. Jadhav, C.H., et al., *Electrochemical supercapacitive performance study of spray pyrolyzed cobalt oxide film.* Materials Today: Proceedings, 2021. **43**: p. 2742-2746.
221. Zhang, D., et al., *Fabrication of platinum-loaded cobalt oxide/molybdenum disulfide nanocomposite toward methane gas sensing at low temperature.* Sensors and Actuators B: Chemical, 2017. **252**: p. 624-632.
222. Yu, Z.Y., et al., *Clean and affordable hydrogen fuel from alkaline water splitting: past, recent progress, and future prospects.* Advanced Materials, 2021. **33**(31): p. 2007100.
223. Hasan Khan, M., *Tunable Photocatalytic Properties of Planar GaN/GeC Hetero-Bilayer: Production of H_2 Fuel.* IEEE Access, 2020. **8**.
224. Linsebigler, A.L., G. Lu, and J.T. Yates, Jr., *Photocatalysis on TiO2 Surfaces: Principles, Mechanisms, and Selected Results.* Chemical Reviews, 1995. **95**(3): p. 735-758.
225. Roger, I., M.A. Shipman, and M.D. Symes, *Earth-abundant catalysts for electrochemical and photoelectrochemical water splitting.* Nature Reviews Chemistry, 2017. **1**(1): p. 0003.
226. Arora, I., et al., *Advances in the strategies for enhancing the photocatalytic activity of TiO2: Conversion from UV-light active to visible-light active photocatalyst.* Inorganic Chemistry Communications, 2022. **143**: p. 109700.
227. Shi, Z., et al., *Co3O4/TiO2 Nanocomposite Formation Leads to Improvement in Ultraviolet–Visible-Infrared-Driven Thermocatalytic Activity Due to Photoactivation and Photocatalysis–Thermocatalysis Synergetic Effect.* ACS Sustainable Chemistry & Engineering, 2018. **6**(12): p. 16503-16514.
228. Moridon, S.N.F., et al., *Synthesis of Cobalt Oxide on FTO by Hydrothermal Method for Photoelectrochemical Water Splitting Application.* Applied Sciences, 2021. **11**(7): p. 3031.
229. Shao, H., et al., *Synergetic activation of peroxymonosulfate by Co3O4 modified g-C3N4 for enhanced degradation of diclofenac sodium under visible light irradiation.* Applied Catalysis B: Environmental, 2017. **218**: p. 810-818.
230. Wang, Y., et al., *Photochemical degradation of phenol solutions on Co3O4 nanorods with sulfate radicals.* Catalysis Today, 2015. **258**: p. 576-584.

231. Zhuang, L., et al., *Ultrathin Iron-Cobalt Oxide Nanosheets with Abundant Oxygen Vacancies for the Oxygen Evolution Reaction.* Advanced Materials, 2017. **29**(17): p. 1606793.
232. Vladimirova, S., et al., *Co_3O_4 as p-Type Material for CO Sensing in Humid Air.* Sensors (Basel), 2017. **17**(10).
233. Grushevskaya, S., I. Belyanskaya, and O. Kozaderov, *Approaches for Modifying Oxide-Semiconductor Materials to Increase the Efficiency of Photocatalytic Water Splitting.* Materials, 2022. **15**(14): p. 4915.
234. Rakibuddin, M., M.A. Shinde, and H. Kim, *Facile sol–gel fabrication of MoS2 bulk, flake and quantum dot for electrochromic device and their enhanced performance with WO3.* Electrochimica Acta, 2020. **349**: p. 136403.
235. Bie, C., L. Wang, and J. Yu, *Challenges for photocatalytic overall water splitting.* Chem, 2022. **8**(6): p. 1567-1574.
236. Kumaravel, V., et al., *Photocatalytic Hydrogen Production: Role of Sacrificial Reagents on the Activity of Oxide, Carbon, and Sulfide Catalysts.* Catalysts, 2019. **9**(3): p. 276.
237. Tran, V.A., et al., *Metal-organic-framework-derived metals and metal compounds as electrocatalysts for oxygen evolution reaction: A review.* International Journal of Hydrogen Energy, 2022. **47**(45): p. 19590-19608.
238. Huang, H., et al., *Visible–Light–Driven Photocatalytic H2 Evolution over CdZnS Nanocrystal Solid Solutions: Interplay of Twin Structures, Sulfur Vacancies and Sacrificial Agents.* Journal of Materials Chemistry A, 2020. **8**.
239. Abu-Zied, B., et al., *Effect of microwave power on the thermal genesis of Co3O4 nanoparticles from cobalt oxalate micro-rods.* Applied Surface Science, 2015. **351**: p. 600-609.
240. Pourshahbazi, H., et al., *Novel oxygen scavenger screw-cap for shelf-life improvement in virgin olive oil packaging during storage.* Journal of Food Measurement and Characterization, 2022. **16**: p. 1-7.
241. Choudhury, B. and A. Choudhury, *Dopant induced changes in structural and optical properties of Cr3+ doped TiO2 nanoparticles.* Materials Chemistry and Physics, 2012. **132**(2): p. 1112-1118.
242. Ikram, M., et al., *The enhanced photocatalytic performance and first-principles computational insights of Ba doping-dependent TiO 2 quantum dots.* Nanoscale Advances, 2022. **4**(18): p. 3996-4008.
243. Wang, C., et al., *The rapid photoresponsive bacteria-killing of Cu-doped MoS 2.* 2020. **8**(15): p. 4216-4224.
244. Sun, H., et al., *Interfacial energy band engineered CsPbBr3/NiFe-LDH heterostructure catalysts with tunable visible light driven photocatalytic CO2 reduction capability.* Catalysis Science & Technology, 2023. **13**(4): p. 1154-1163.
245. Bingwa, N., et al., *Effect of alkali and alkaline earth metal dopants on catalytic activity of mesoporous cobalt oxide evaluated using a model reaction.* Applied Catalysis A: General, 2018. **555**: p. 189-195.
246. Zhang, R., et al., *Electrochemical Activation of Atomic Layer-Deposited Cobalt Phosphate Electrocatalysts for Water Oxidation.* ACS Catalysis, 2021. **11**(5): p. 2774-2785.
247. Kokulnathan, T., et al., *Construction of nickel cobalt-layered double hydroxide/functionalized–halloysite nanotubes composite for electrochemical detection of organophosphate insecticide.* Chemical Engineering Journal, 2022. **433**: p. 133639.
248. Li, S., et al., *Carbon-Coated Co3+-Rich Cobalt Selenide Derived from ZIF-67 for Efficient Electrochemical Water Oxidation.* ACS Applied Materials & Interfaces, 2016. **8**(32): p. 20534-20539.

249. Wang, X., et al., *Atomic-scale insights into surface lattice oxygen activation at the spinel/perovskite interface of Co3O4/La0. 3Sr0. 7CoO3.* Angewandte Chemie International Edition, 2019. **58**(34): p. 11720-11725.
250. Goldwasser, M.R., et al., *Combined methane reforming in presence of CO2 and O2 over LaFe1−xCoxO3 mixed-oxide perovskites as catalysts precursors.* Catalysis Today, 2005. **107-108**: p. 106-113.
251. Liu, Z., et al., *Optimal geometrical configuration of cobalt cations in spinel oxides to promote oxygen evolution reaction.* Angewandte Chemie, 2020. **132**(12): p. 4766-4772.
252. Feng, Y., et al., *3D 1T-MoS2/CoS2 Heterostructure via Interface Engineering for Ultrafast Hydrogen Evolution Reaction.* Small, 2020. **16**(33): p. 2002850.
253. Sirota, B., N. Glavin, and A.A. Voevodin, *Room temperature magnetron sputtering and laser annealing of ultrathin MoS2 for flexible transistors.* Vacuum, 2019. **160**: p. 133-138.
254. Yu, H., et al., *Functionalization of sheet structure MoS2 with CeO2–Co3O4 for efficient photocatalytic hydrogen evolution.* Journal of Materials Science, 2018. **53**(21): p. 15271-15284.
255. Saikia, K., et al., *Sulphonated biomass-based catalyst for solketal synthesis by acetalization of glycerol – A byproduct of biodiesel production.* Fuel Processing Technology, 2022. **238**: p. 107482.
256. Chen, H., et al., *Assembling Hollow Cobalt Sulfide Nanocages Array on Graphene-like Manganese Dioxide Nanosheets for Superior Electrochemical Capacitors.* ACS Applied Materials & Interfaces, 2017. **9**(40): p. 35040-35047.
257. Shahid, M.M., et al., *Cobalt oxide nanocubes interleaved reduced graphene oxide as an efficient electrocatalyst for oxygen reduction reaction in alkaline medium.* Electrochimica Acta, 2017. **237**: p. 61-68.
258. Thambidurai, S., et al., *Morphology dependent photovoltaic performance of zinc oxide-cobalt oxide nanoparticle/nanorod composites synthesized by simple chemical co-precipitation method.* Journal of Alloys and Compounds, 2021. **852**: p. 156997.
259. Sharma, A. and B.-K. Lee, *Rapid photo-degradation of 2-chlorophenol under visible light irradiation using cobalt oxide-loaded TiO2/reduced graphene oxide nanocomposite from aqueous media.* Journal of Environmental Management, 2016. **165**: p. 1-10.
260. Wang, G., et al., *Hydrothermal Synthesis and Optical, Magnetic, and Supercapacitance Properties of Nanoporous Cobalt Oxide Nanorods.* The Journal of Physical Chemistry C, 2009. **113**(11): p. 4357-4361.
261. Lakhera, S.K., et al., *A review on particulate photocatalytic hydrogen production system: Progress made in achieving high energy conversion efficiency and key challenges ahead.* Renewable and Sustainable Energy Reviews, 2021. **152**: p. 111694.
262. Ali, S., et al., *Modification strategies of metal oxide photocatalysts for clean energy and environmental applications: A review.* Inorganic Chemistry Communications, 2022. **145**: p. 110011.
263. Aguirre, M.E., et al., *Cu2O/TiO2 heterostructures for CO2 reduction through a direct Z-scheme: Protecting Cu2O from photocorrosion.* Applied Catalysis B: Environmental, 2017. **217**: p. 485-493.
264. Matsubara, Y. and O. Ishitani, *Photochemical formation of hydride using transition metal complexes and its application to photocatalytic reduction of the coenzyme NAD(P)+ and its model compounds.* Coordination Chemistry Reviews, 2023. **477**: p. 214955.
265. Kumaravel, V., et al., *Photocatalytic Hydrogen Production: Role of Sacrificial Reagents on the Activity of Oxide, Carbon, and Sulfide Catalysts.* Catalysts, 2019. **9**: p. 276.

266. Huang, H.-B., et al., *Visible-light-driven photocatalytic H2 evolution over CdZnS nanocrystal solid solutions: interplay of twin structures, sulfur vacancies and sacrificial agents.* Journal of Materials Chemistry A, 2020. **8**(7): p. 3882-3891.
267. Chen, S. and L.-W. Wang, *Thermodynamic Oxidation and Reduction Potentials of Photocatalytic Semiconductors in Aqueous Solution.* Chemistry of Materials, 2012. **24**(18): p. 3659-3666.
268. Meng, X., et al., *Three-dimensionally hierarchical MoS2/graphene architecture for high-performance hydrogen evolution reaction.* Nano Energy, 2019. **61**: p. 611-616.
269. Luo, S., et al., *Flower-Like Interlayer-Expanded MoS2−x Nanosheets Confined in Hollow Carbon Spheres with High-Efficiency Electrocatalysis Sites for Advanced Sodium–Sulfur Battery.* 2021. **17**(37): p. 2101879.
270. Xing, Z., et al., *On the engineering part of solar hydrogen production from water splitting: Photoreactor design.* Chemical Engineering Science, 2013. **104**: p. 125-146.